



**MASARYK UNIVERSITY**

**Faculty of Science**

**Ondřej Čaha**

**Lateral compositional modulation  
in InAs/AlAs multilayers**

Doctoral thesis

Supervisor: Prof. RNDr. Václav Holý, CSc.

Brno 2007

## Bibliografická identifikace (Bibliographical data)

**Jméno a příjmení (first name and surname):** Ondřej Čaha

**Název disertační práce (dissertation title in czech):** Laterální modulace chemického složení v InAs/AlAs supermřížkách

**Název disertační práce anglicky (dissertation title in english):** Lateral compositional modulation in InAs/AlAs multilayers

**Studijní program (study program):** Fyzika (Physics)

**Studijní obor (study branch):** Fyzika pevných látek (Solid state physics)

**Školitel (supervisor):** Prof. RNDr. Václav Holý, CSc.

**Rok obhajoby (year of defence):** 2007

**Klíčová slova v češtině (keywords in czech):** rentgenová difrakce pod malým úhlem, difúzní rozptyl, samospořádací procesy, kvantové dráty, supermřížky, III-V polovodiče

**Klíčová slova v angličtině (keywords in english):** grazing-incidence X-ray diffraction, diffuse scattering, self-organization processes, quantum wires, superlattices, III-V semiconductors



# Acknowledgements

I would like to express my thank to all people who supported me during my doctoral studies. Especially I am thankful to:

- Prof. Václav Holý (MU and UK Praha) for guidance and other help during my doctoral studies.
- Assoc. Prof. Kevin E. Bassler and Prof. Simon C. Moss (UH) for guidance and other support during my stay at University of Houston.
- Dr. Jianhua Li (UH), Dr. A. Mascarenhas, Dr. A. Norman (NREL Golden), Dr. J. L. Reno (Sandia National Laboratory) for providing the samples.
- Dr. B. Krause and Dr. T. H. Metzger (ESRF Grenoble) for assistance at synchrotron measurements. Dr. Petr Mikulík, Dr. Jiří Novák and Dr. Mojmír Meduňa (MU Brno) for the experimental assistance and various discussions during my studies.
- Prof. P. W. Voorhees (Northwestern University) and Dr. Z. F. Huang (McGill University) for helpfull discussions.
- Vlastimil Křápek for providing VFF code and other practical issues.
- Prof. J. Humlíček for the conditions at the Institute of condensed matter physics at Mu Brno.
- Olga Fikarová Zrzavecká for AFM measurements.
- Tegy J. Vadakkan (UH) and my other colleagues at MU and UH for support in various scientific and practical problems.
- ...
- Last but not least to my wife.

# Abstrakt

Tato dizertační práce se zabývá morfologií supermřížek InAs/AlAs rostlých na InP(001) substrátu. Studovali jsme vývoj zvlnění povrchu jednotlivých vrstev v průběhu růstu pomocí rentgenové difrakce a také pomocí teoretického modelu růstu.

Důležitou roli v růstových simulacích i v analýze rtg rozptylu hraje elastická deformace vzorku. Použili jsme dvě metody výpočtu deformačního pole založené na teorii elastického kontinua a jednu metodu založenou na atomistickém modelu. Zjistili jsme, že výsledky jednotlivých metod se na modelu supermřížky složené z velmi tenkých vrstev dobře shodují.

Další část je věnovaná růstovým simulacím založeným na kontinuální aproximaci povrchové difúze. Studovali jsme vliv nelineárních členů v evoluční rovnici na výsledný tvar povrchu jednotlivé heteroepitaxní vrstvy a supermřížky. Zaměřili jsme se na vliv nelineárního konzervativního KPZ členu a efektu smáčecí vrstvy. Zjistili jsme, že na rozdíl od KPZ členu hraje podstatnou roli efekt smáčecí vrstvy.

Morfologie supermřížek byla studována experimentálně pomocí vysokoúhlové rentgenové difrakce a rentgenové difrakce pod malým úhlem dopadu. V teoretické části je popsána aproximativní metoda umožňující určení parametrů laterální modulace přímo z naměřených dat v difrakci pod malým úhlem dopadu. Experimentálně jsme zkoumali dva typy vzorků. První typ obsahuje 100 period supermřížky. Na tomto vzorku jsme studovali morfologii laterálně uspořádané supermřížky. Druhým typem byla série vzorků rostlých za stejných podmínek lišících se pouze počtem deponovaných vrstev. Experimentální výsledky získané na této sérii vzorků jsme srovnali s výsledky dosaženými numerickými simulacemi. Experimentální výsledky se shodují s numerickým modelem jak v hodnotě laterální periody modulace tak v modulační amplitudě.

# Abstract

This thesis is devoted to a morphology of InAs/AlAs superlattices grown on InP (001) substrate. We have studied an evolution of a surface profile using numerical growth simulations and x-ray scattering experiments.

An elastic strain field in the sample plays substantial role in both numerical growth simulations and an analysis of x-ray experiments. We describe two methods based on a continuum elasticity theory and one atomistic methods for the strain calculation. Results obtained by various computational methods in the system of short-period superlattice are compared and a good agreement is found.

In the following, numerical simulations based on a continuum approach of a surface diffusion are presented. On systems of a single heteroepitaxial layer and superlattice we have studied effects of various nonlinear terms on a resulting superlattice morphology. We focused especially on a nonlinear conservative KPZ term and a wetting effect. It was found that, in contrast to KPZ term, a wetting effect plays a substantial role in the resulting lateral composition modulation.

Diffuse x-ray scattering experiments in high-angle x-ray diffraction and grazing-incidence geometries were used to study morphology of the superlattices. In a theoretical section we present an approximative method allowing a direct determination of lateral modulation parameters from a grazing-incidence diffraction experiments. Experiments were performed on two types of samples. The first sample has 100 superlattice periods; on this sample we studied the morphology of a laterally modulated superlattice. The second type was a series of samples grown under the same deposition condition, the samples vary with the number of superlattice periods. The results obtained on the series of samples were compared to the numerical simulations. We have found good quantitative agreement of the numerical simulations to the experimental data in a lateral modulation period as well as modulation amplitude.

# Contents

<b>1</b>	<b>Introduction</b>	<b>9</b>
1.1	Structure of the thesis . . . . .	11
<b>2</b>	<b>Theory of a multilayer growth</b>	<b>13</b>
2.1	Strain field in hetero-epitaxial layers . . . . .	13
2.1.1	Strain field in an ideally flat hetero-epitaxial layer . . . . .	14
2.1.2	Analytic Fourier transform method . . . . .	18
2.1.3	Boundary integral equations . . . . .	21
2.1.4	Valence-force field method . . . . .	24
2.1.5	Comparison of the various methods . . . . .	25
2.1.6	Nonlinear dependence of the strain energy on the layer thickness . . . . .	28
2.2	Simulation of the multilayer growth . . . . .	29
2.2.1	Evolution equation . . . . .	31
2.2.2	Solution of an linearized equation . . . . .	32
2.3	Results of numerical growth simulations . . . . .	34
2.3.1	Evolution of a single layer . . . . .	34
2.3.2	Growth of a system with a nonlinear CKPZ term . . . . .	36
2.3.3	Evolution of a system with a wetting effect . . . . .	44
<b>3</b>	<b>Theory and results of x-ray scattering</b>	<b>49</b>
3.1	X-ray scattering on modulated structures . . . . .	49
3.1.1	General description of x-ray diffraction . . . . .	49
3.1.2	Distorted wave Born approximation . . . . .	51
3.1.3	GID on the samples with low number of superlattice periods . . . . .	52
3.1.4	Direct determination of the correlation function from GID . . . . .	56
3.2	Sample structure and preparation . . . . .	57
3.3	X-ray diffraction setup . . . . .	58
3.4	X-ray diffraction on the sample with higher miscut . . . . .	59
3.4.1	Analysis of the experimental data . . . . .	61
3.5	GID diffraction on the series of samples . . . . .	66
3.5.1	Comparison with growth simulations . . . . .	70
<b>4</b>	<b>Summary</b>	<b>72</b>
<b>A</b>	<b>Elastic Green function of various systems</b>	<b>75</b>
<b>B</b>	<b>List of symbols</b>	<b>78</b>

*CONTENTS*

8

**C Table of simulation parameters**

**79**

# Chapter 1

## Introduction

This thesis is devoted to self-organization processes in InAs/AlAs superlattices grown on InP. We have studied an evolution of a superlattice morphology using x-ray scattering and theoretical simulations. In the introduction we briefly review the possible applications and the preparation methods of nanostructures.

Low-dimensional semiconductor nanostructures have various possible applications in modern electronic and optoelectronic semiconductor devices. Electrons and holes are localized in the quantum nanostructures and the density of states is therefore substantially changed from bulk material. The physics of low-dimensional semiconductors is described in several books (see e.g., [1, 2] among others). The electronic and optic properties of nanostructures promise higher quantum efficiency of lasers and detectors. The quantum density of states depends strongly on the size of the nanostructures. This is the main advantage of the nanostructures, the physical properties can be tuned by the size of nanostructures. On the other hand it is crucial to obtain as narrow size distribution of the nanostructures as possible.

The basic quantum structures are quantum wells, quantum wires, and quantum dots. Schematic figure of basic structures is shown in figure 1.1. The simplest structure is the quantum well, which is few nanometers thick layer of a material with lower band gap surrounded by a semiconductor with higher band gap. Then the lowest energy states of the electrons and holes are localized inside the quantum well as a two dimensional electron gas. The fabrication of quantum wells is well developed and they are frequently used in commercial applications.

Contrary to the quantum wells, the fabrication of quantum wires and dots is more complicated. The first possible route is a lithographic preparation, which gives satisfactory size distribution and well ordered lattice of the nanostructures. However the lithographic techniques are relatively slow and expensive for industrial usage. The other possibility are self-organization processes occurring in Stranski-Krastanov growth of multilayers. The self-

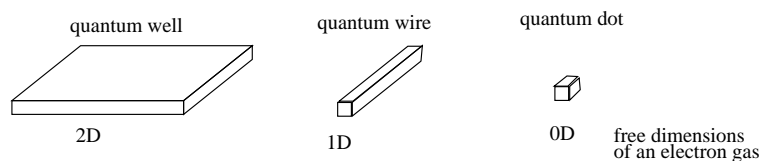


Figure 1.1: Schematic figure of various nanostructure types.

organization allows to make high density quantum structures on a large sample area. The main disadvantage of self-organized nanostructures is a wide dispersion of nanostructure size and position.

Self-organized quantum dots usually occur in the layers with positive lattice mismatch. Standard examples are systems of InAs grown on GaAs or SiGe grown on Si. In the short-period superlattices (SPS), a spontaneous lateral composition modulation (LCM) can occur leading to a quasiperiodic modulation of the thicknesses of individual layers. Resulting quantum wires are ordered in quasiperiodic lattice. LCM was observed in several types of SPS based on III-V systems, such as InAs/AlAs on InP(001) [3] or InP/GaP on GaAs(001) [4].

Lateral composition modulation in an AlAs/InAs SPS has been studied so far by transmission electron microscopy (TEM) [5], atomic force microscopy (AFM) [6], photoluminescence (PL) [7, 8] and x-ray diffraction (XRD) [9]. In these works it was found that the modulation can occur in various azimuthal directions [5, 6], depending on the mean composition of the InAs/AlAs superlattice. In superlattices with thicker InAs layers, a modulation towards  $\langle 100 \rangle$  is preferred, while, Al-rich superlattices are modulated along  $\langle 310 \rangle$  [10].

In section 3.4 of this thesis we continue in investigations published previously [9, 11], in which high-resolution x-ray scattering experiments in laterally modulated InAs/AlAs SPS were analyzed, assuming a sinus-like form of the interfaces. However, the actual form of the interfaces substantially differs from this simplified shape, since the interface consists of a sequence of discrete monolayer steps. In this thesis, we improve the structure model of a modulated SPS taking this discrete nature of the interfaces into account. We use a discrete model of the interfaces for the analysis of XRD data taken both in coplanar and grazing-incidence geometry (GID).

Theoretical description of the modulation process is based on two different models [12]. If the crystallographic miscut of the substrate surface is large (above 1 deg), the density of monolayer steps on the vicinal surface is large. In this case a stress-induced bunching of the steps takes place [12, 13] creating a nearly periodic sequence of atomically flat terraces divided by bunches of monolayer steps. The resulting modulation is one-dimensional and the average direction of the bunches is always perpendicular to the azimuthal direction of the miscut. If the miscut is small, the mean distance between the neighboring monolayer steps is larger than the diffusion length of the migrating adatoms. Then, the bunching process does not occur and the spontaneous modulation of the layer thicknesses is caused by a morphological instability of the growing surface – the Asaro-Tiller-Grinfeld instability (ATG) [14, 15, 16]. The direction of the modulation depends on the anisotropy of the physical properties (elastic constants, surface energy density) and usually a two-dimensional array of bumps is observed as a result of the ATG process.

The cited papers analyzed the self-organization process in a linearized approach from which a critical wavelength of the surface corrugation follows as function of material parameters. The exact nonlinear equation of the surface evolution was studied by Yang and Srolovitz [17] and Spencer and Meiron [18] only for the case of a semi-infinite substrate. It was found that the shape of an initially harmonic surface waviness changes and a sequence of deep cusps is created. This behavior was observed using scanning electron microscopy (see, e.g., [19]).

The physical properties of very thin layers (down to few monolayers) differ from the properties of the bulk. This difference leads to the creation of a stable two-dimensional layer at the surface (wetting layer) in the first stage of the Stranski-Krastanov growth mode. The occurrence of this so-called "wetting-effect" can be explained by a nonlinear dependence of the elastic energy density on the layer thickness [20, 21]. Simulations showed that the

wetting-effect suppresses the growth of the cusps and subsequently it leads to the formation of surface islands [22]. These islands are unstable and coalesce together (the Ostwald ripening [23]) [24]. However, numerical growth simulations indicate that an anisotropy of the surface energy limits the ripening process and causes the creation of a nearly homogeneous array of islands (see Ref. [25], among others, and the citations therein).

Several works have been published studying the ATG instability in superlattices [26, 27, 28, 29]. In these papers, a continuum model was used based on a solution of a growth equation in a first-order approximation, assuming very small amplitudes of the surface corrugation. From the analysis of the stability of the solution of this equation, critical wavelength  $L_c$  of the surface corrugation was found and its dependence on the material constants (surface energy, diffusivity of the adatoms, among others) was discussed. From this approach, an unlimited growth of the modulation amplitude follows, which does not correspond to the experimentally observed stabilization of the modulation amplitude during the growth. In this thesis we describe this stabilizing effect using the exact nonlinear equation of growth including the wetting-effect and a conservative KPZ term. We have simulated the time evolution of the spontaneous lateral modulation of layer thicknesses in short-period semiconductor superlattices and we have found that the evolution of the modulation amplitude quantitatively corresponds to the results obtained by x-ray scattering measurements.

A substantial step in the analysis of x-ray diffraction data and growth simulations is a simulation of the elastic strain fields caused by the lattice mismatch between the constituting layers, and affected by the local interface profile. For this calculation, we use continuum elasticity Fourier transform (FTM) [11, 30], boundary integral equation (BIE) [31], and valence force field (VFF) methods [32]. The application of the VFF method for a system with a free surface is complicated, since one has to take into account free dangling bonds and a surface reconstruction. Therefore, in order to simplify the calculations, we restrict the application of VFF only to an infinite superlattice. On the other hand, the FTM and BIE approach is based on an analytic solution of continuum elasticity equations and it can be used also in a close vicinity of the surface. Showing that the results of all methods coincide with a good precision far from the surface, we confirm the general validity of the FTM and BIE methods. The FTM method was used for the simulation of scattering measurements; BIE method was used in the growth simulations of the superlattice.

## 1.1 Structure of the thesis

The second chapter deals with the simulations of the multilayer growth. The strain distribution in the sample plays crucial role in the self-organization process and its knowledge is also necessary for the analysis of the x-ray diffraction measurement. Therefore we focus on the various methods of the strain field calculation in the first part of the second chapter. We describe three different methods of the strain field calculation. Two methods are based on the continuum elasticity theory and the third methods deals with the minimizing of an interatomic potential. In the next part we compare results obtained by various computational methods in the system consisting of very thin layer (in the order of few monolayers). The rest of the second chapter is devoted to the simulations of the multilayer growth. First we present the theoretical surface evolution equation due to a surface diffusion. The other parts of the chapter present the results of the numerical simulations of the deposition of single heteroepitaxial layer on a substrate and the deposition of superlattices. We focus especially

on effects of various nonlinear terms in the evolution equation on the resulting superlattice morphology and discuss values of material parameters.

In the third chapter we describe a theory of a diffuse x-ray scattering on the laterally modulated multilayers. We present the approximative method for the direct determination of the correlation function of the chemical composition from the intensity distribution in the reciprocal space. The other parts of the third chapter show the experimental results of the diffuse x-ray scattering on two types of the samples. The first sample has 100 superlattice periods; on this sample we studied the morphology of the superlattice. The second type was a series of samples grown under the same deposition condition, the samples vary with the number of superlattice periods. The results obtained on the series of samples were compared to the numerical simulations. The other parts of the third chapter describe the results of the x-ray scattering experiments and compare the experimental results to the simulation of the multilayer growth.

The last chapter contains a summary of the work. The thesis has three appendices; in the first appendix we introduce elastic Green function formulas of two-dimensional and three-dimensional isotropic and cubic systems. The second appendix is a list of used variables and the third appendix contains a table of material constants and deposition parameters used in the numerical simulations.

## Chapter 2

# Theory of a multilayer growth

In this chapter we present a theoretical description and numerical results of surface evolution of the laterally modulated structures due to a surface diffusion. The surface evolution is very sensitive to the strain distribution inside the sample. The calculation of the strain field is a complex problem and therefore we have devoted the first section to various methods of the strain calculation. The second part describes the theoretical equations of the surface evolution due to the surface diffusion and the third part contains the numerical results of the surface evolution.

### 2.1 Strain field in hetero-epitaxial layers

This section describes the methods for calculation of the strain field in the hetero-epitaxial layers; it consists of four parts. In the first section we solve an ideally flat pseudomorph layer. In the general case with non-flat surface and interfaces, it is not possible to find an analytic solution. The other sections are devoted to the three different numerical methods, which we have used.

The first method is an analytic solution using Fourier transform. In the following we will note it as analytic Fourier transform method (FTM). The main disadvantage of this method is that the top surface is assumed as ideally flat and therefore the strain near the surface is not well calculated. This method is acceptable for the simulation of the x-ray scattering, but not for the growth simulations, which are very sensitive to the strain field on the growing surface.

For the growth simulations we have used a boundary integral equations (BIE). BIE uses continuum elasticity Green functions and it is slower than FTM but gives more precise results closed to wavy surface.

These two methods are based on a linear continuum elasticity. If the layers are very thin (few monolayers), the atomic structure of the material has a big influence on the local strain. To verify the correctness of the continuum methods we have used a valence force field method (VFF), which is based on minimizing of an interatomic potential. Last two sections deal with the description of the VFF method and the comparison of the results to the continuum methods. From the atomic calculations it follows that the strain energy density depends on the layer thickness for very thin layer. In the last section we calculate the dependence of the strain energy density on the layer thickness by VFF method.

### 2.1.1 Strain field in an ideally flat hetero-epitaxial layer

The deformation of a solid can be described by the displacement vector  $\mathbf{u}(\mathbf{r})$ , which is the difference of the real position of an atom  $\mathbf{r}$  and its position in the undeformed solid  $\mathbf{r}_0$ . In the following we will also use two equivalent notations for the position vector  $\mathbf{r} = (x, y, z) \equiv \mathbf{x} = (x_1, x_2, x_3)$ . We will denote the tensor components by numbers 1, 2, and 3 or by letters  $x, y, z$ , respectively. The axis  $z \equiv x_3$  is chosen perpendicular to the sample surface.

The deformation of the sample is described by the symmetric strain tensor [33]

$$\epsilon_{ij} = \frac{1}{2} \left( \frac{\partial u_i}{\partial x_j} + \frac{\partial u_j}{\partial x_i} \right), \quad i, j = 1, 2, 3. \quad (2.1)$$

The force density in the sample is determined by the stress tensor  $\sigma$ . In the linear elasticity, the tensor  $\sigma$  is connected to the strain tensor by the Hooke law

$$\sigma_{ij} = \sum_{k,l=1}^3 C_{ijkl} \epsilon_{kl}, \quad (2.2)$$

where  $C_{ijkl}$  is a tensor of elastic constants. Because of the symmetry of tensors  $\epsilon$  and  $\sigma$  the tensor  $C$  has symmetry

$$C_{ijkl} = C_{jikl} = C_{ijlk} = C_{jilk} = C_{klij} = C_{klji} = C_{lkij} = C_{lkji}.$$

For the cubic crystal, the elastic tensor has only three independent components, which are usually noted by one pair of indices

$$C_{1111} = C_{2222} = C_{3333} \equiv C_{11}$$

$$C_{1122} = C_{2233} = C_{3311} \equiv C_{12}$$

$$C_{1212} = C_{2323} = C_{3131} \equiv C_{44}$$

and the other components are zero. In the isotropic solid the elastic tensor has two independent components

$$C_{11} = 2\mu \frac{1-\nu}{1-2\nu}$$

$$C_{12} = 2\mu \frac{\nu}{1-2\nu}$$

$$C_{44} = \mu,$$

where  $\mu$  is shear modulus and  $\nu$  is Poisson ratio. In the mechanical equilibrium the stress tensor satisfies elastic equilibrium equation

$$\sum_j \frac{\partial \sigma_{ij}}{\partial x_j} + f_i = 0, \quad (2.3)$$

where  $\mathbf{f}$  is a density of volume forces. In our case no external forces are present and then  $\mathbf{f} = 0$ . On the force-free surface the stress tensor satisfies boundary condition

$$\sum_j \sigma_{ij} |_{\text{surface}} n_j = 0, \quad (2.4)$$

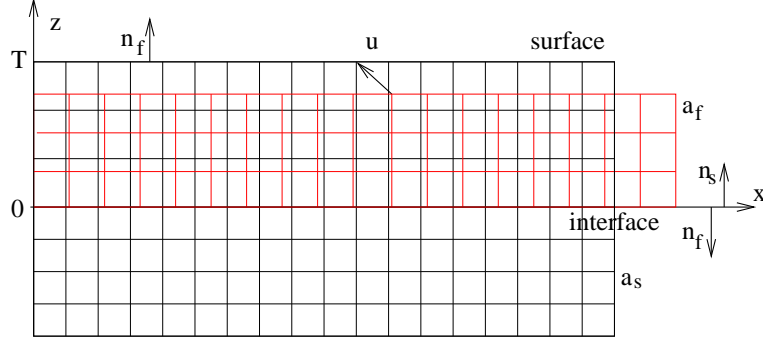


Figure 2.1: Crystal lattice of an ideally flat pseudomorph hetero-epitaxial layer. The crystallographic orientation of the surface and interface is (001). The substrate lattice is undeformed, while the lattice of the layer is deformed (compressed or tensile) to match the substrate lattice in the interface plane. The red lattice shows an unstrained lattice of a layer material.

where  $\mathbf{n}$  is the vector of surface outward normal.

In the following we will solve the system of an ideally flat pseudomorph layer shown in figure 2.1. We assume a flat interface between the substrate and layer in  $z = 0$  and the layer with thickness  $T$  (surface is in  $z = T$ ). The crystal lattice is cubic and the surface is oriented in (001) plane. Since there are no external forces acting on the sample from the equilibrium equation (2.3) follows  $\sum_j \frac{\partial \sigma_{ij}}{\partial x_j} = 0$  inside both substrate and layer. However there is a strain in the layer which comes due to a discrepancy in lattice parameters of the layer and substrate. The complete system of equations is given by the boundary conditions on the surfaces and interface. The boundary condition on the free surface is (2.4). Lattice points in the pseudomorph layer are in the same positions in the  $xy$  plane as the substrate lattice points. Since the lattice parameters of the layer and substrate materials are different, the displacement vector  $\mathbf{u}$  in the layer and the substrate is defined to the different unstrained lattices. If the displacement vector  $\mathbf{u}$  equals zero in the origin of the coordinate system (see figure 2.1), the following conditions hold for lateral components of the displacement vector at the interface

$$\begin{aligned} u_x^s(x, y, z = 0) &= u_x^f(x, y, z = 0) + x \frac{a_f - a_s}{a_s}, \\ u_y^s(x, y, z = 0) &= u_y^f(x, y, z = 0) + y \frac{a_f - a_s}{a_s}, \end{aligned}$$

where superscripts  $s$  and  $f$  mean the values of the displacement vector in substrate and layer, respectively,  $a_s$  is the lattice parameter of the substrate,  $a_f$  is the lattice parameter of the unstrained layer, and  $\zeta = \frac{a_f - a_s}{a_s}$  is the lattice mismatch of the layer with respect to the substrate. These boundary conditions on the interface for the displacement vector lead to the following boundary condition of the strain tensor

$$\begin{aligned} \epsilon_{xx}^s|_{z=0} &= \epsilon_{xx}^f|_{z=0} + \zeta \\ \epsilon_{yy}^s|_{z=0} &= \epsilon_{yy}^f|_{z=0} + \zeta. \\ \epsilon_{xy}^s|_{z=0} &= \epsilon_{xy}^f|_{z=0}. \end{aligned} \tag{2.5}$$

Other components are given by the second boundary condition for the force density acting on the interface. Since the interface is not moving the forces acting on the interface from the substrate and layer are in equilibrium. Then the components of the stress tensor satisfy the condition

$$\sum_j \sigma_{ij}^s|_{\text{interface}} n_j^s = - \sum_j \sigma_{ij}^f|_{\text{interface}} n_j^f, \quad (2.6)$$

where the outward normal of the surface  $\mathbf{n}^s$  has opposite direction to the outward normal of the layer  $\mathbf{n}^f = -\mathbf{n}^s$  (see figure 2.1). If the layer is much thinner than the substrate, we can assume that the substrate far below the layer is not deformed

$$u_i|_{z \rightarrow -\infty} = \epsilon_{ij}|_{z \rightarrow -\infty} = \sigma_{ij}|_{z \rightarrow -\infty} = 0. \quad (2.7)$$

The solution in this ideal case gives the strain and stress in the substrate equal zero

$$u_j^s = \epsilon_{jk}^s = \sigma_{jk}^s = 0.$$

The values of the strain tensor components in the layer follow from (2.5) as

$$\begin{aligned} \epsilon_{xx}^f &= \epsilon_{yy}^f = -\zeta \\ \epsilon_{xy}^f &= \epsilon_{yz}^f = \epsilon_{xz}^f = 0. \end{aligned}$$

Using the outward normal on the free surface  $\mathbf{n}^f = (0, 0, 1)$  we can simply find using the boundary condition on the free surface (2.4) that three of the stress tensor components are equal zero

$$\sigma_{xy}^f = \sigma_{yz}^f = \sigma_{xz}^f = 0.$$

Applying the the Hooke law (2.2) we get the remaining diagonal components of the stress tensor

$$\begin{aligned} \sigma_{xx}^f &= \sigma_{yy}^f = C_{12}^f \epsilon_{zz}^f - (C_{11}^f + C_{12}^f) \zeta \\ \sigma_{zz}^f &= C_{11}^f \epsilon_{zz}^f - 2C_{12}^f \zeta. \end{aligned}$$

Because of the boundary condition on the free surface  $\sigma_{zz}^f = 0$  the final solution is

$$\begin{aligned} \epsilon_{zz}^f &= 2 \frac{C_{12}^f}{C_{11}^f} \zeta \\ \sigma_{xx}^f &= \sigma_{yy}^f = \Sigma = - \frac{(C_{11}^f - C_{12}^f)(C_{11}^f + 2C_{12}^f)}{C_{11}^f} \zeta, \end{aligned} \quad (2.8)$$

where we have denoted the misfit stress  $\Sigma$ . The strain energy density is given by the expression

$$E_S = \frac{1}{2} \sum_{i,j} \epsilon_{ij} \sigma_{ij}. \quad (2.9)$$

In the case of ideally flat layer the strain energy density is

$$E_0 = \frac{(C_{11}^f - C_{12}^f)(C_{11}^f + 2C_{12}^f)}{C_{11}^f} \zeta^2. \quad (2.10)$$

For the isotropic continuum it can be expressed as

$$E_0 = 2\mu \frac{1+\nu}{1-\nu} \zeta^2.$$

In the real case surface and interface are never ideally flat. The elastic equilibrium equation (2.3) is still valid inside the substrate and the layer. The boundary conditions on the surface (2.4) on the interface (2.6) and on the backside of the sample (2.7) remain unchanged as well. Only the condition (2.5) on the interface has to be rewritten into the general form. One of the possible ways how to do it is to use the displacement vector  $\bar{\mathbf{u}}$  defined with respect to the substrate lattice in the whole sample. Then the boundary condition (2.5) for the displacement on interface is

$$\bar{u}_i^f \Big|_{\text{interface}} = \bar{u}_i^s \Big|_{\text{interface}}. \quad (2.11)$$

And we can define strain tensor with respect to the substrate lattice  $\bar{\epsilon}$

$$\bar{\epsilon}_{ij} = \frac{1}{2} \left( \frac{\partial \bar{u}_i}{\partial x_j} + \frac{\partial \bar{u}_j}{\partial x_i} \right).$$

The diagonal components of the strain tensor in the layer  $\bar{\epsilon}^f$  differ from the original strain tensor  $\epsilon^f$  by the lattice mismatch  $\zeta$ , while the other components are not changed

$$\bar{\epsilon}_{ij}^f = \epsilon_{ij}^f + \delta_{ij}\zeta, \quad (2.12)$$

where  $\delta_{ij}$  is the Kronecker tensor. Putting this formula into the Hooke law we get

$$\sigma_{ij}^f = \sum_{k,l} C_{ijkl} \bar{\epsilon}_{kl}^f - \delta_{ij}(C_{11} + 2C_{12})\zeta = \bar{\sigma}_{ij}^f - \delta_{ij}(C_{11} + 2C_{12})\zeta, \quad (2.13)$$

where we have denoted reduced stress tensor  $\bar{\sigma}_{ij} = \sum_{kl} C_{ijkl} \bar{\epsilon}_{kl}$ . Since  $\sigma$  and  $\bar{\sigma}$  differ by a constant term, the equilibrium equation (2.3) is still valid for reduced stress tensor  $\bar{\sigma}$  inside the layer or inside the substrate

$$\sum_k \frac{\partial \bar{\sigma}_{jk}}{\partial x_k} = 0. \quad (2.14)$$

The boundary condition on the free surface for  $\bar{\sigma}$  is obtained putting (2.13) into (2.4)

$$\sum_j \bar{\sigma}_{ij}^f \Big|_{\text{surface}} n_j - n_i(C_{11}^f + 2C_{12}^f)\zeta = 0. \quad (2.15)$$

And the last condition on the interface we can get substituting (2.13) into (2.6)

$$\sum_j \bar{\sigma}_{ij}^f \Big|_{\text{interface}} n_j^f - n_i^f(C_{11}^f + 2C_{12}^f)\zeta = - \sum_j \bar{\sigma}_{ij}^s \Big|_{\text{interface}} n_j^s. \quad (2.16)$$

The complete set of equations is equivalent to the formulas in the previous paragraph, but they are valid for the general case of the hetero-epitaxial layer with wavy surface and interface. The generalization to the system with more than one layer is obvious. We have to apply the boundary conditions (2.11) and (2.16) at each interface

$$\bar{u}_i^k \Big|_{\text{interface}} = \bar{u}_i^{k+1} \Big|_{\text{interface}}. \quad (2.17)$$

$$\sum_j \bar{\sigma}_{ij}^k \Big|_{\text{interface}} n_j^k - n_i^k (C_{11}^k + 2C_{12}^k) \zeta^k = - \sum_j \bar{\sigma}_{ij}^{k+1} \Big|_{\text{interface}} n_j^{k+1} - n_i^{k+1} (C_{11}^{k+1} + 2C_{12}^{k+1}) \zeta^{k+1},$$

where the superscript  $k$  denotes the values in the  $k$ -th layer.

If we assume that the elastic constants do not depend on the material, i.e., they are same in the substrate and the layer, we can simplify the system of equations. Let us introduce the mismatch function

$$\zeta(\mathbf{x}) = \begin{cases} \frac{a_f - a_s}{a_s} & \mathbf{x} \text{ inside the layer} \\ 0 & \text{otherwise.} \end{cases}$$

Putting from (2.13) into the equilibrium equation (2.3) we can substitute the boundary condition (2.17) by the density of volume force

$$\sum_k \frac{\partial \bar{\sigma}_{jk}}{\partial x_k} + f_j = 0, \quad (2.18)$$

where the density of volume forces is

$$f_j = -\frac{\partial}{\partial x_j} [(C_{11} + 2C_{12})\zeta(\mathbf{x})] = 0. \quad (2.19)$$

Inside the layer or the substrate the density of volume forces  $\mathbf{f}$  is zero and we get equation (2.14). On the surface and interface of the ideally flat layer we can evaluate the force in terms of Dirac  $\delta$  function as

$$\mathbf{f} = -(C_{11} + 2C_{12})\zeta[\delta(z) - \delta(z - T)]\mathbf{n}^f.$$

This force is equivalent to the term in the condition (2.15), and the the boundary condition on the surface has then simple form

$$\sum_k \bar{\sigma}_{jk} \Big|_{\text{surface}} n_k = 0. \quad (2.20)$$

To get the equations for the system of several layers, we have to generalize only the function of local mismatch  $\zeta$  to get the value of the local mismatch

$$\zeta(\mathbf{r}) = \frac{a(\mathbf{r}) - a_s}{a_s},$$

where  $a(\mathbf{r})$  is the unstrained lattice parameter of the material in position  $\mathbf{x}$ . It is worthy to note that such definition is valid not only for the system of chemically homogeneous layers but also for the alloys.

Since the general system is expressed in the redefined variables  $\bar{\mathbf{u}}$ ,  $\bar{\epsilon}$ , and  $\bar{\sigma}$  we will always use them in the following paragraphs and we omit the bars.

### 2.1.2 Analytic Fourier transform method

This method is based on the approach published previously in [11, 30]. The analytic solution of the equations (2.18), (2.20) and (2.7) can be found assuming that (i) the surface is ideally flat and positioned at  $z = 0$  and (ii) the elastic constants do not depend on the chemical composition. We have used the Fourier transform method for the analysis of the

sample EA532 described in chapter 3.2. From the x-ray diffraction results presented in the chapter 3.4 follows that the sample has periodic modulation closed to the direction [100]. We have simplified the calculation making further assumptions (iii) the modulation is perfectly periodic in the direction  $x \parallel [100]$  with period  $L$  and (iv) the sample structure is completely homogeneous along  $y \parallel [010]$  axis (i.e., perpendicular to the modulation direction). The equilibrium equation (2.18) can be rewritten using displacement vector as

$$\sum_{klm} C_{jklm} \frac{\partial^2 u_l}{\partial x_k \partial x_m} + f_j = 0, \quad (2.21)$$

and the surface condition (2.20) becomes

$$\sum_{klm} n_k C_{jklm} \frac{\partial u_l}{\partial x_m} \Big|_{\text{surface}} = 0. \quad (2.22)$$

Due to the cubic symmetry of the matrix  $C_{jk}$  of the elastic constants, the displacement field has only two nonzero components  $u_x, u_z$ , depending only on the coordinates  $x$  (parallel to the surface and to the LCM direction) and  $z$  (parallel to the outward surface normal).

In the periodic structure the displacement field can be expressed as the Fourier series

$$\mathbf{u}(x, z) = \sum_k \mathbf{u}^{\text{FT}}(k, z) e^{ikx}, \quad (2.23)$$

where  $k$  is an integer multiple of  $2\pi/L$ . Putting from equation (2.23) into (2.21) and (2.22), we obtain a system of ordinary differential equations

$$\hat{\mathbf{A}} \frac{d^2}{dz^2} \mathbf{u}^{\text{FT}} + i \hat{\mathbf{B}} \frac{d}{dz} \mathbf{u}^{\text{FT}} - \hat{\mathbf{C}} \mathbf{u}^{\text{FT}} = \mathbf{P}, \quad (2.24)$$

where

$$\hat{\mathbf{A}} = \begin{pmatrix} C_{44} & 0 \\ 0 & C_{11} \end{pmatrix}, \hat{\mathbf{B}}(k) = \begin{pmatrix} 0 & k(C_{12} + C_{44}) \\ k(C_{12} + C_{44}) & 0 \end{pmatrix}, \hat{\mathbf{C}}(k) = \begin{pmatrix} k^2 C_{11} & 0 \\ 0 & k^2 C_{44} \end{pmatrix},$$

and

$$\mathbf{u}^{\text{FT}}(k, z) = \begin{pmatrix} u_x(k, z) \\ u_z(k, z) \end{pmatrix}, \mathbf{P}(k, z) = (C_{11} + 2C_{12}) \begin{pmatrix} ik \zeta^{\text{FT}}(k, z) \\ \frac{d}{dz} \zeta^{\text{FT}}(k, z) \end{pmatrix}.$$

The one-dimensional Fourier transform of the local mismatch  $\zeta(x, z)$  with respect to  $x$  is denoted as  $\zeta^{\text{FT}}(k, z)$ . The boundary conditions for  $\mathbf{u}^{\text{FT}}$  at the free surface and in the substrate far below the superlattice are

$$\hat{\mathbf{A}} \frac{d}{dz} \mathbf{u}^{\text{FT}} + i \hat{\mathbf{D}} \mathbf{u}^{\text{FT}} \Big|_{z=0, z \rightarrow -\infty} = 0, \quad (2.25)$$

where

$$\hat{\mathbf{D}} = \begin{pmatrix} 0 & kC_{44} \\ kC_{12} & 0 \end{pmatrix}.$$

Equation (2.24) can be analytically solved finding the general solution  $\mathbf{v}_h$  of the homogeneous equation

$$\hat{\mathbf{A}} \frac{d^2}{dz^2} \mathbf{v}_h + i \hat{\mathbf{B}} \frac{d}{dz} \mathbf{v}_h - \hat{\mathbf{C}} \mathbf{v}_h = 0 \quad (2.26)$$

and one particular solution of the full equation  $v_p$ . The general solution of the homogeneous equation can be expressed as

$$\mathbf{v}_h = \sum_{n=1}^4 a_n \mathbf{v}_n e^{i\kappa_n z}, \quad (2.27)$$

where  $\kappa_n$  are the roots of the dispersion equation

$$\det(\hat{\mathbf{W}}) = \det(\kappa^2 \hat{\mathbf{A}} + \kappa \hat{\mathbf{B}} + \hat{\mathbf{C}}) = 0 \quad (2.28)$$

and  $\mathbf{v}_n$  are the corresponding eigenvectors  $\hat{\mathbf{W}}(\kappa_n) \mathbf{v}_n = 0$ . The particular solution can be found using Fourier transform

$$\mathbf{v}_p^{\text{FT}}(k, q) = \int_{-\infty}^{\infty} dz \mathbf{v}_p(k, z) e^{-iqz} \quad (2.29)$$

as

$$\mathbf{v}_p^{\text{FT}}(k, q) = - \left[ \hat{\mathbf{W}}(k, q) \right]^{-1} \mathbf{P}^{\text{FT}}(k, q). \quad (2.30)$$

The inverse Fourier transform can be obtained using the residuum theorem. We have denoted the eigenvalues with the positive and negative imaginary parts as  $\kappa_{n+}$  and  $\kappa_{n-}$ , respectively. The final expression for the particular solution is

$$\mathbf{v}_p(k, z) = \frac{F}{C_{11}C_{44}} \left[ \sum_{n+} \zeta^+(k, \kappa_{n+}, z) \mathbf{w}_{n+} e^{i\kappa_{n+}z} - \sum_{n-} \zeta^-(k, \kappa_{n-}, z) \mathbf{w}_{n-} e^{i\kappa_{n-}z} \right], \quad (2.31)$$

where

$$\mathbf{w}_n = \frac{1}{\prod_{j \neq n} (\kappa_n - \kappa_j)} \begin{pmatrix} C_{44}k(k^2 - \kappa_n^2) + (C_{11} - C_{12})k\kappa_n^2 \\ C_{44}\kappa_n(\kappa_n^2 - k^2) + (C_{11} - C_{12})k^2\kappa_n \end{pmatrix}$$

and

$$\begin{aligned} \zeta^+(k, \kappa, z) &= \int_{-\infty}^{\infty} dx' \int_{-\infty}^z dz' \zeta(x', z') e^{-i(kx' + \kappa z')}, \\ \zeta^-(k, \kappa, z) &= \int_{-\infty}^{\infty} dx' \int_z^0 dz' \zeta(x', z') e^{-i(kx' + \kappa z')}. \end{aligned}$$

The coefficients  $a_n$  are determined from the boundary condition (2.25). From the boundary conditions at the rear surface  $a_{n+} = 0$  follows. The remaining coefficients  $a_{n-}$  have to be obtained from the boundary condition at the surface  $z = 0$

$$\sum_{n-} a_{n-} (\kappa_{n-} v_{xn-} + k v_{zn-}) + \frac{F}{C_{11}C_{44}} \sum_{n+} (w_{xn+\kappa_{n+}} + w_{zn+k}) \zeta^+(k, \kappa_{n+}, 0) = 0, \quad (2.32)$$

$$\sum_{n-} a_{n-} (C_{11}\kappa_{n-} v_{zn-} + C_{12}k v_{xn-}) + \frac{F}{C_{11}C_{44}} \sum_{n+} (C_{11}w_{zn+\kappa_{n+}} + C_{12}w_{xn+k}) \zeta^+(k, \kappa_{n+}, 0) = 0. \quad (2.33)$$

A strain field in the sample is found by the following procedure. In the periodic system with period  $L$  we choose a finite number of Fourier components determined by the reciprocal coordinate  $k = \frac{2\pi}{L}p$ , where  $p$  is an integer. For each  $k$  we have to find four roots  $\kappa_n$  from the dispersion equation (2.28) and four corresponding eigenvectors  $\mathbf{v}_n$ . Then using equation (2.31) we evaluate the particular solution  $\mathbf{v}_p(k, z)$ . The equations (2.32) and (2.33) give us a

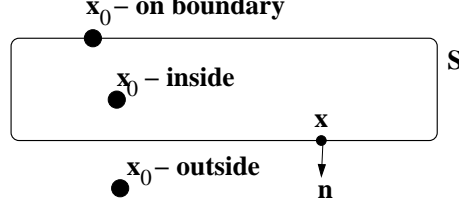


Figure 2.2: The schematic figure of the integration region in the Somigliana equation and the positions of point  $\mathbf{x}_0$ .

set of two linear equations for the coefficients  $a_{n-}$ . The general solution of a homogeneous equation  $\mathbf{v}_h(k, z)$  is then simply found using the equation (2.27). The Fourier component of the displacement field  $\mathbf{u}^{\text{FT}}(k, z)$  is a sum of the particular solution  $\mathbf{v}_p(k, z)$  and the solution of a homogeneous equation  $\mathbf{v}_h(k, z)$ . In the last step the displacement field in the real space  $\mathbf{u}(x, z)$  is calculated using equation (2.23) from the particular Fourier components  $\mathbf{u}^{\text{FT}}(k, z)$ .

### 2.1.3 Boundary integral equations

Using Boundary integral equations method we have solved the elastic equations (2.14), (2.15), (2.16), (2.12) and (2.7). We have assumed that (i) the system is perfectly periodic along  $x$  axis with period  $L$  and (ii) the strain is independent on the position in axis  $y$ . The Green function  $U_{km}(\mathbf{x}_0, \mathbf{x})$  of the elastic equilibrium equation (2.3) is solution of the equation

$$\sum_{jkl} C_{ijkl} \frac{\partial^2 U_{km}(\mathbf{x}_0, \mathbf{x})}{\partial x_j \partial x_l} = -\delta_{im} \delta(\mathbf{x} - \mathbf{x}_0). \quad (2.34)$$

The solution of elastic equilibrium equation (2.3) is evaluated using Green function as

$$u_j(\mathbf{x}_0) = \sum_k \int d\mathbf{x} U_{jk}(\mathbf{x}_0, \mathbf{x}) f_k(\mathbf{x}), \quad (2.35)$$

where the integration is performed over infinite volume. In the practical case we have a sample of a finite volume  $V$  bounded by a continuous surface  $S$ . The integral over the outer region can be evaluated using Gauss theorem; the equation is known as a Somigliana integral equation (see e.g. [31])

$$\sum_k c_{jk}(\mathbf{x}_0) u_k(\mathbf{x}_0) = \sum_k \left\{ \int_S d\mathbf{x} [U_{jk}(\mathbf{x}_0, \mathbf{x}) t_k(\mathbf{x}) - T_{jk}(\mathbf{x}_0, \mathbf{x}) u_k(\mathbf{x})] + \int_V d\mathbf{x} U_{jk}(\mathbf{x}_0, \mathbf{x}) f_k(\mathbf{x}) \right\}, \quad (2.36)$$

where  $t_j(\mathbf{x}) = \sum_{klm} C_{jklm} n_k(\mathbf{x}) \frac{\partial u_l}{\partial x_m} \Big|_{\mathbf{x}}$  is  $j$ -th component of the surface traction in position  $\mathbf{x}$ ,  $n_k$  is the  $k$ -th component of outward normal,

$$T_{jk}(\mathbf{x}_0, \mathbf{x}) = \sum_{lm} C_{jklm} n_l(\mathbf{x}) \frac{\partial}{\partial x_m} U_{lm}(\mathbf{x}_0, \mathbf{x}) \quad (2.37)$$

is the traction Green function and

$$c_{jk}(\mathbf{x}_0) = \begin{cases} 0 & \text{for } \mathbf{x}_0 \text{ outside the integrating region} \\ \delta_{jk} & \text{for } \mathbf{x}_0 \text{ inside the integrating region} \\ \frac{1}{2} \delta_{jk} & \text{for } \mathbf{x}_0 \text{ on the smooth boundary.} \end{cases} \quad (2.38)$$

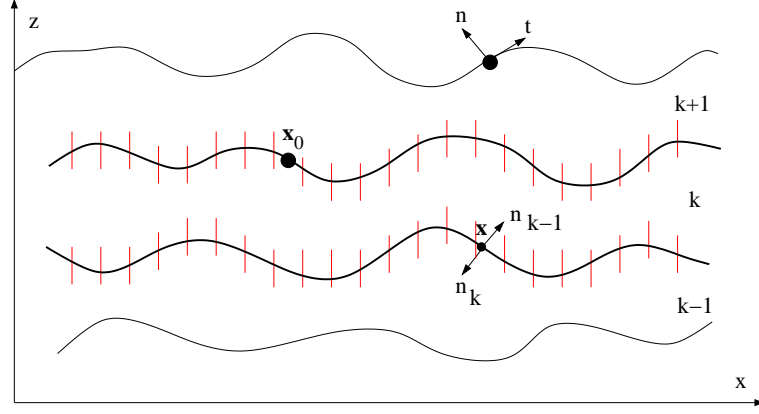


Figure 2.3: Schematic view on the superlattice. Thick lines denote the integration boundaries of the  $k$ -th layer. The boundaries of particular elements are denoted by red lines. The arrows in the point  $\mathbf{x}$  show the outward normal with respect to the  $k$ -th and  $k - 1$ -th layer. On the surface we show the direction of surface normal  $n$  and tangent  $t$ .

The schematic figure of various  $\mathbf{x}_0$  positions and the integrating region is shown in figure 2.2. If the boundary is not smooth in the point  $\mathbf{x}_0$  the appropriate values of  $c_{jk}$  can be found e.g. in reference [34]. The formulas of the Green functions for various systems are presented in the appendix A.

If the system consist of  $M$  layers on the substrate we have to solve the equation (2.36) separately in  $M + 1$  regions (one for each layer and substrate), because the equilibrium equation (2.14) is valid only inside the chemically homogeneous material. The boundary condition on the free surface (2.15) has form

$$t_j|_{\text{surface}} - n_j^M (C_{11}^M + 2C_{12}^M) \zeta^M = 0, \quad (2.39)$$

where  $\zeta^M$  is the lattice mismatch of the  $M$ -th (top) layer,  $C_{ij}^M$  are elastic parameters of the top layer, and  $\mathbf{n}^M$  is its outward normal. The boundary conditions on the interface between  $k$ -th and  $k + 1$ -th layer are from (2.17) (see also [35, 36])

$$u_j^k(\mathbf{x}) = u_j^{k+1}(\mathbf{x}), \quad t_j^k(\mathbf{x}) - n_j^k (C_{11}^k + 2C_{12}^k) \zeta^k = -t_j^{k+1}(\mathbf{x}) + n_j^{k+1} (C_{11}^{k+1} + 2C_{12}^{k+1}) \zeta^{k+1}, \quad (2.40)$$

where  $u_j^k$ ,  $t_j^k$ , and  $\zeta^k$  is displacement, traction, and lattice mismatch in the  $k$ -th layer, respectively. The integration over the substrate has to be performed along the interface between the substrate and the first layer and along the backside of the sample. Assuming that the substrate is undeformed far below the superlattice we can set the displacement and the traction on the backside of the sample equal zero and neglect its contribution to the boundary integral.

We have divided one period of the surface into  $N$  equidistant elements with lengths  $L/N$ . Assuming that the displacement is constant inside each element the integral equation (2.36) can be transformed into the set of linear algebraic equations for the upper boundary

$$\frac{1}{2} u_j(\mathbf{x}_p^U) = \sum_k \sum_{q=1}^N \left[ u_k(\mathbf{x}_q^U) \int_{S_q^U} d\mathbf{x} T_{jk}(\mathbf{x}_p^U, \mathbf{x}) + t_k(\mathbf{x}_q^U) \int_{S_q^U} d\mathbf{x} U_{jk}(\mathbf{x}_p^U, \mathbf{x}) + \right. \quad (2.41)$$

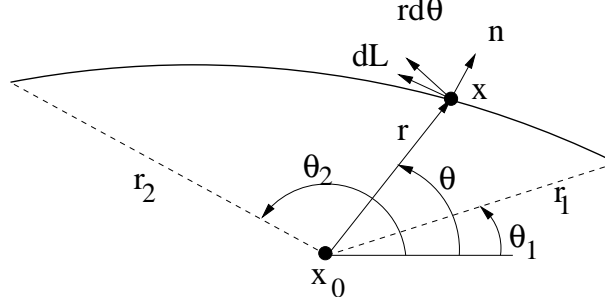


Figure 2.4: The local polar coordinate system closed to the singular point  $x_0$ .

$$+u_k(\mathbf{x}_q^L) \int_{S_q^L} d\mathbf{x} T_{jk}(\mathbf{x}_p^U, \mathbf{x}) + t_k(\mathbf{x}_q^L) \int_{S_q^L} d\mathbf{x} U_{jk}(\mathbf{x}_p^U, \mathbf{x}) \Big], \quad j = 1, 2, \quad p = 1 \dots N,$$

where  $S_q$  denotes integration over  $q$ -th element,  $\mathbf{x}_q$  is its central point, and the superscripts  $U$  and  $L$  denote points and elements on the upper and lower surface, respectively. The analogous expressions can be obtained for the points on the lower boundary, so there are  $4N$  linear equations with  $8N$  unknown variables  $u_j(\mathbf{x}_q), t_j(\mathbf{x}_q)$  for each region, that is  $4N(M+1)$  equations with  $8N(M+1)$  variables altogether. Because of the boundary conditions on each interface (2.40), surface (2.39) and neglecting the contribution from the back side of the sample we can determine one half of the unknown variables and obtain the system of  $2N(2M+1)$  linear equations for the same number of variables –  $2N$  components of the traction on  $M$  interfaces and  $2N$  components of displacement on  $M$  interfaces and on the surface. We have solved this system of linear algebraic equations using LU decomposition method [37].

The particular integrals over each element were calculated by the Gaussian quadrature with usually 20 points per an element. The surface between the given points were approximated using third order polynomial splines [37], which are smooth in any point and condition for  $c_{jk} = \frac{1}{2}\delta_{jk}$  is therefore always satisfied.

The problematic integration is over the element which includes the point  $\mathbf{x}_0$ . If  $\mathbf{x}$  equals  $\mathbf{x}_0$ , the functions  $U_{jk}(\mathbf{x}, \mathbf{x}_0)$  and  $T_{jk}(\mathbf{x}, \mathbf{x}_0)$  diverge. From the definition of the function  $U_{jk}(\mathbf{x}, \mathbf{x}_0)$  in equations (A.5) and (A.9) we can see that it has logarithmic singularity  $\ln(x - x_0)$ . The integration around the logarithmic singularity can be performed using logarithmic Gaussian quadrature. The function  $T_{jk}(\mathbf{x}, \mathbf{x}_0)$  has singularity of  $1/(x - x_0)$ . From the equation (A.7) follows that the singular is only the zero-th term in the sum (A.10). The integral over the linear element  $\Delta L$  around the singular point  $\mathbf{x}_0$  can be rewritten as

$$\int_{\Delta L} T_{jk}(\mathbf{x}, \mathbf{x}_0) u_k(\mathbf{x}) d\mathbf{x} = \int_{\Delta L} [T_{jk}(\mathbf{x}, \mathbf{x}_0) - T_{jk}^\infty(\mathbf{x}, \mathbf{x}_0)] u_k(\mathbf{x}) d\mathbf{x} + \int_{\Delta L} T_{jk}^\infty(\mathbf{x}, \mathbf{x}_0) u_k(\mathbf{x}) d\mathbf{x}, \quad (2.42)$$

where the first integral on the right hand side contains only the nonsingular terms in the infinite sum (A.10) and can be calculated without any numerical problems. The second integral was solved using technique described in [38] which allows us to calculate  $T_{jk}^\infty$  integral analytically. Assuming that the displacement  $\mathbf{u}(\mathbf{x})$  is constant inside the element  $\Delta L$  the integral can be simplified as

$$\int_{\Delta L} T_{jk}^\infty(\mathbf{x}, \mathbf{x}_0) u_k(\mathbf{x}) d\mathbf{x} = u_k(\mathbf{x}_0) \int_{\Delta L} T_{jk}^\infty(\mathbf{x}, \mathbf{x}_0) d\mathbf{x}.$$

This integral can be evaluated analytically using local polar coordinate system (see figure 2.4). Putting from the equations (A.6) and (A.7) the integral can be written as

$$\int_{\Delta L} T_{jk}^{\infty}(\mathbf{x}, \mathbf{x}_0) d\mathbf{x} = C_1 \int_{\Delta L} \left\{ C_2 \frac{1}{r} \frac{\partial r}{\partial n} \delta_{jk} + 2 \frac{1}{r} \frac{\partial r}{\partial n} \frac{\partial r}{\partial x_j} \frac{\partial r}{\partial x_k} + C_2 \frac{1}{r} \left( \frac{\partial r}{\partial x_k} n_j - \frac{\partial r}{\partial x_j} n_k \right) \right\} d\mathbf{x},$$

where  $C_1 = -\frac{1}{4\pi(1-\nu)}$  and  $C_2 = 1 - 2\nu$ . The final solution of this integral in the local coordinate system reads as [38]

$$\begin{aligned} \int_{\Delta L} T_{jk}^{\infty}(\mathbf{x}, \mathbf{x}_0) d\mathbf{x} = & C_1 C_2 (\delta_{1j} \delta_{2k} - \delta_{2j} \delta_{1k}) \ln r \Big|_{r_1}^{r_2} + \\ & + C_1 \left[ C_2 \delta_{jk} \theta + \delta_{1j} \delta_{1k} \left( \theta + \frac{1}{2} \sin 2\theta \right) - \frac{1}{2} (\delta_{1j} \delta_{2k} + \delta_{2j} \delta_{1k}) \cos 2\theta + \delta_{2j} \delta_{2k} \left( \theta - \frac{1}{2} \sin 2\theta \right) \right] \Big|_{\theta_1}^{\theta_2}, \end{aligned} \quad (2.43)$$

where  $r_1$ ,  $\theta_1$  and  $r_2$ ,  $\theta_2$  are the polar coordinates of the starting and ending point of the element  $\Delta L$ , respectively. The final integral around the singular point is given by putting the expression (2.43) into the equation (2.42). This technique allows efficient calculation of the integrals with relatively small number of integrating points over each element even close to the singularity in the Green function.

For the growth simulations it is necessary to evaluate the strain energy density on the surface, which is for the isotropic continuum

$$E_S = \frac{1}{2} \sum_{jk} [\epsilon_{jk} - \delta_{jk} \zeta] \left[ \sigma_{jk} - 2\mu \delta_{jk} \frac{1+\nu}{1-2\nu} \zeta \right].$$

The efficient calculation is to transform the strain and stress tensor components into the local coordinates  $t$  and  $n$  instead of  $x$  and  $z$ , where the axis  $t$  is parallel to the surface, while axis  $n$  has direction of the local outward normal (see figure 2.3). In that case the stress tensor has only one nonzero component  $\sigma_{tt}$  because of the boundary condition on the free surface (2.4). Therefore all three components of the strain tensor can be expressed as a function of only one independent component  $\epsilon_{tt}$ , which in point  $\mathbf{x}_p$  can be approximately expressed as

$$\epsilon_{tt}(\mathbf{x}_p) = \frac{L}{2N} (u_t(\mathbf{x}_{p+1}) - u_t(\mathbf{x}_{p-1})). \quad (2.44)$$

Then the strain energy density equals

$$E_S = \frac{\mu}{1-\nu} [(\epsilon_{tt} - \zeta)^2 - \nu \epsilon_{tt} \zeta]. \quad (2.45)$$

### 2.1.4 Valence-force field method

The valence-force field method is based on the minimization of the total energy of the crystal. This energy is expressed by means of an interatomic potential depending on the mutual positions of pairs and triplets of neighboring atoms. Several empirical or semi-empirical interatomic potentials have been used in the literature, we have chosen the potential obtained by Keating [39], and extended by Martin [32] for zinc-blende structures

$$V = \frac{1}{2} \sum_i \left[ \frac{1}{4} \sum_{j=1}^4 \frac{\alpha_{ij}}{a_{ij}^2} (\mathbf{v}_{ij}^2 - 3a_{ij}^2)^2 + \frac{1}{2} \sum_{j=1, k>j}^4 \frac{\beta_{ijk}}{a_{ij} a_{ik}} (\mathbf{v}_{ij} \cdot \mathbf{v}_{ik} + a_{ij} a_{ik})^2 \right], \quad (2.46)$$

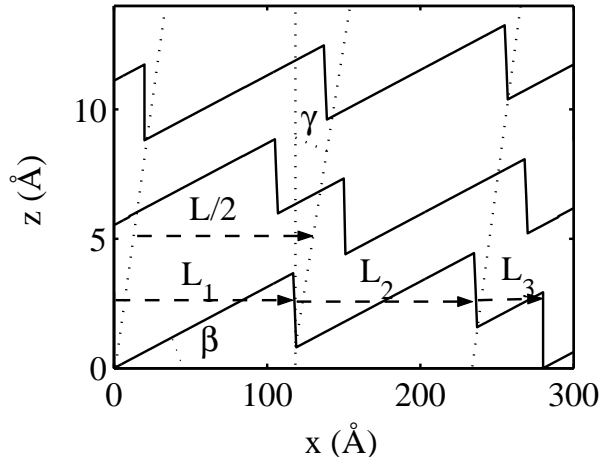


Figure 2.5: Model of LCM in the superlattice formed by the monoatomic steps.

where  $\alpha_{ij}$ ,  $\beta_{ijk}$  are potential constants,  $\mathbf{v}_{ij}$  denotes the vector connecting the  $i$ -th and the  $j$ -th atoms and  $a_{ij}$  is  $\frac{1}{4}$  of the lattice parameter. The sum over  $i$  runs over all atoms in the system, the sums over  $j$  and  $k$  comprise only four nearest neighbors of the atom  $i$ . The first term in the expression expresses the bond length change from the strain-free state, the second describes the change in the bond angles.

Minimizing the total energy in equation. (2.46), we obtain a system of  $3N$  cubic equations, where  $N$  is the total number of atoms in the system. Direct solution of the system is impossible and we used a numerical approach described in [40]; the method consists in the following. In each computation step, we minimize the energy, allowing one single atom to deviate from its starting position, other atoms are held fixed. One iteration step consists in a sequence of  $N$  computation steps, i.e., in a subsequent finding of the optimum positions of all  $N$  atoms. The iteration steps are repeated until the maximum change in the atomic positions between two last iteration steps is smaller than a requested accuracy.

In order to simplify the model, in the application of VFF we have restricted to an *infinite* periodic multilayer and we have *not* included the surface. Therefore, the results of the calculation do not consider both the surface relaxation and the influence of the substrate, and they can be compared with the results of the analytic method (see above) only far below the sample surface and far from the substrate interface.

### 2.1.5 Comparison of the various methods

We have compared the results obtained from the various methods on a model of monoatomic stairs (figure 2.5). We have chosen the parameters of the model close to the values obtained from the experiment on the sample with 100 superlattice periods (see chapter 3). From the mean lateral period  $L = 280 \text{ \AA}$  and the miscut angle  $\beta = 1.8 \pm 0.2^\circ$  it follows that three monoatomic steps (and three atomically flat terraces) fit in one LCM period; the widths of these terraces are denoted  $L_{1,2,3}$ . We assume that all the interfaces in the superlattice stack have the same values of  $L_{1,2,3}$ . For the comparison of the various method we choose  $L_1 = L_2 = 120 \text{ \AA}$  and  $L_3 = 40 \text{ \AA}$ . The positions of the steps at equivalent interfaces are laterally shifted according to the replication angle  $\gamma = 4^\circ$ . The sequence of the terraces at

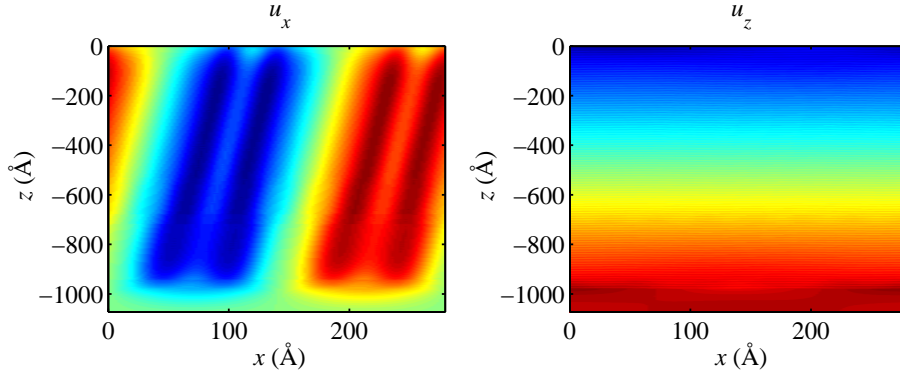


Figure 2.6: The components  $u_x$  (left) and  $u_z$  (right) of the displacement vector in the whole superlattice with the total number of 100 InAs/AlAs bilayers. The displacement field is calculated using the FTM. Single layers are not resolved in this view, closer look is presented in the figure 2.7.

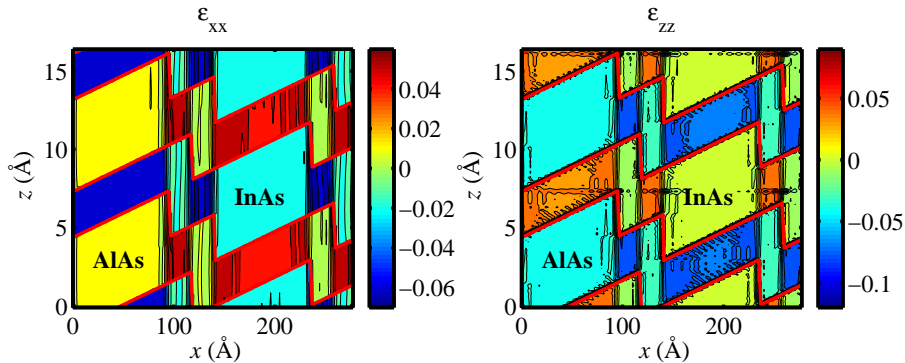


Figure 2.7: The components  $\epsilon_{xx}$  (a) and  $\epsilon_{zz}$  of the strain tensor inside the superlattice calculated using FTM. The strain tensor is evaluated with respect to the local composition. Thick red lines denote the interfaces of individual layers.

adjacent InAs/AlAs and AlAs/InAs interfaces are shifted laterally by  $L/2$ ; this shift leads to a lateral modulation of the average chemical composition of the SPS.

The components of the displacement vector  $u_x$  and  $u_z$  calculated using FTM are shown in figure 2.6. While the single layers are not resolved in this figure we have plotted the components of the strain tensor  $\epsilon_{xx}$  and  $\epsilon_{zz}$  in one bilayer in figure 2.7. From the figure 2.6 it is obvious that the strain field in the SPS, averaged vertically and laterally over the SPS and LCM periods, is homogeneous except for approx. 5 nm thin regions at the free surface and at the substrate interface.

We compared the results of FTM, BIE and VFF in the region of the homogeneous deformation; figures 2.8 and 2.9 present the displacement components  $u_{x,z}$  in one bilayer calculated by all methods. The maximum differences in  $u_x(u_z)$  are presented in table 2.1.5. The relative maximum difference are calculated with respect to the maximum differences of the maximum and minimum values of  $u_x(u_z)$  in one bilayer. The differences are caused by different approximations used in the various methods. The FTM and BIE methods approximate the

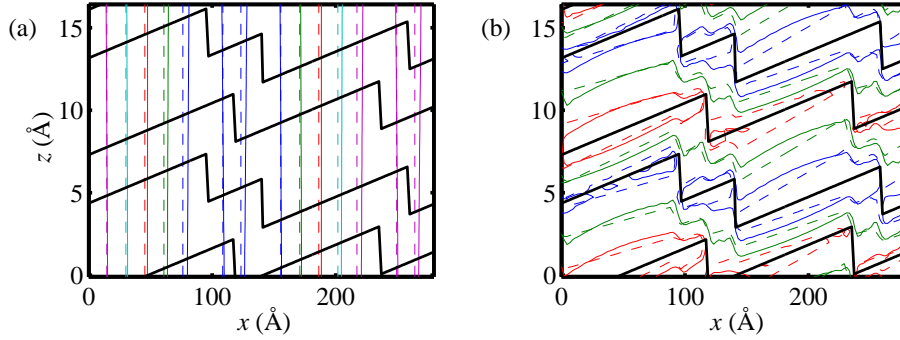


Figure 2.8: Comparison of the components  $u_x$  (a) and  $u_z$  of the displacement vector obtained by VFF and FTM methods. The same colors correspond to the same value. The solid (dashed) lines show contours calculated using FTM (VFF) method, respectively. Black lines indicate the interfaces between the layers.

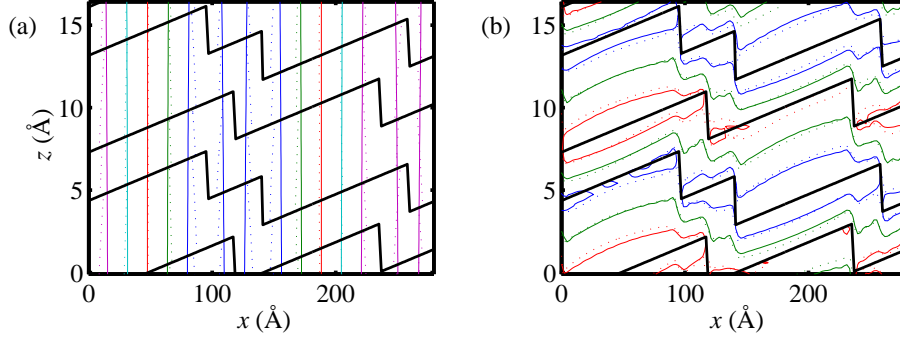


Figure 2.9: Comparison of the components  $u_x$  (a) and  $u_z$  of the displacement vector obtained by BIE and FTM methods. The same colors correspond to the same value. The solid (dotted) lines show contours from FTM (BIE) method, respectively. Black lines indicate interfaces between the layers.

Calculation method		$u_x$ (Å)		$u_z$ (Å)	
FTM	VFF	0.14	6.5 %	0.095	26 %
FTM	BIE	0.23	11 %	0.059	16 %
BIE	VFF	0.26	12 %	0.103	28 %

Table 2.1: Absolute and relative difference of the displacement field calculated using various methods. The relative difference is calculated with respect to the maximal value inside one bilayer.

actual crystal lattice by a continuum. The error introduced by this continuum approach is substantial, if the smallest size of the structure details is comparable to the lattice parameter. This is the case for the thicknesses of individual layers; the LCM period, on the other hand, is much larger. Therefore, the continuum approximation affect the values of  $u_z$  rather than  $u_x$ . Other important approximation made in the FTM is the independence of the elastic constants on the chemical composition. In addition, the FTM assumes a linear elasticity, i.e., the elastic energy in the continuum approximation is proportional to the square of the displacements, whereas the interatomic potential in equation (2.46) contains the 4th powers of the displacements. For the actual mismatch values, however, the non-linearity plays a minor role. Moreover, the VFF method considers the true point symmetry  $T_d$  of the zinc-blende unit cell, whereas the matrix of the elastic constants  $C_{jk}$  exhibits a higher  $O_h$  cubic symmetry. This difference, however, can be ruled out for the LCM orientation [100].

From this comparison it follows that the FTM approach is relevant for the simulation of x-ray diffraction even if the individual layers in the SPS are only few monolayers thick. In figure 2.7 the components  $\epsilon_{xx}$  and  $\epsilon_{zz}$  of the strain tensor are plotted; the strain components are defined with respect to the non-deformed material of the particular layer. It is obvious that in the In-rich region (the right half of the figure), the InAs layers are only slightly laterally compressed (less than 1%), while the AlAs layers are in strongly laterally stretched (about 6%) and vertically compressed (about 7%). In the Al-rich regions (the left half of the figure 2.7), the situation is opposite – the AlAs layers are only slightly laterally stretched, while InAs layers are strongly laterally compressed and vertically stretched.

We have studied the influence of these differences to the simulated x-ray diffraction intensities (see section 3.1). We calculated the intensities of the lateral maxima according to equation (3.17) from the displacement field obtained by the FTM and the VFF methods; in all geometries and wavelengths used in our study, the relative difference in the satellite intensities obtained by these methods do not exceed 10%; this difference is smaller than the smallest difference achieved between the measured and simulated diffraction data.

### 2.1.6 Nonlinear dependence of the strain energy on the layer thickness

The approximation of the system by elastic continuum works well if the length scale of the system is much larger than size of atoms. In the real systems the strain energy density in the hetero-epitaxial layer differs from the continuum expression (2.10) and depends on the layer thickness. For a Ge layer on Si, the nonlinear dependence of the strain energy density on the layer thickness was approximated by the exponential function [41]

$$f_{el}^{(0)}(h) \approx 0.05 \times E_0(1 - \exp(-h/h_{ml})), \quad (2.47)$$

where  $E_0$  is strain energy density from equation (2.10) and  $h_{ml}$  is thickness of one monolayer. We have used an analogous formula

$$f_{el}^{(0)}(h) = E_W \times (1 - \exp(-h/h_W)), \quad (2.48)$$

where  $E_W$  and  $h_W$  are parameters depending on the lattice misfit and elastic constants of the layer.

To obtain values of the wetting effect parameters  $E_W$  and  $h_W$  we have used the VFF calculation. Similar approach was used in work [21] to obtain the wetting effect parameters of Ge/Si. For that purpose we have minimized the Keating potential at the system consisting

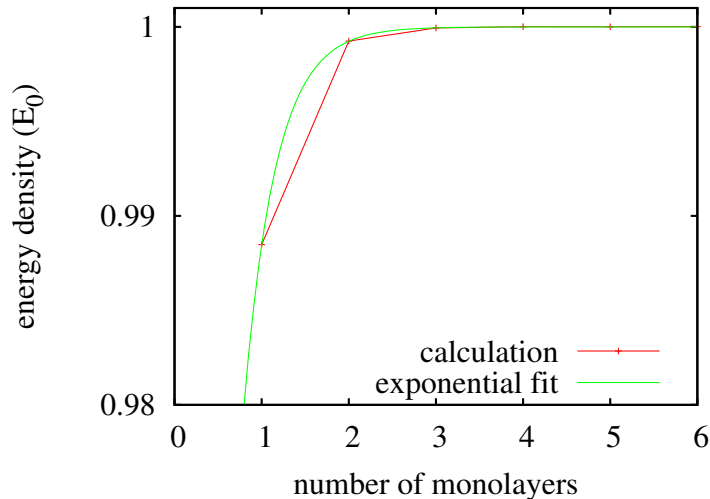


Figure 2.10: The nonlinear part of the dependence of the strain energy on the layer thickness for InAs layer on InP substrate. The strain energy density is normalized to the strain energy obtained by the continuum elasticity theory.

of an ideally flat layer on the substrate. The surface and the interface between the layer and the substrate were assumed flat and oriented in the crystallographic plane (001). Since the periodicity of the system in the directions [100] and [010] is one lattice parameter, we have to solve the system consisting of only one atom in each monolayer. The surface bonds and surface reconstruction were neglected. The calculation was provided for one to six monolayers thick layer. The substrate thickness taken into an account was six monolayers; the deeper atomic layers were assumed as undeformed substrate. The difference of the strain energy density from the continuum value  $E_0$  is shown in figure 2.10 for InAs layer on InP(001) substrate, and in figure 2.11 for AlAs layer on the InP substrate.

This difference was fitted by the exponential function (2.48). The fitted parameters are  $E_W = 0.17 \times E_0$  and  $h_W = 0.36$  ML for InAs on InP(001) and  $E_W = 0.20 \times E_0$  and  $h_W = 0.32$  ML for AlAs on InP(001).

## 2.2 Simulation of the multilayer growth

This section is divided into two parts; in the first part we present the evolution equation and in the second we describe its approximative solution. A basic evolution equation was derived by Mullins [42]. The case of the strained material was solved in the linearized approximation by Asaro and Tiller [14], Grinfeld [15], and Srolovitz [16]. Their solution was generalized to the system of multilayers by Shilkrot, Srolovitz, and Tersoff [28] and Huang and Desai [29].

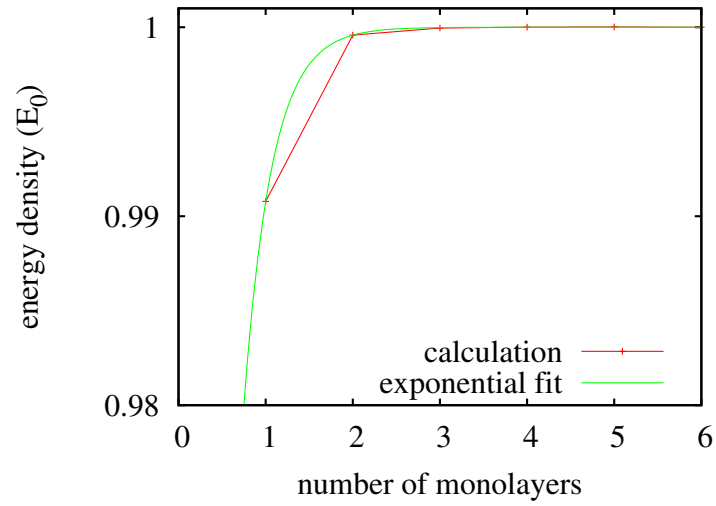


Figure 2.11: The nonlinear part of the dependence of the strain energy on the layer thickness for AlAs layer on InP substrate. The strain energy density is normalized to the strain energy obtained by the continuum elasticity theory.

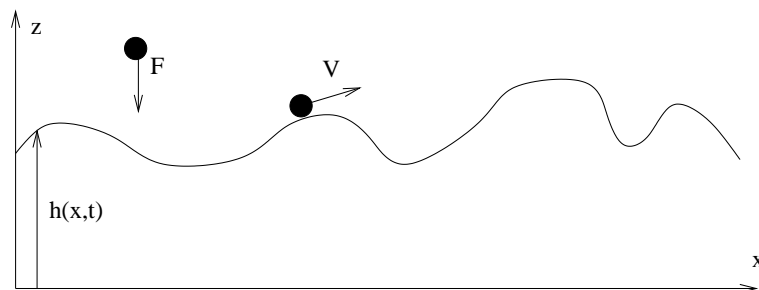


Figure 2.12: Diffusion of adsorbed atoms on the surface.

### 2.2.1 Evolution equation

The morphology of an evolving surface is described by the local height  $z = h(x, y, t)$  (see figure 2.12). The rate of change of the surface height is given by the constant deposition rate  $F$ , deposition noise  $\eta$  and by surface diffusion

$$\frac{\partial h(x, y, t)}{\partial t} = \left( \frac{\partial h(x, y, t)}{\partial t} \right)_{\text{diff}} + F + \eta. \quad (2.49)$$

The adsorbed atoms drift along the surface with average velocity given by the Nernst-Einstein relation[42]

$$V_{\text{diff}} = -\frac{D_s}{k_B T} \nabla_s \mu_s, \quad (2.50)$$

where  $D_s$  the surface diffusion coefficient,  $k_B$  is the Boltzmann constant,  $T$  is temperature,  $\nabla_s$  denotes derivation along the surface, and  $\mu_s$  is the chemical potential on the surface. The surface current  $J$  of atoms is product of  $V_{\text{diff}}$  by the number of atoms per unit area  $\theta$

$$J = -\frac{D_s \theta}{k_B T} \nabla_s \mu_s.$$

If the surface divergence of  $-J$  is taken, one obtains the increase in number of atoms per unit area per unit time. Multiplying  $-\nabla_s J$  by the volume of one atom  $\Omega$  we get the increase of a layer volume per unit area which is the speed of change of surface height. Then the complete evolution equation can be written in the form

$$\frac{\partial h(x, y, t)}{\partial t} = \frac{D_s \theta \Omega}{k_B T} \nabla_s^2 \mu_s(x, y, t) + F + \eta(x, y, t). \quad (2.51)$$

For the following we assume the evolution of quantum wires parallel to the  $y$  axis. The height  $h$  and the chemical potential  $\mu_s$  are independent on  $y$ . Then the surface Laplacian has simpler form

$$\nabla_s^2 = \frac{\partial}{\partial x} \left[ (1 + h'^2)^{-\frac{1}{2}} \frac{\partial}{\partial x} \right], \quad (2.52)$$

where  $h' = \frac{\partial h}{\partial x}$ .

The chemical potential  $\mu_s$  can be expressed as [41, 42, 43]

$$\mu_s(x, t) = \mu_{s0} + \Omega \left[ \gamma \kappa + E_S|_{z=h(x)} + \frac{df_{el}^{(0)}(h)}{dh} \right], \quad (2.53)$$

where  $\mu_{s0}$  is the chemical potential of an ideally flat unstrained surface,  $\gamma$  is density of the surface energy per unit area and corresponds to the classical surface tension,  $\kappa$  is the surface curvature, and  $E_S$  is the strain energy density on the surface. The function  $f_{el}^{(0)}(h)$  describes a nonlinear dependence of the free energy density on the layer thickness  $h$  giving rise to a wetting-effect. We have used the exponential formula (2.48)

$$f_{el}^{(0)}(h) = E_W \times (1 - \exp(-h/h_W)). \quad (2.54)$$

where the parameters  $E_W$  and  $h_W$  are calculated in section 2.1.6. The surface curvature  $\kappa$  can be expressed as [42]

$$\kappa = -\frac{h''}{(1 + h'^2)^{\frac{3}{2}}}. \quad (2.55)$$

The full system of the nonlinear equations is obtained putting from (2.53) into (2.51). This equation was solved numerically and the strain energy density was calculated using boundary integral equation method described in part 2.1.3. The simplest integration method is the Gaussian integration

$$h(t + \Delta t) = \Delta t \frac{\partial h}{\partial t} + h(t).$$

We have used more precise Houbolt integration scheme [17, 44]

$$h(t + \Delta t) = \frac{1}{11} \left[ 6\Delta t \frac{\partial h}{\partial t} + 18h(t) - 9h(t - \Delta t) + 2h(t - 2\Delta t) \right], \quad (2.56)$$

where  $\frac{\partial h}{\partial t}$  is given by the equation (2.51). The results of this integration scheme was verified using Runge-Kutta integration adapted to the evolution equation with a random noise term [45]. The surface height  $h$  was integrated in  $N$  equidistant distributed points  $x_p$ . The derivatives  $\frac{dh}{dx}$  were calculated by means of the central differences.

The slowest step is the evaluation of the strain energy, which includes many numerical integrations and solution of a system of linear algebraic equations. To accelerate the integration of the evolution equation, the strain energy density was calculated only if the surface profile was substantially changed. The strain energy was recalculated if the height  $h(x_p, t)$  was changed more than given value  $\delta$  in any point  $x_p$  from the last calculation of the strain energy. The parameter  $\delta$  was typically set to be 0.1 Å. The results of the numerical simulations are presented in chapter 2.3.

## 2.2.2 Solution of an linearized equation

Although it is impossible to find an analytic solution of the full nonlinear evolution equation presented in the previous paragraph, an analytic solution of an linearized equation was found. The linearized approach was presented by Asaro and Tiller [14], Grinfeld [15], and Srolovitz [16] for the case of strained semi-infinite substrate. Shilkrot, Srolovitz, and Tersoff [28] and Huang and Desai [29] found the linear approximation of the multilayers without the wetting effect. The height of the growing layer can be written as sum of the average height  $\bar{h}(t)$  at time  $t$  and the perturbation  $\Delta(x, t)$  from the average flat surface.

$$h(x, t) = \bar{h}(t) + \Delta(x, t). \quad (2.57)$$

Since the diffusion and noise don't change the average number of atoms, the average height  $\bar{h}$  is linear function of time

$$\bar{h}(t) = \bar{h}(t_0) + (t - t_0)F. \quad (2.58)$$

In the linear approach we assume that the derivative of the perturbation is very small  $\frac{\partial \Delta}{\partial x} \ll 1$  and therefore we can neglect the derivative  $h'$  in the surface Laplacian and curvature. If we neglect the wetting effect and the noise, the evolution equation (2.51) is then transformed into the form

$$\frac{\partial \Delta(x, t)}{\partial t} = \frac{D_s \theta \Omega}{k_B T} \frac{\partial^2 \mu_s(x, t)}{\partial x^2} = \frac{D_s \theta \Omega^2}{k_B T} \frac{\partial^2}{\partial x^2} \left[ -\gamma \frac{\partial^2 \Delta(x, t)}{\partial x^2} + E_S(x, t) \right], \quad (2.59)$$

where the derivative along the surface was replaced by derivative with respect to  $x$  coordinate. Solution of this equation can be found using Fourier transform in  $x$

$$\frac{\partial \Delta^{\text{FT}}(k, t)}{\partial t} = -k^2 \frac{D_s \theta \Omega^2}{k_B T} \left[ \gamma k^2 \Delta^{\text{FT}}(k, t) + E_S^{\text{FT}}(k, T) \right], \quad (2.60)$$

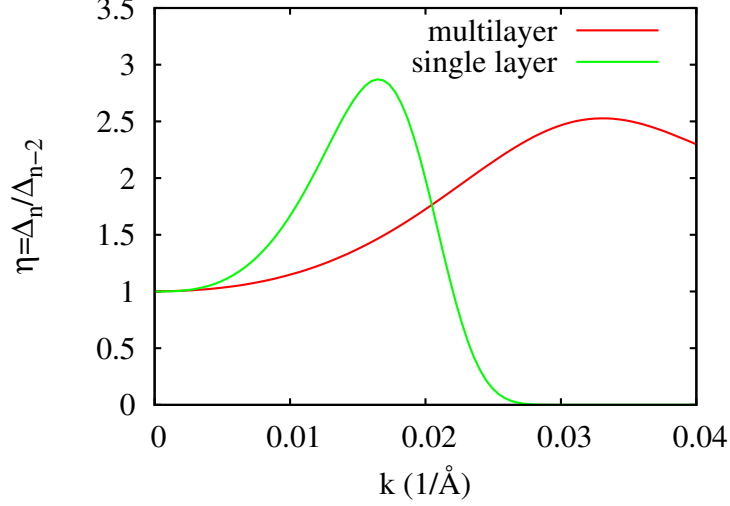


Figure 2.13: The ratio  $\eta = \Delta_n^{\text{FT}}/\Delta_{n-2}^{\text{FT}}$  of the amplitudes of the interface corrugation at subsequent interfaces calculated for various wave vectors  $k = 2\pi/L$  of the surface corrugation using the ATG model (single layer) [14, 15] and a multilayer model [28, 29]. In the ATG model we have assumed a growth of an InAs layer on InP.

where  $\Delta^{\text{FT}}(k, t)$  and  $E_S^{\text{FT}}(k, t)$  are Fourier components of  $\Delta(x, t)$  and  $E_S(x, t)$ , respectively.

First we will find the first order approximation for the strain energy density in the case of strained semi-infinite substrate. As was shown in the section 2.1.1 the components of the strain tensor at the ideally flat surface  $\Delta^{\text{FT}}(k) = 0$  are

$$\sigma_{xx} = \Sigma, \quad \sigma_{zz} = \sigma_{xz} = 0. \quad (2.61)$$

For small perturbation ( $\Delta^{\text{FT}}(k) \ll 1/k$ ), the solution of the mechanical equilibrium was found in the form [14, 15, 16]

$$\begin{aligned} \sigma_{xx} &= \Sigma \left[ 1 - \Delta^{\text{FT}}(k)k(kz - 2)e^{-kz} \sin(kx) \right] \\ \sigma_{zz} &= \Sigma \Delta^{\text{FT}}(k)k^2 z e^{-kz} \sin(kx) \\ \sigma_{xz} &= \Sigma \Delta^{\text{FT}}(k)k^2 (1 - kz)e^{-kz} \cos(kx), \end{aligned}$$

where all terms in the higher order in  $\Delta^{\text{FT}}(k)k$  were neglected. The equation (2.60) then reads as

$$\frac{\partial \Delta^{\text{FT}}(k)}{\partial t} = -\Gamma \gamma k^4 \Delta^{\text{FT}}(k, t) + 2\Gamma \frac{\Sigma^2 k^3}{M} \Delta^{\text{FT}}(k, t), \quad (2.62)$$

where  $\Gamma = \frac{D_s \Omega^2 \theta}{k_B T}$  and  $M = \mu \frac{1+\nu}{1-\nu}$  for the isotropic solid. The solution of this equation is

$$\Delta^{\text{FT}}(k, t) = \Delta^{\text{FT}}(k, 0) \exp \left\{ \Gamma [2\Sigma^2/Mk^3 - \gamma k^4] t \right\}. \quad (2.63)$$

Thus for  $k < k_0 = \frac{2\Sigma^2}{\gamma M}$  or for wavelengths longer than  $\lambda_0 = \frac{2\pi}{k_0}$  the amplitude grows exponentially to infinity; for  $k > k_0$  the perturbation quickly disappears. The fastest growing wavelength is the critical wavelength  $\lambda_c = 4/3\lambda_0$ . In figure 2.13 we show the dependence

of the quantity  $\frac{\Delta^{\text{FT}}(k,t)}{\Delta^{\text{FT}}(k,0)}$  for the time  $t$  corresponding to the deposition of 1 nm thick layer of InAs on the InP substrate. From the equation follows that the presence of initial perturbation  $\Delta^{\text{FT}}(k,0)$  is essential to develop any surface morphology. This condition is always satisfied because random fluctuations are present on the real surfaces.

In multilayers, the stress tensor on the surface is influenced by the morphology of lower interfaces. In first order in perturbation theory, the stress  $\sigma_{xx}$  consists of two contributions

$$\sigma_{xx}(x) = \sigma_{\text{surf}} + \sigma_{\text{int}}. \quad (2.64)$$

The first term is associated with the surface itself and is the same as was calculated for the semi-infinite solid in previous paragraph. The second term is associated with the presence of buried interfaces. The contribution from the interface between  $n$ -th and  $(n+1)$ -th layer is [28, 29]

$$\sigma_{\text{int}}^{n/n+1} = -2|k|(\Sigma_n - \Sigma_{n+1})e^{-|k|h_n}\Delta_n^{\text{FT}}(k), \quad (2.65)$$

where  $\Sigma_n$  is misfit stress in the  $n$ -th layer,  $\Delta_n^{\text{FT}}(k)$  is the perturbation of the interface under consideration, and  $h_n$  is the distance of this interface to the growing surface. The complete solution within this approximation is described in [29]. The result shows that the growth depends on the given values of the deposition rate, thicknesses of the particular layers, misfit stress, and surface tension. If the multilayer consists of periodic bilayers the amplitude of  $k$ -th layer is given by the next nearest neighbor amplitude as  $\Delta_n^{\text{FT}}(k) = \eta\Delta_{n-2}^{\text{FT}}(k) = \eta^{n/2}\Delta_0^{\text{FT}}(k)$ . The ratio  $\eta$  is plotted in the figure 2.13 for the InAs/AlAs superlattice on InP.

## 2.3 Results of numerical growth simulations

In this section we present the results of the growth simulations. The first section deals with the growth of single layer on the substrate without the wetting effect. The second section describes the growth of the single layer and multilayers in presence of the conservative KPZ term. In the last section we show the evolution of a single layer and multilayers with the wetting effect.

### 2.3.1 Evolution of a single layer

At first we have studied the evolution of the single layer on the substrate. If the layer on the substrate is very thick, the wetting effect and shape of the layer/substrate interface don't play a role. That case corresponds to the system of strained semi-infinite substrate studied by Yang and Srolovitz [17] and Spencer and Meiron [18]. We have reproduced their results in order to test our simulating code. The example of the surface evolution is shown in figure 2.14. The length of the system is chosen to be the critical unstable wavelength of the linearized equation  $\lambda_c$  (see section 2.2.2). Both [17, 18] shows that starting from the initial smooth cosine profile, the amplitude of the cosine grows with an increasing speed and the initially cosine profile evolves into cusps. We have also studied the evolution of the system with larger size than one wavelength. An example simulation starting from the random surface is presented in the figure 2.15. In the initial stage the system evolves in good agreement with the linearized theory. The dependence of the growth rate on the frequency can be found using Fourier transform of the surface profile. Figure 2.16 shows the Fourier transform of the surface profile after short time from the beginning divided by the Fourier transform of the

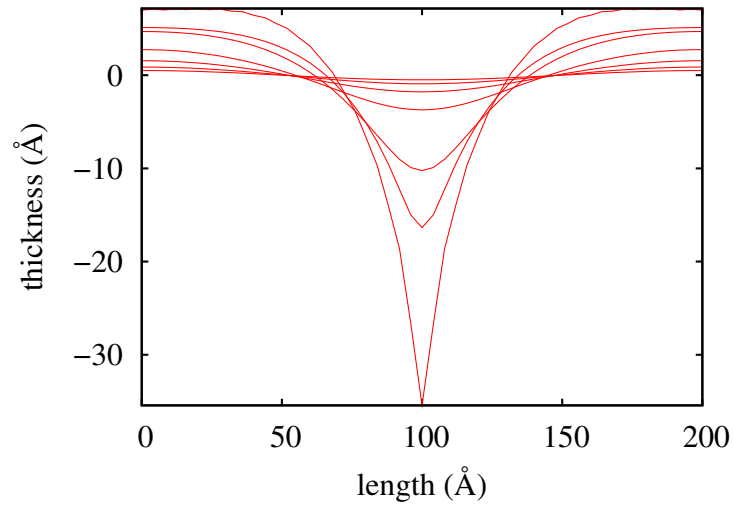


Figure 2.14: The surface evolution of the semi-infinite strained substrate. The period of the system was chosen to the most unstable wavelength [18].

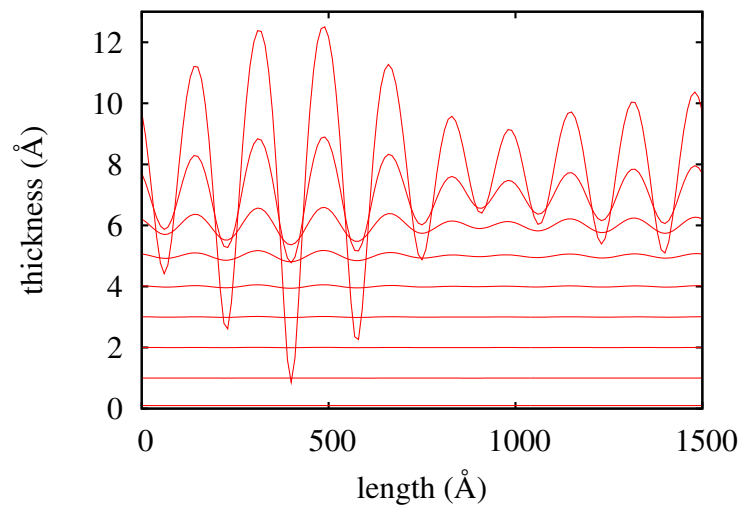


Figure 2.15: The surface evolution of the semi-infinite strained substrate of larger system. The surface finds the most unstable wavelength and then it evolves into the cracks.

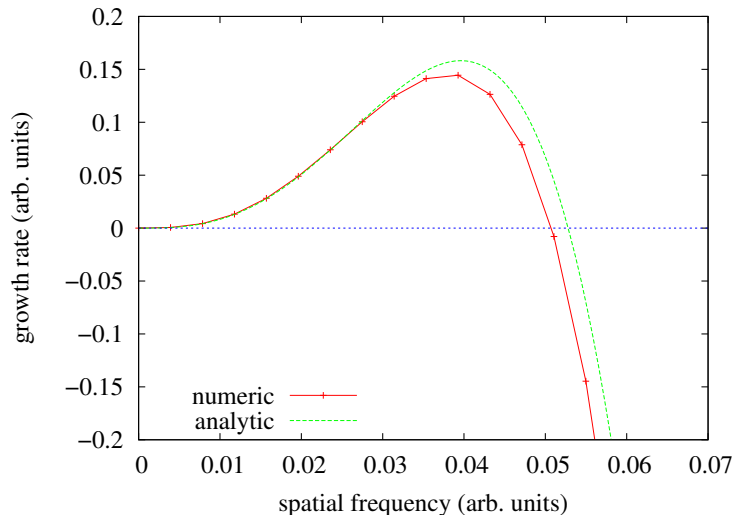


Figure 2.16: Comparison of the growth rate as function of the modulation period from the analytic and numeric calculation.

initial surface profile and the analytic prediction from the linearized theory. As is shown in the figure the difference between the analytic and numeric calculation slightly grows with the increasing spatial frequency. In the beginning the surface finds the critical wavelength  $\lambda_c$ , which overgrow the modulation with other frequencies. In the latter stage with increasing amplitude of the surface profile the nonlinear terms in the evolution equation play bigger role. The almost cosine waves change shapes and the cusp evolution appears in the similar way as in the simulation of small system.

The evolution of the cusps was observed in experiment on few systems such as SiGe/Si in the works [19, 46]. However the cusp evolution was not observed in all semiconductor systems. We have tried several ways to limit the cusp evolution.

### 2.3.2 Growth of a system with a nonlinear CKPZ term

Kardar, Parisi, and Zhang proposed the evolution equation (2.51) with the nonlinear term [47]

$$\frac{\partial h(x, t)}{\partial t} = \frac{D_s \theta \Omega}{k_B T} \nabla^2 \mu_s(x, t) + F + \eta(x, t) + \psi \left( \frac{\partial h(x, t)}{\partial x} \right)^2. \quad (2.66)$$

In the following we will note this nonlinear correction as a KPZ term. The KPZ term accounts for the dependence of the deposition rate on the surface slope. The deposition rate  $F$  is measured in the direction normal to the surface, while the height  $h(x, t)$  is measured in the direction of  $z$ -axis. The first order approximation of this inclination gives us the value of  $\psi = F/2$ . The KPZ term is not conservative, i.e., that the *mean* deposition rate depends on the surface profile.

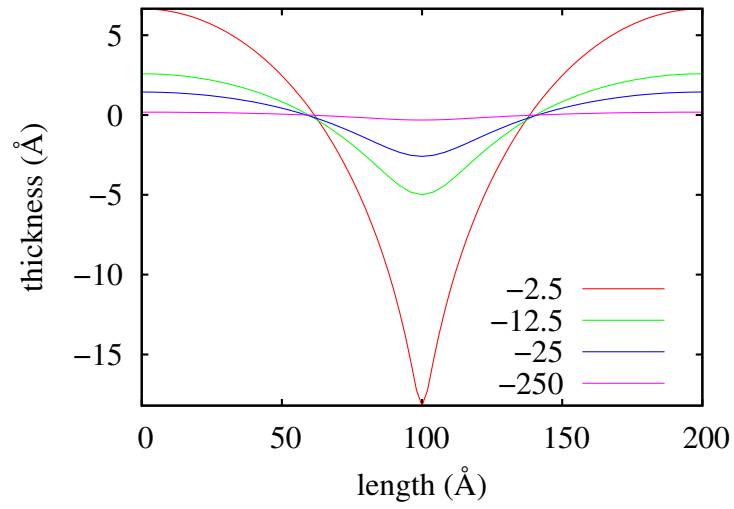


Figure 2.17: Stable shapes for various negative values of the CKPZ parameter.

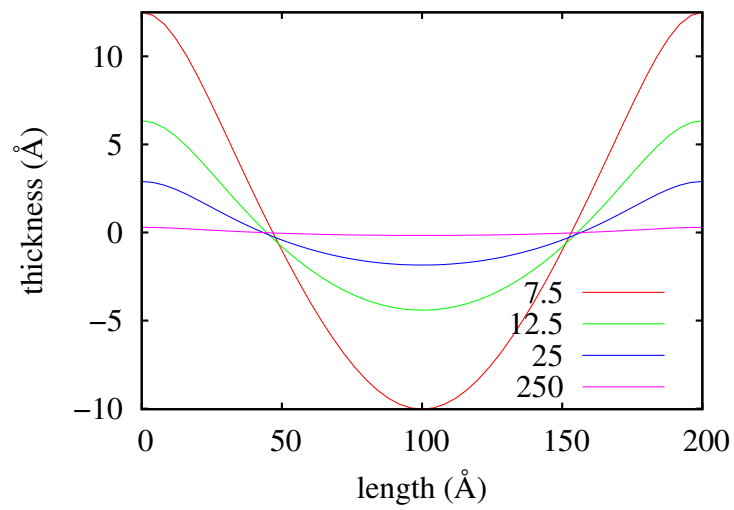


Figure 2.18: Stable shapes for various positive values of the CKPZ parameter.

However, Lai and Das Sarma suggested that under molecular beam epitaxy (MBE) conditions the surface growth is conservative [48, 49]. Instead of the classic KPZ term we have used conservative KPZ (CKPZ) term, first proposed in the reference [50]:

$$\frac{\partial h(x, t)}{\partial t} = \frac{D_s \theta \Omega}{k_B T} \nabla^2 \mu_s(x, t) + F + \eta(x, t) + \psi \frac{\partial^2}{\partial x^2} \left( \frac{\partial h(x, t)}{\partial x} \right)^2. \quad (2.67)$$

A physical interpretation was suggested by Villain [51], who pointed out that the nonlinearity could arise from a dependence of the adatom density on the surface inclination. Krug [52] motivated CKPZ term by the inclination dependence of a nonlinear contribution to the adatom chemical potential. Golovin, Davis, and Voorhees interpreted CKPZ term as one of nonlinear terms approximating the wetting effect.

First we have studied the evolution equation with CKPZ term in the system consisted of a thick single layer on the substrate. In this system the evolution equation does not depend on the particular layer thickness. It is useful to use instead of the layer height its deviation  $\Delta(x, t)$  from the mean height  $\bar{h}(t)$  as was introduced in the section 2.2.2. Then the evolution equation reads as

$$\frac{\partial \Delta(x, t)}{\partial t} = \Gamma \frac{\partial^2}{\partial x^2} \left[ \gamma \kappa + E_S + \frac{\psi}{\Gamma} \left( \frac{\partial \Delta(x, t)}{\partial x} \right)^2 \right] + \eta(x, t), \quad (2.68)$$

where  $\Gamma = \frac{D_s \theta \Omega^2}{k_B T}$  and the CKPZ term was merged with the surface diffusion term. In the following we express the value of  $\psi$  in units of  $\psi_0 = \Gamma E_0$ , where  $E_0$  is the strain energy density of a flat layer given by the formula (2.10).

The influence of the CKPZ term was first studied in the system with the size of the critical period. We have observed that both positive and negative values of the parameter  $\psi$  prevent the pit and consequent crack formation. The profile evolution reaches the steady shape for  $\psi$  lower than  $-2.5\psi_0$ . The steady shapes are plotted in the figure 2.17. The steady shape for the negative values has pit in the bottom and the amplitude decreases with the decreasing value of the parameter  $\psi$ .

For the positive value of the CKPZ parameter the system reaches the steady as well. While for the negative value the steady profile has pits, the steady shapes for the positive values of  $\psi$  have cusps on the top. The overview of the steady shapes for the positive value is in the figure 2.18. The steady shapes are in good agreement with the work [53].

Golovin, Davis and Voorhees studied the evolution with the nonlinear CKPZ parameter and with the elastic energy approximation up to the first order nonlinear term. They have found that the steady shape cannot be reached for the parameter  $\psi$  closed to the zero value. There is high curvature at the pit (for positive CKPZ parameter  $\psi$ ) or cusp (negative) and therefore the simulation in the region around this sharp shape is very sensitive to the number of elements in the numeric solution. We have performed the simulations for the system of the length  $\lambda_c$  with 50, 100, 150, and 200 elements. The dependence of the steady amplitude on the parameter  $\psi$  obtained for the various number of elements is shown in the figure 2.19. For negative CKPZ parameter the steady amplitude is independent on the number of elements and reaches the stable state. For  $\psi$  value bigger than  $7\psi_0$ , the stable shape is also reached. In the region between  $0.25\psi_0$  and  $7\psi_0$  we have found that the amplitude of a "steady" shape increases with the number of calculation elements. The steady shape in this region has very sharp cusp and its amplitude is limited by the artifacts of the numerical methods rather

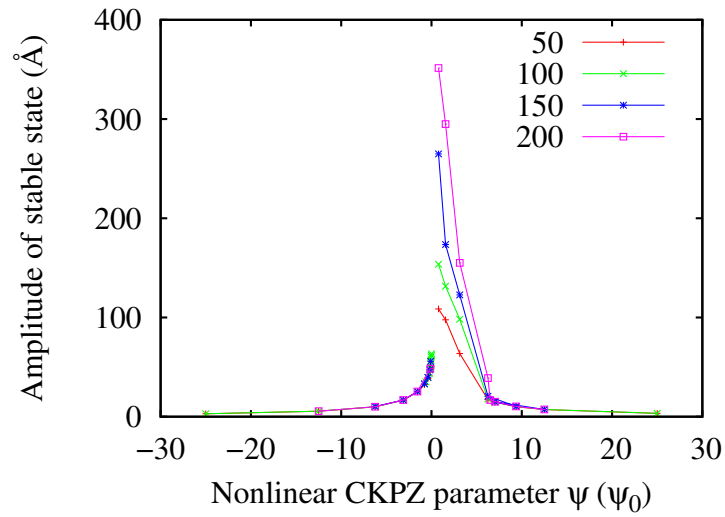


Figure 2.19: The dependence of the stable amplitude on the value of the CKPZ parameter. The various lines correspond to the different number of elements in one period.

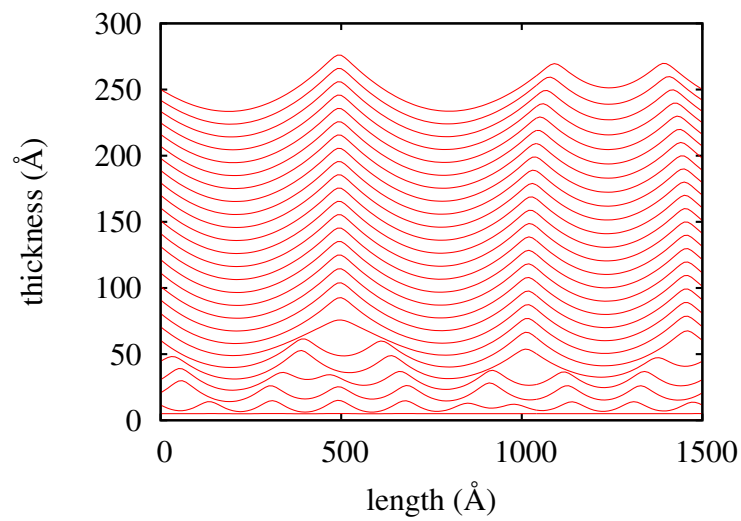


Figure 2.20: The surface evolution of the single layer on the substrate with positive value of the CKPZ parameter  $\psi = 25\psi_0$ . The lines show the surface in the various time.

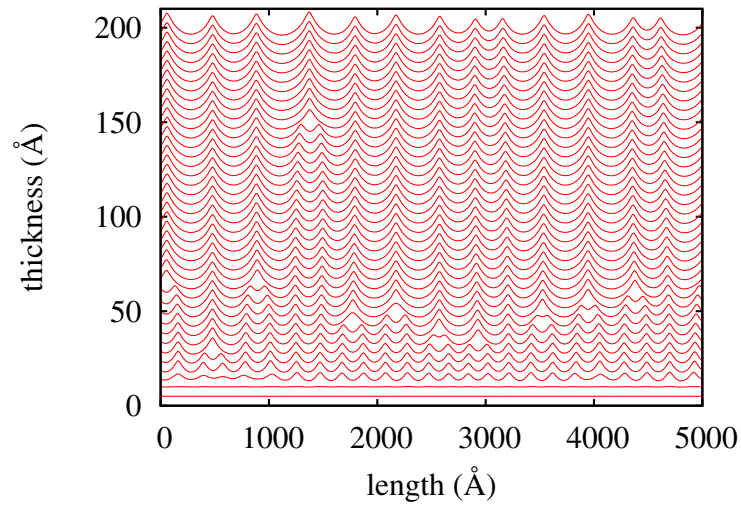


Figure 2.21: The surface evolution of the single layer on the substrate with positive value of the CKPZ parameter  $\psi = 25\psi_0$ . The lines show the surface in the various time.

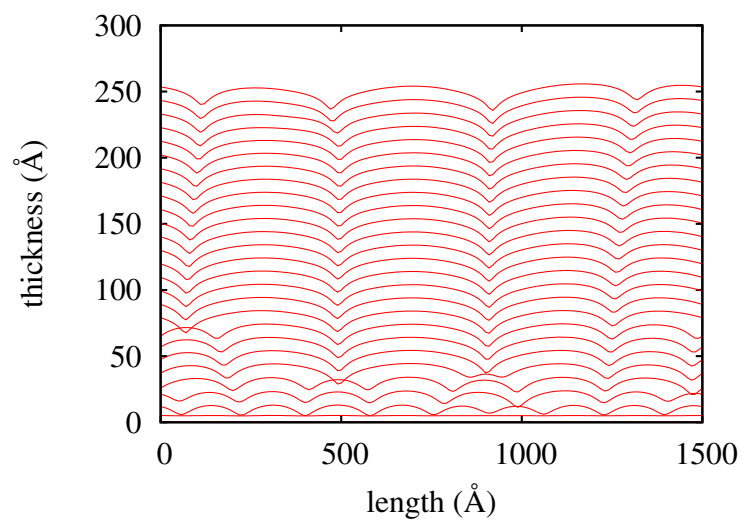


Figure 2.22: The surface evolution of the single layer on the substrate with negative value of the CKPZ parameter  $\psi = -25\psi_0$ . The lines show the surface in the various time.

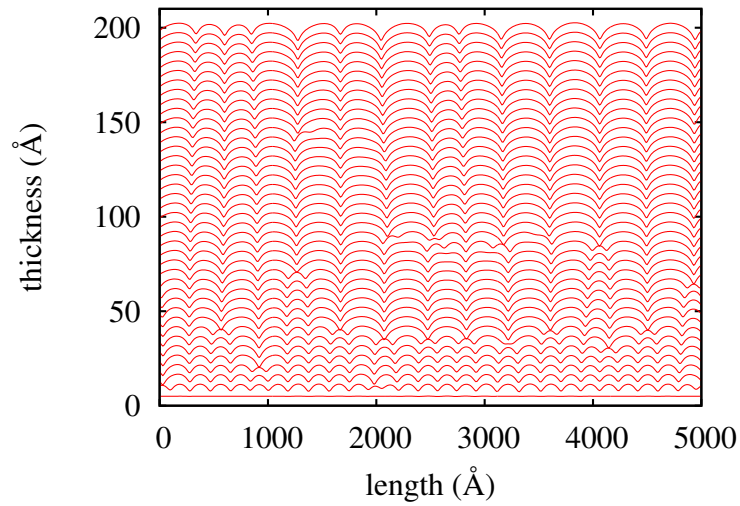


Figure 2.23: The surface evolution of the single layer on the substrate with negative value of the CKPZ parameter  $\psi = -25\psi_0$ . The lines show the surface in the various time.

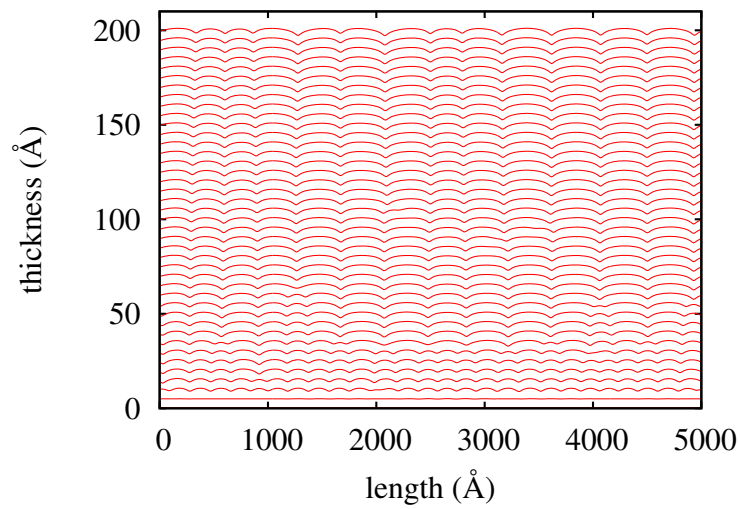


Figure 2.24: The surface evolution of the single layer on the substrate with negative value of the CKPZ parameter  $\psi = -60\psi_0$ . The lines show the surface in the various time.

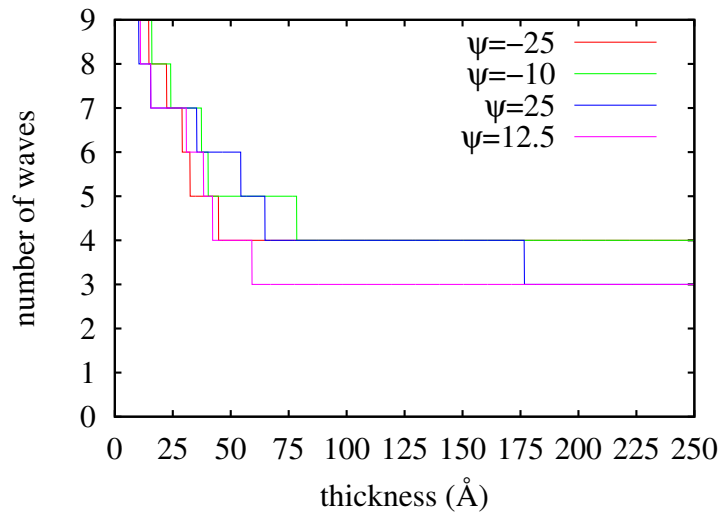


Figure 2.25: The dependence of the number of waves on the layer thickness in the system of size  $9\lambda_c$  for various values of CKPZ parameter  $\psi$ .

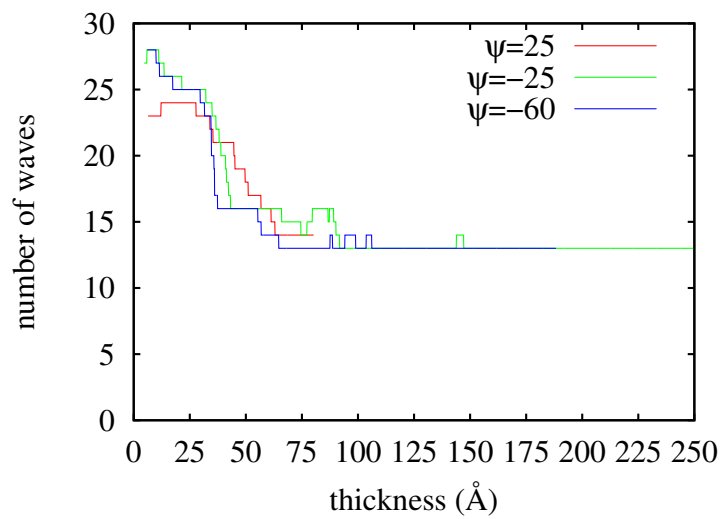


Figure 2.26: The dependence of the number of waves on the layer thickness in the system of length  $30\lambda_c$  for various values of the CKPZ parameter  $\psi$ .

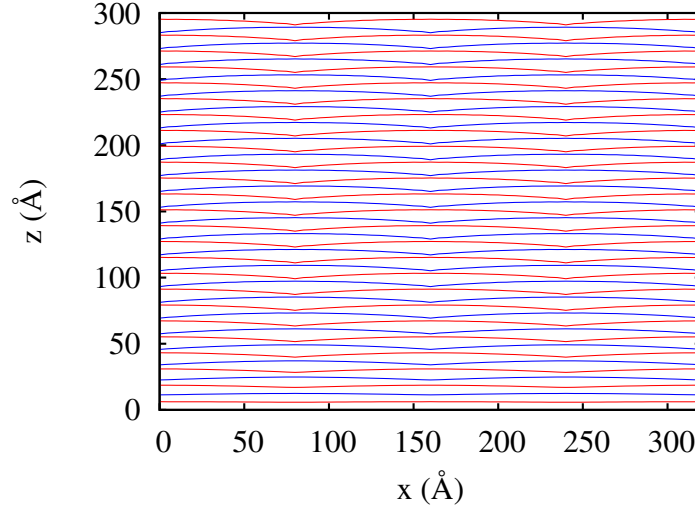


Figure 2.27: The evolution of the multilayer with the CKPZ parameter  $\psi = -250\psi_0$ . Red lines show upper interfaces of InAs layers; blue lines show upper interfaces of AlAs layers. The mean thickness of each layer is 6 Å.

than physical processes. We expect that this region corresponds to the region of the unstable solutions.

We have studied the evolution of the surface in larger systems and effect of the system size to the results. Figures 2.20 and 2.21 show the surface evolution for positive value of CKPZ parameter ( $\psi = 25\psi_0$ ) of the system size  $9\lambda_c$  and  $30\lambda_c$ , respectively. The waves with the critical wavelength  $\lambda_c$  dominate in the early stage. Later its amplitude stops due to the nonlinear effects and the shape changes to the evolution of cones. The stable shape however is not reached. The relatively small cones coalesce together to minimize internal energy. This process was first described by Ostwald [23] and is called Ostwald ripening. The number of cones as function of time is shown in figures 2.25 and 2.26 for the system sizes  $9\lambda_c$  and  $30\lambda_c$ , respectively.

The evolution of the larger system with negative CKPZ parameter  $\psi = -25\psi_0$  is shown in figure 2.22 and 2.23 in the systems of lengths  $9\lambda_c$  and  $30\lambda_c$ , respectively. The evolution in the system with length  $30\lambda_c$  and the parameter of CKPZ parameter  $\psi = -60$  is plotted in figure 2.24. The evolution can be described in the same three stages as with the negative parameter  $\psi$ . In the early stage the most unstable wavelength is predominant. Then in the second stage the growth of modulation amplitude stops and the initially harmonic shape changes to the caps. Then in the last stage the Ostwald ripening process occurs. The dependence of the number of waves on time is plotted in the figures 2.25 and 2.26 along with the dependence for the positive values of the parameter  $\psi$ . The figures show that the ripening process doesn't depend on the particular value of the CKPZ parameter  $\psi$ .

We have also studied the evolution of the multilayers with the CKPZ term. In this case the transformation to exclude the dependence on the layer thickness is not possible. We have performed several simulations for the values of the CKPZ parameter  $\psi = \pm 250\psi_0$  and for the layer thicknesses of  $T = 4, 6, 8$  Å. The value of the lattice mismatch was chosen to be  $\pm 0.05$  for the odd and even layer, respectively. An example of the surface profile is presented in the

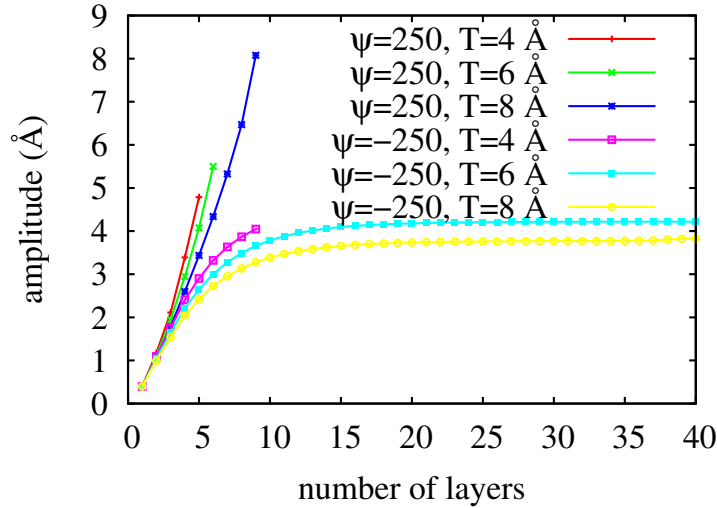


Figure 2.28: Dependence of the modulation amplitude on the number of layers with various values of the CKPZ parameter  $\psi$  and mean thicknesses of the layers  $T$ .

figure 2.27. In the figure 2.28 we have plotted the amplitude dependence on the number of layers for the chosen values of  $\psi$  and  $T$ . Our simulations finished when the growing surface reached the interface beneath i.e., when the growing layer splits into the isolated islands; the amplitude is the difference of the highest and lowest height of the surface. We have found that even for huge positive value of the CKPZ parameter the amplitude of the surface grows with the number of layers and doesn't express any tendency to stabilize the modulation amplitude. For the negative value of CKPZ parameter the stable can be reached if the layer is thick enough.

However, the CKPZ term cannot explain the stabilization of the modulation amplitude during the Stranski-Krastanov growth. The stabilization of the modulation amplitude in the multilayers occurs only for huge negative values of the CKPZ parameter much higher than  $\psi_0$ . It should be noted that the value of the CKPZ parameter  $\psi = \psi_0$  its contribution is comparable to the strain energy density. As for our knowledge there is not any possible physical interpretation of the CKPZ parameter value higher than  $\psi_0$ .

### 2.3.3 Evolution of a system with a wetting effect

The physical interpretation of the CKPZ term can motivate only small values of the CKPZ parameter which could not stabilize the surface evolution. Therefore we have to introduce the wetting effect as a leading nonlinear term. The evolution of a single layer was studied earlier [20, 25, 41, 54].

The main attribute of the wetting effect is its explicit dependence on the layer thickness. The deposition rate then stands as other explicit parameter in the simulation. However this parameter can be well measured and its value is known with very good precision. The evolution of the single layer with the wetting effect however can be divided into the same three stages as the evolution with the CKPZ term. In the early stage the modulation amplitude is much smaller than layer thickness, the contribution of the wetting effect to the chemical potential is neglectable and the critical wavelength is dominant. When the bottom parts of

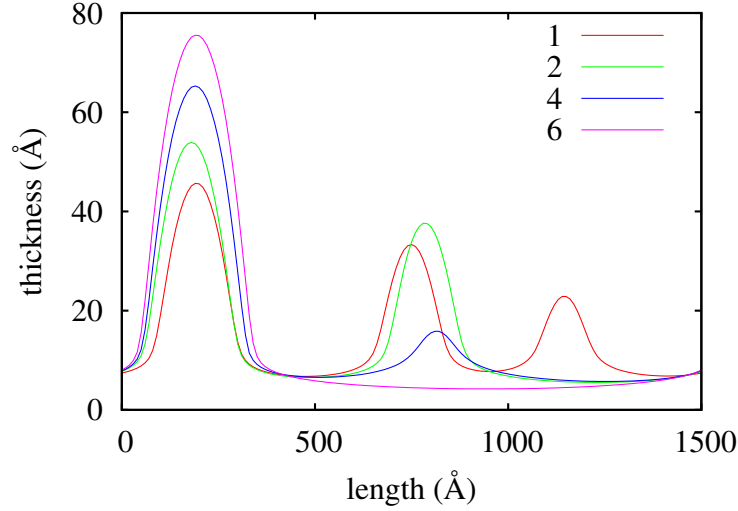


Figure 2.29: The surface evolution of a single layer with wetting effect. Various lines denote the surface profile after depositing 1, 2, 4, and 6 monolayers.

the surface profile come close to the substrate interface the wetting effect stops the growing amplitude. The resulting shape is different to the steady shape with the CKPZ term. The tops evolves into the cones which are similar to the evolution with the positive CKPZ parameter but the bottom develops into the wetting layer which separates the cones. This behavior corresponds to the Stranski-Krastanov growth mode which is observed in almost all semiconductor systems. In the third stage of the growth process the Ostwald ripening occurs. The single layer with the wetting effect finally develops into the isolated cones separated with relatively large wetting layer. The example of the time evolution is shown in the figure 2.29.

In the simulations of the multilayers are further more complicated by the other parameters thickness of individual layers and different physical properties of the layer materials. We were not able to study effects of various parameters in the simulations and we have therefore focused on the simulation of InAs/AlAs on InP system to reproduce our experimental data presented in chapter 3.5.

The simulations have been performed with known material parameters and the surface energy  $\gamma$  was set to be  $1 \text{ Jm}^{-2}$ . The complete list of used material parameters is presented in appendix C. The resulting structure of the interfaces inside the superlattice is shown in Fig. 2.30. From the simulations, the modulation period of  $300 \text{ \AA}$  follows, which is in a good agreement with the observed value  $L_{exp} = (267 \pm 15) \text{ \AA}$ . It should be noted that the simulated modulation period is affected by the size of the simulated region, since there can be only an integer number of the waves in the simulated system of a given size. To eliminate the influence of the system size we have simulated the growth of several systems of sizes 150, 225, 300 and 400 nm. For various system sizes, the modulation periods were always obtained in the interval  $(300 \pm 20) \text{ \AA}$  depending on the particular system size. The modulation amplitude is not affected by the system size.

During the growth of first layers in the stack the modulation amplitude grows exponentially as predicted by the linearized theory [28, 29] (see figure 2.32). In the further growth stage however, the rate of the growth of the modulation amplitude decreases. The results

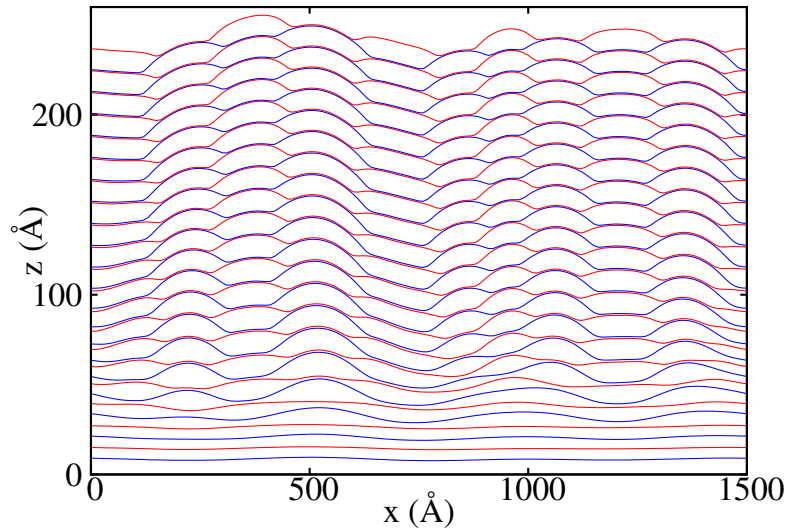


Figure 2.30: The evolution of the multilayers with the wetting effect. Blue lines show upper interfaces of InAs layers red lines show upper interfaces of AlAs layers. The diffusion constant of AlAs is  $2 \times 10^7 \text{ cm}^2\text{s}^{-1}$ .

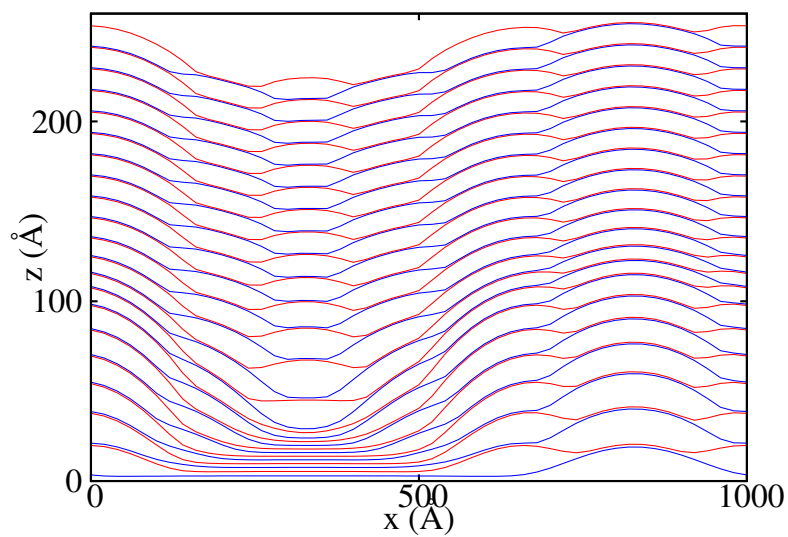


Figure 2.31: The evolution of the multilayers with the wetting effect. Blue lines show upper interfaces of InAs layers red lines show upper interfaces of AlAs layers. The diffusion constant of AlAs was  $2 \times 10^{-10} \text{ cm}^2\text{s}^{-1}$ .

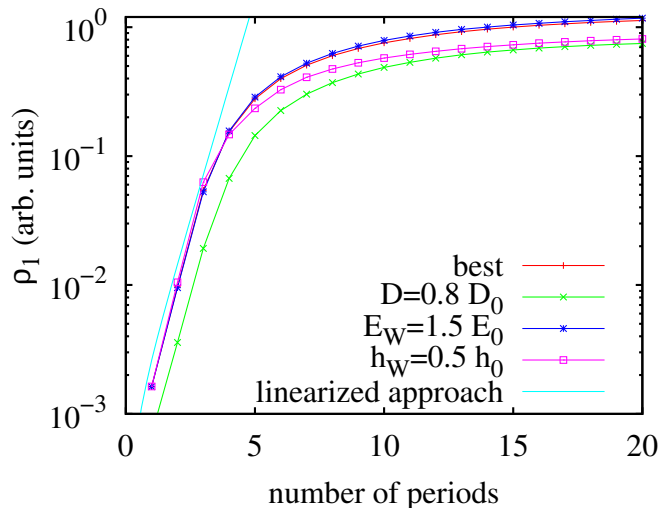


Figure 2.32: The simulated modulation amplitude as a function of the number of layers for various values of the simulation parameters. We show the evolution curve for the best fitted parameters, evolution for  $0.8\times$  slower diffusion rate,  $1.5\times$  higher amplitude of  $E_W$ ,  $0.5\times$  smaller  $h_W$ , and the prediction of the linearized approach [28, 29].

were compared to the values obtained from the x-ray scattering experiment and is presented in the following chapter.

The simulations show a good agreement with the experimental results in spite of the simplified one-dimensional model of the surface used. Transmission electron microscopy (TEM) on similar samples [55] revealed that the modulation is nearly one-dimensional indeed, resulting in a quasiperiodic sequence of quantum wires; this fact explains why the one-dimensional model is sufficient for the simulation of the modulation kinetics. The TEM observations also demonstrated that if the average lattice parameter of the (relaxed) multilayer is larger than that of the InP buffer underneath (the actual multilayer structure is laterally compressed), the modulation direction is close to [100]; if the multilayer is laterally deformed in tension, the modulation direction is close to the crystallographic directions [310] and [130]. Of course, the one-dimensional model used here cannot predict the modulation direction. We ascribe the dependence of the modulation direction on the deformation sign to the anisotropic surface tension and anisotropy in elastic constants [56]. The degree of anisotropy of the surface tension is also affected by the actual strain in the layer [57] and this fact could therefore also explain different modulation directions in the case of a tensile and compressive deformation of the multilayer.

The continuum simulation also allows for the formation of non-physical layers the thickness of which are fractional numbers of monolayers. However, our results based on a continuum approximation are qualitatively similar to the those obtained using an atomistic model and a monolayer step corrugation [13].

The observed and predicted modulation periods roughly correspond to the period given by the linearized theory [28, 29], which prediction is  $L \approx 200 \text{ \AA}$ . It is well-known from the literature that the surface diffusion of In is much faster than Al [58], although exact values of the surface diffusivity of In are not known. In [59] the surface diffusion constant of Al at

530 °C was found to be  $1.5 \times 10^{-7} \text{ cm}^2\text{s}^{-1}$ . The deposition flux of As atoms is higher than the flux of In and Al atoms at usual MBE conditions [60], therefore only diffusivities of Al and In atoms play a role.

On the other hand, our simulations have shown that the values of the diffusion constants have nearly no influence on the modulation amplitude, since the diffusion process is sufficiently quick and the growing surface is nearly in an equilibrium state. The diffusion rate however affects the modulation *period*. In the case of very slow diffusion (in the order of  $10^{-10} \text{ cm}^2\text{s}^{-1}$  for Al), the growth of the larger ripples at the expense of smaller ones (the Ostwald ripening) does not take place and the modulation remains constant during the growth of the whole superlattice stack. If the diffusion is very fast (of the order of  $10^{-7} \text{ cm}^2\text{s}^{-1}$  for Al), the Ostwald ripening takes place during the growth of the first layer already, which leads to the creation of a smaller amount of larger, more distant dots, separated by larger flat areas of a thin wetting layer. The nucleation of the ripples on the subsequent interfaces is affected by the local distribution of lateral strains originated from the large buried ripples. Due to the elastic energy, this distribution gives rise to local minima of the chemical potential at the rims of the buried ripples (two local minima for each ripple) so that the number of the ripples is duplicated. After the deposition of several periods, the ripples cover the whole interface again and the flat areas between the ripples disappear. This process is shown in figure 2.31.

The resulting modulation period is approaching the period obtained for a slow diffusion again.

In our simulations, we have achieved a good correspondence of both the modulation period and the time dependence of the modulation amplitude for any value of the diffusion constant of Al between  $10^{-10}$  and  $10^{-7} \text{ cm}^2\text{s}^{-1}$ ; the diffusion constant of In was chosen 100 times larger than that for Al.

The resulting interface morphology is substantially affected by the wetting-effect, i.e., by a non-linear dependence of the volume density of the elastic energy on the layer thickness. We have approximated this dependence by the equation (2.48). The best correspondence of the measured and simulated modulation amplitudes was obtained for the values  $E_W = 0.15 \times E_0$  and  $h_W = 0.6 \times h_{\text{ml}}$ . We have also estimated these values by means of an atomistic simulation of the elastic energy density using the valence-field force method and the Keating model [39]. In these simulations we have neglected the surface relaxation and reconstruction and we have obtained the dependence of the density of the elastic energy on the thickness of a layer with a flat (001) surface. From the fit of this dependence with exponential formula in equation (2.48) we have obtained  $E_W = 0.10 \times E_0$  and  $h_W = 0.8 \times h_{\text{ml}}$ , which very well corresponds to the values above.

The parameters  $E_W$  and  $h_W$  affect the modulation amplitude and they have no influence on the modulation period. In the first stage of the multilayer growth the modulation amplitude rapidly increases; this increase is slowed down after the growth of about 5 superlattice periods. The parameter  $h_W$  affects mainly the rate of the initial amplitude growth; this rate increases with decreasing  $h_W$ . The parameter  $E_W$  determines the slowing-down process: for larger values of  $E_W$  the slowdown of the amplitude growth is observed earlier than for smaller  $E_W$ .

## Chapter 3

# Theory and results of x-ray scattering

This chapter is divided into five sections. The first section presents the theoretical description of x-ray scattering on laterally modulated superlattices. Next two sections deal with the description of the samples structure and the x-ray diffraction setup. In the fourth section we present the experimental results on the sample with high number of superlattice periods. The last section describes the results on the series of samples with low number of superlattice periods.

### 3.1 X-ray scattering on modulated structures

#### 3.1.1 General description of x-ray diffraction

The theory presented in this section is based on references [12, 61, 62]. The electromagnetic wave in the material without presence of free charges is described by the wave equation

$$\nabla^2 \mathbf{E} = (1 + \chi(\mathbf{r})) \frac{1}{c^2} \frac{\partial^2 \mathbf{E}}{\partial t^2}, \quad (3.1)$$

where  $\mathbf{E}$  is the electric intensity vector,  $c$  is vacuum velocity of light, and  $\chi(\mathbf{r})$  is electric polarizability. We can search the solution in the form  $\mathbf{E}(\mathbf{r}, t) = \mathbf{E}(\mathbf{r})e^{-i\omega t}$ . The wave equation transforms into

$$(\nabla^2 + K^2)\mathbf{E} = -K^2\chi(\mathbf{r})\mathbf{E}, \quad (3.2)$$

where the length of the wave vector is  $K = \frac{\omega}{c}$ . In the following we omit the time factor  $e^{-i\omega t}$ . The plane wave is a solution of the wave equation in vacuum  $\chi = 0$

$$\mathbf{E} = \mathbf{E}_0 e^{i\mathbf{K} \cdot \mathbf{r}}, \quad (3.3)$$

where  $\mathbf{E}_0$  is amplitude and  $\mathbf{K}$  wave vector.

We will introduce Dirac notation as

$$E(\mathbf{r}) = \langle \mathbf{r} | \mathbf{E} \rangle \quad (3.4)$$

and the plane wave with wave vector  $\mathbf{K}$  will be noted as  $|\mathbf{K}\rangle$ . Within Dirac notation the wave equation is

$$\hat{L}|\mathbf{E}\rangle = \hat{V}|\mathbf{E}\rangle, \quad (3.5)$$

where we have defined the operator  $\hat{L} = \nabla^2 + K^2$  and the scattering potential  $\hat{V} = -K^2\chi(\mathbf{r})$ . The scattering of the plane wave  $|\mathbf{K}_0\rangle$  on the scattering potential  $\hat{V}$  can be described using the Green function  $G_0$  of the operator  $\hat{L}$

$$|E\rangle = |\mathbf{K}_0\rangle + G_0\hat{V}|E\rangle.$$

The Green function  $G_0$  is

$$G_0(\mathbf{r} - \mathbf{r}') = -\frac{1}{4\pi} \frac{e^{iK|\mathbf{r}-\mathbf{r}'|}}{|\mathbf{r} - \mathbf{r}'|}. \quad (3.6)$$

Substituting the previous equation into itself we get the infinite series

$$|E\rangle = \left(1 + G_0\hat{V} + G_0\hat{V}G_0\hat{V} + \dots\right) |\mathbf{K}_0\rangle. \quad (3.7)$$

In the first Born approximation (for the x-ray it is called usually kinematical approximation) we take the first term in the infinite series and obtain

$$|E\rangle = \left(1 + G_0\hat{V}\right) |\mathbf{K}_0\rangle. \quad (3.8)$$

Usually the intensity of the scattered wave into the direction  $\mathbf{K}_S$  is detected. The differential cross section of the scattering into this direction is from the quantum theory of scattering

$$\frac{d\sigma}{d\Omega} = \frac{1}{16\pi^2} |\langle \mathbf{K}_S | \hat{V} | \mathbf{K}_0 \rangle|^2. \quad (3.9)$$

The intensity detected at the direction  $\mathbf{K}_S$  is the differential cross section averaged over all inhomogeneities in the sample multiplied with the intensity of the incident beam  $I_0$  and divided by the length from the sample to the detector  $r_{SD}$  for spherical wave

$$I(\mathbf{K}_S) = \frac{I_0}{r_{SD}^2} \left\langle \frac{d\sigma}{d\Omega} \right\rangle. \quad (3.10)$$

The polarizability of the perfect crystal can be expressed as a Fourier series

$$\chi(\mathbf{r}) = \sum_{\mathbf{G}} \chi_{\mathbf{G}} e^{i\mathbf{G}\cdot\mathbf{r}}, \quad (3.11)$$

where  $\mathbf{G}$  is the vector of the reciprocal lattice and  $\chi_{\mathbf{G}}$  is the  $\mathbf{G}$ -th Fourier component of the polarizability. We assume that the polarizability of the deformed crystal can be expressed in a modified Fourier series

$$\chi(\mathbf{r}) = \sum_{\mathbf{G}} \chi_{\mathbf{G}}(\mathbf{r}) e^{i\mathbf{G}\cdot(\mathbf{r}-\mathbf{u}(\mathbf{r}))}, \quad (3.12)$$

where  $\chi_{\mathbf{G}}(\mathbf{r})$  is the  $\mathbf{G}$ -th Fourier component of the polarizability of the material in the position  $\mathbf{r}$  and  $\mathbf{u}$  is the displacement vector. Putting from (3.12) into (3.9) we get the scattered intensity as

$$I(\mathbf{K}_S) = A \left\langle \left| \sum_{\mathbf{G}} \int \chi_{\mathbf{G}}(\mathbf{r}) e^{-i\mathbf{G}\cdot\mathbf{u}(\mathbf{r})} e^{-i(\mathbf{K}_S - \mathbf{K}_0 - \mathbf{G})\cdot\mathbf{r}} d^3\mathbf{r} \right|^2 \right\rangle,$$

where the constant  $A$  stands for  $I_0 \frac{1}{16\pi^2 r_{SD}^2}$ . The vector  $\mathbf{K}_S - \mathbf{K}_0$  is usually denoted as a scattering vector  $\mathbf{Q}$ . The function  $e^{-i(\mathbf{Q}-\mathbf{G})\cdot\mathbf{r}}$  is very fast oscillating function unless  $\mathbf{Q}$  is

closed to  $\mathbf{G}$ . We denote the reciprocal space vector closest to the scattering vector  $\mathbf{Q}$  as  $\mathbf{h}$ . On the other side the functions  $\chi_{\mathbf{G}}(\mathbf{r})$  and  $\mathbf{u}(\mathbf{r})$  are changing much slower with  $\mathbf{r}$  than the oscillating function and the integral of the product of the slowly changing and fast oscillating function is almost zero. We can neglect all the terms in the sum over the reciprocal lattice beside  $\mathbf{G} = \mathbf{h}$

$$I(\mathbf{Q}) = A \left\langle \left| \int \chi_{\mathbf{h}}(\mathbf{r}) e^{-i\mathbf{h}\cdot\mathbf{u}(\mathbf{r})} e^{-i(\mathbf{Q}-\mathbf{h})\cdot\mathbf{r}} d^3\mathbf{r} \right|^2 \right\rangle, \quad (3.13)$$

where we have neglected the terms with the reciprocal lattice vectors  $\mathbf{G}$  far from  $\mathbf{Q}$ .

### 3.1.2 Distorted wave Born approximation

Better results can be obtained by distorted-wave Born approximation (DWBA). In that case we divide the scattering potential into two parts

$$\hat{V} = \hat{V}_A + \hat{V}_B.$$

The first part is such that the wave equation can be solved exactly with the solution  $|E^A\rangle$

$$\hat{L}|E^A\rangle = \hat{V}_A|E^A\rangle. \quad (3.14)$$

The differential cross-section in the DWBA is sum of two terms. The first term corresponds to the scattering on the potential  $\hat{V}_A$  and the second term describes the scattering on the potential  $\hat{V}_B$

$$\frac{d\sigma}{d\Omega} = \frac{1}{16\pi^2} |\langle f|\hat{V}_A|\mathbf{K}_0\rangle + \langle f|\hat{V}_B|i\rangle|^2, \quad (3.15)$$

where the wave  $|i\rangle$  is solution of (3.14) excited by the primary wave  $|\mathbf{K}_0\rangle$ , and the wave  $|f\rangle$  is excited by the scattered wave  $|\mathbf{K}_S\rangle$ . We choose the potential  $\hat{V}_A$  as an amorphous semi-infinite solid

$$\hat{V}_A = -K^2\chi_0 H(-z),$$

where  $H(-z)$  is the Heaviside function (equals 1 for negative  $z$ , and 0 for positive). The solutions of the potential  $\hat{V}_A$  are obtained by the Fresnel coefficients  $r$  and  $t$

$$\langle \mathbf{r}|i\rangle = \begin{cases} e^{i\mathbf{K}_0\cdot\mathbf{r}} + r_i e^{i\mathbf{K}_{0R}\cdot\mathbf{r}} & \text{for } z > 0 \\ t_i e^{i\mathbf{k}_0\cdot\mathbf{r}} & \text{for } z \leq 0 \end{cases} \quad (3.16)$$

$$\langle \mathbf{r}|f\rangle = \begin{cases} e^{i\mathbf{K}_S\cdot\mathbf{r}} + r_f^* e^{i\mathbf{K}_{SR}\cdot\mathbf{r}} & \text{for } z > 0 \\ t_f^* e^{i\mathbf{k}_S^*\cdot\mathbf{r}} & \text{for } z \leq 0 \end{cases}$$

where  $\mathbf{K}_0 = (K_{0x}, K_{0y}, K_{0z})$  is the wave vector of the incident beam,  $\mathbf{K}_{0R} = (K_{0x}, K_{0y}, -K_{0z})$  is the wave vector of the reflected beam,  $\mathbf{k}_0 = (K_{0x}, K_{0y}, k_{0z})$  is the wave vector of the refracted beam, and star denotes the complex adjoint. For the absolute value of the refracted wave vector stands  $|\mathbf{k}_0|^2 = (1 + \chi_0)K^2$ . The wave vectors of the scattered beam have analogous notation. The scattering on the potential  $\hat{V}_A$  is the specular reflection on the surface into the direction  $\mathbf{K}_{0R}$ . In our case we are interested only in the diffuse scattered beam, to which the specular reflected beam does not contribute. The diffuse scattered intensity in DWBA is given by the expression

$$I_{\text{diff}}(\mathbf{Q}) = \text{const.} |t_i t_f|^2 \left\langle \left| \int \chi_{\mathbf{h}}(\mathbf{r}) e^{-i\mathbf{h}\cdot\mathbf{u}(\mathbf{r})} e^{-i\mathbf{q}\cdot\mathbf{r}} d^3\mathbf{r} \right|^2 \right\rangle. \quad (3.17)$$

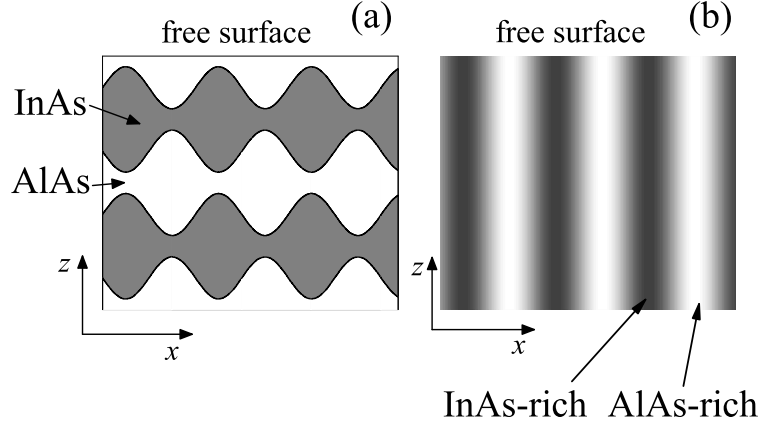


Figure 3.1: The model structure of the superlattice (a) and the composition of the InAs averaged along the axis  $z$ .

We defined the reduced scattering vector  $\mathbf{q} = \mathbf{k}_S - \mathbf{k}_0 - \mathbf{h}$ . The refraction correction also comprises absorption, thus the  $z$ -components of these vectors are complex.

Assuming a perfectly periodic structure along  $x$  with the period  $L$  and independence of the structure on the position along  $y$  axis, the scattered intensity consist of a periodic sequence of  $\delta$ -like peaks (intensity satellites) in the positions  $q_{xp} = p\frac{2\pi}{L}$ , where  $p$  is an integer. The lateral modulation in the real samples is not perfectly periodic, thus, the intensity satellites are smeared. Assuming that deviations from perfectly periodic ordering obey a short-range-order model, the integrated intensities of the satellites are not changed due to the deviations in the first order approximation.

If the structure of the superlattice can be described by a given model, we have calculated the displacement field (see section 2.1), and the integrated intensities of the satellites are given by the expression (3.17).

### 3.1.3 GID on the samples with low number of superlattice periods

Samples with a small number of layers do not have a well evolved structure and it is very hard to find an appropriate structure model. Thus, we have derived an approximative method to determine the structure directly from the measured grazing-incidence scattering data without any previous model. In a grazing-incidence geometry, both the incidence angle  $\alpha_i$  and the exit angle  $\alpha_f$  of the radiation are small, the vertical coordinate  $q_z$  of this reciprocal plane is much smaller than the distance  $\Delta q_z = 2\pi/D$  of the superlattice satellites, where  $D$  is the superlattice period. Therefore, for the purpose of the intensity calculation, the actual superlattice structure can be modeled by a single, vertically homogeneous layer. In this model, the lateral spontaneous modulation of the thicknesses of individual layers is represented by the lateral modulation of the chemical composition of this averaged layer, as shown in figure 3.1.

The amplitude of the scattered wave from the layer is [12]

$$E(\mathbf{q}) = A \sum_m F_m e^{-i\mathbf{q}\cdot\mathbf{r}_m} e^{-i\mathbf{h}\cdot\mathbf{u}_m}, \quad (3.18)$$

where the summation is performed over the unit cells of the layer,  $F_m$  is the structure factor of the unit cell in position  $\mathbf{r}_m$ ,  $\mathbf{u}_m$  is its displacement vector and  $\mathbf{h}$  is the diffraction vector. Deriving equation (3.18) we have assumed the validity of the kinematic approximation and we have neglected the wave diffracted by the substrate underneath.

We denote  $c_m$  the concentration on the In atoms in the unit cell in position  $\mathbf{r}_m$ ;  $c = \langle c_m \rangle$  is the average In content in the layer. In the layer assumed, the concentration  $c_m$  depends only on the in-plane coordinates  $(x_m, y_m)$  and not on the position  $z_m$  in direction perpendicular to the surface. The displacement vector  $\mathbf{u}_m$  is defined with respect to the *averaged* lattice of the layer corresponding to the mean In content  $c$ . The structure factor  $F_m$  is

$$F_m = (1 - c_m)F_{\text{AlAs}} + c_m F_{\text{InAs}} = \langle F \rangle (1 + \delta c_m \xi), \quad \delta c_m = c_m - c,$$

where  $F_{\text{AlAs}}$  and  $F_{\text{InAs}}$  are the structure factors of AlAs and InAs, respectively,  $\langle F \rangle = (1 - c)F_{\text{AlAs}} + cF_{\text{InAs}}$  is the average structure factor, and  $\xi = (F_{\text{InAs}} - F_{\text{AlAs}})/\langle F \rangle$ . In the following we assume that the modulation of the structure factor due to the chemical inhomogeneities is rather shallow, i.e.,  $\delta c_m \xi \ll 1$ . Then

$$F_m \approx \langle F \rangle e^{\delta c_m \xi}. \quad (3.19)$$

Assuming linear elasticity, the displacement vector  $\mathbf{u}(\mathbf{x}_m)$  of the  $m$ -th unit cell can be expressed in the terms of Green functions by the Somigliana equation (2.36). We have neglected the surface relaxation of internal stresses and the volume integral was replaced by the summation thru the unit cells

$$\mathbf{h} \cdot \mathbf{u}(\mathbf{x}_m) = \sum_{j=1}^3 h_j u_j(\mathbf{x}_m) = \sum_{j=1}^3 h_j \sum_n \int_{n\text{-th unit cell}} d\mathbf{x} U_{jk}^{\text{cub}}(\mathbf{x}_m, \mathbf{x}) f_k(\mathbf{x}), \quad (3.20)$$

where  $U_{jk}^{\text{cub}}$  is Green function for cubic material,  $\mathbf{f}(\mathbf{x}_n)$  is density of volume forces, and the integral is performed over the  $n$ -th unit cell. The density of volume forces in the  $n$ -th unit cell is proportional to the local InAs concentration  $c_n$  and is given by the equation (2.19). Far from  $\mathbf{x}_n$  the force contribution of the  $n$ -th lattice cell can be approximated by the point defect

$$f_k(\mathbf{x}) \approx \delta c_n \zeta (C_{11} + 2C_{12}) a^3 \frac{\partial \delta(\mathbf{x} - \mathbf{x}_n)}{\partial x_k}, \quad (3.21)$$

where  $\zeta$  is the lattice mismatch of pure InAs with respect of AlAs,  $a$  is the averaged in-plane lattice constant, and we neglect the dependence of the elastic constants on the chemical composition. Then the scalar product of the displacement vector  $\mathbf{u}$  and diffraction vector  $\mathbf{h}$  can be expressed as using function  $v_{mn}$  containing the elastic Green function

$$\mathbf{h} \cdot \mathbf{u}_m = \sum_n \delta c_n v_{mn}. \quad (3.22)$$

In this case  $v_{mn} \equiv v_{m-n}$  holds. Assuming the chemical composition does not depend on the vertical position in the superlattice stack the displacement vector  $u_m$  depends on  $\mathbf{x}_m \equiv (x_m, y_m)$  only.

The explicit formula for Fourier transform of function  $v_{mn}$  was derived by Dederichs [63]:

$$v^{\text{FT}}(\mathbf{q}_{\parallel}) = -ia^2 \frac{\zeta}{|\mathbf{q}_{\parallel}|} (C_{11} + 2C_{12}) \left[ \sum_{j=x,y} \frac{h_j q_j^0}{C_{44} + H(q_j^0)^2} \right] \left[ 1 + \sum_{j=x,y} \frac{C_{12} + C_{44}}{C_{44} + H(q_j^0)^2} (q_j^0)^2 \right]^{-1}, \quad (3.23)$$

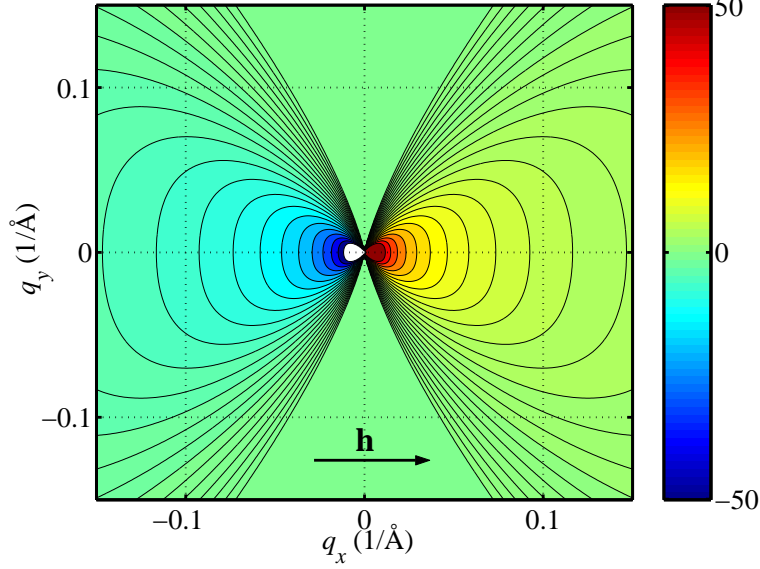


Figure 3.2: Imaginary part of the Green function  $v^{\text{FT}}(\mathbf{q}_{\parallel})$  around diffraction 400.

where  $q_j^0 = q_j/|\mathbf{q}_{\parallel}|$ ,  $j = x, y$ ,  $\mathbf{h} = (h_x, h_y, 0)$  is the diffraction vector parallel to the sample surface, and  $H = C_{11} - C_{12} - 2C_{44}$  is the elastic anisotropy factor ( $H = 0$  for an elastically isotropic continuum). Function  $v^{\text{FT}}(\mathbf{q}_{\parallel})$  is purely imaginary and antisymmetric ( $v^{\text{FT}}(-\mathbf{q}_{\parallel}) = -v^{\text{FT}}(\mathbf{q}_{\parallel})$ ). Figure 3.2 shows the imaginary part of this function calculated in diffraction 400 (diffraction vector  $\mathbf{h}$  parallel to the  $q_x$ -axis).

From equations (3.18) and (3.22) we obtain the following expression for the scattered amplitude

$$E(\mathbf{q}) = A\langle F \rangle \sum_m e^{-i\mathbf{q}\cdot\mathbf{r}_m} \exp\left(-i \sum_n \delta c_n p_{m-n}\right), \quad p_{m-n} = v_{m-n} + i\xi\delta_{mn}, \quad (3.24)$$

$\delta_{mn}$  is the Kronecker delta.

In our model, the local concentration  $c_m$  is a random function of the in-plane position  $\mathbf{x}_m$ . The distribution of the scattered intensity in a plane  $q_z = \text{const}$  averaged over a statistical ensemble of all sets of random values  $\delta c_m$  is

$$I(\mathbf{q}_{\parallel}) = B \sum_{m,m'} e^{-i\mathbf{q}_{\parallel}\cdot(\mathbf{x}_m - \mathbf{x}_{m'})} \left\langle \exp\left[-i \sum_n \delta c_n (p_{m-n} - p_{m'-n}^*)\right] \right\rangle, \quad \mathbf{q}_{\parallel} \equiv (q_x, q_y), \quad (3.25)$$

where the constant  $B$  contains a  $q_z$ -dependent term that is not affected by the lateral modulation of the layer.

The averaging in equation (3.25) can be performed using the cumulant expansion as follows [64]. We define

$$\left\langle \exp\left[-i \sum_n \delta c_n (p_{m-n} - p_{m'-n}^*)\right] \right\rangle \equiv e^{-T_{m-m'}} \quad (3.26)$$

and the function  $T$  can be expanded in the following cumulant series

$$T_{m-m'} = - \sum_{t=1}^{\infty} \frac{(-i)^t}{t!} \kappa_{m-m'}^{(t)}, \quad (3.27)$$

where  $\kappa_{m-m'}^{(t)}$  is the  $t$ -th cumulant. Restricting the cumulant series to the 2nd cumulant only, we obtain

$$\begin{aligned} T_{m-m'} \approx \frac{1}{2} \kappa_{m-m'}^{(2)} &= \frac{1}{2} \sum_{n,n'} \rho_{n-n'} (v_{m-n} - v_{m'-n}) (v_{m-n'} - v_{m'-n'}) - 2i \operatorname{Re} \xi \sum_n \rho_n v_{m'-m+n} \\ &\quad - |\xi|^2 \rho_{m-m'} - \operatorname{Re}(\xi^2) \rho_0 - 2 \operatorname{Im}(\xi) \sum_n \rho_n v_n, \end{aligned} \quad (3.28)$$

where  $\rho_{m-m'} = \langle \delta c_m \delta c_{m'} \rangle$  is the correlation function of the fluctuations of the chemical composition.

In the following, we replace the discrete sums by integrals. The Fourier transformation of the function  $T$  is

$$T^{\text{FT}}(\mathbf{q}_{\parallel}) = \int d^2(\mathbf{x}_m - \mathbf{x}_{m'}) T(\mathbf{x}_m - \mathbf{x}_{m'}) e^{-i\mathbf{q}_{\parallel} \cdot (\mathbf{x}_m - \mathbf{x}_{m'})} = \delta^{(2)}(\mathbf{q}_{\parallel}) T_c + T_{\text{diff}}^{\text{FT}}(\mathbf{q}_{\parallel}); \quad (3.29)$$

the constant term

$$T_c = \int d^2 \mathbf{q}'_{\parallel} \rho^{\text{FT}}(\mathbf{q}'_{\parallel}) [(w^{\text{FT}}(\mathbf{q}'_{\parallel}))^2 - \operatorname{Re}(\xi^2)]$$

appears only in a multiplicative pre-factor in the expression for the scattered intensity, and

$$T_{\text{diff}}^{\text{FT}}(\mathbf{q}_{\parallel}) = -\rho^{\text{FT}}(\mathbf{q}_{\parallel}) |w^{\text{FT}}(\mathbf{q}_{\parallel}) + \xi|^2 \quad (3.30)$$

is the Fourier transformation of the diffuse part  $T_{\text{diff}}(\mathbf{x} - \mathbf{x}')$  of the function  $T(\mathbf{x} - \mathbf{x}')$ . Here we have denoted  $w^{\text{FT}}(\mathbf{q}_{\parallel}) = -iv^{\text{FT}}(\mathbf{q}_{\parallel})/a^2$ ,  $a$  is the averaged lateral lattice parameter of the layer.

The scattered intensity can be divided into two parts. The coherent part of the intensity is concentrated at the crystal truncation rod, i.e., this part is proportional to  $\delta^{(2)}(\mathbf{q}_{\parallel})$ . In the following, we will deal with the diffuse part of the scattered intensity

$$I_{\text{diff}}(\mathbf{q}_{\parallel}) = V \int d^2 \mathbf{x} \int d^2 \mathbf{x}' e^{-i\mathbf{q}_{\parallel} \cdot (\mathbf{x} - \mathbf{x}')} \left[ e^{-T_{\text{diff}}(\mathbf{x} - \mathbf{x}')} - 1 \right], \quad (3.31)$$

where  $V$  is a constant containing  $e^{-T_c}$  among others. Equations (3.30,3.31) will be used for the intensity calculation.

The correlation function  $\rho_{m-m'} \equiv \rho(\mathbf{x}_m - \mathbf{x}_{m'}) = \langle \delta c_m \delta c_{m'} \rangle$  describes the random lateral modulation of the chemical composition of the layer. If the modulation were completely periodic, the correlation function could be expressed by means of a Fourier series

$$\rho(\mathbf{x} - \mathbf{x}') = \sum_{\mathbf{G}} \rho_{\mathbf{G}} e^{i\mathbf{G} \cdot (\mathbf{x} - \mathbf{x}')}, \quad (3.32)$$

where  $\mathbf{G}$  are the vectors of a lattice reciprocal to the two-dimensional lattice of the composition modulation. In reality, the lateral modulation is not exactly periodic and it creates a disordered two-dimensional grid. Let us assume now that the lattice parameter  $2\pi/L$  of

this reciprocal lattice is randomly distributed ( $L$  is the period of the lateral composition modulation). Then the correlation function can be postulated in the form

$$\rho(\mathbf{x} - \mathbf{x}') = \sum_{\mathbf{G}} \rho_{\mathbf{G}} \chi_{\mathbf{G}}(\mathbf{x} - \mathbf{x}'), \quad (3.33)$$

where  $\chi_{\mathbf{G}}(\mathbf{x}) = \int d^2 \mathbf{G}' f_{\mathbf{G}}(\mathbf{G}') \exp(i \mathbf{G}' \cdot \mathbf{x})$  is the two-dimensional characteristic function of the random variable  $\mathbf{G}'$  and  $f_{\mathbf{G}}(\mathbf{G}')$  is its distribution function around the reciprocal lattice point  $\mathbf{G}$ . Then the Fourier transformation  $\rho^{\text{FT}}(\mathbf{q}_{\parallel})$  of the correlation function equals:

$$\rho^{\text{FT}}(\mathbf{q}_{\parallel}) = 4\pi^2 \sum_{\mathbf{G}} \rho_{\mathbf{G}} f_{\mathbf{G}}(\mathbf{q}_{\parallel}). \quad (3.34)$$

Since the distribution function  $f_{\mathbf{G}}(\mathbf{G}')$  is normalized the integrated intensity of the  $\mathbf{G}$ -th satellite of Fourier transformation  $\rho^{\text{FT}}(\mathbf{q}_{\parallel})$  does not depend on the degree of periodicity of the composition modulation and it equals  $4\pi^2 \rho_{\mathbf{G}}$ . This integrated intensity is proportional to the product of the satellite height  $C$  with its width at half maximum (FWHM)  $\delta q$ .

As an example, we calculate the functions  $\rho^{\text{FT}}(\mathbf{q}_{\parallel})$ ,  $T_{\text{diff}}^{\text{FT}}(\mathbf{q}_{\parallel})$  and the resulting intensity distribution  $I_{\text{diff}}(\mathbf{q}_{\parallel})$  around diffraction 400. We assume that the lateral inhomogeneities of the chemical composition create a disordered square lattice with the mean lattice parameter  $\langle L \rangle = 340 \text{ \AA}$ , the distance  $L$  was assumed randomly distributed with the Gamma distribution. Figure 3.3 shows the Fourier transformation of the correlation function  $\rho^{\text{FT}}$ , the Fourier transformation of  $T_{\text{diff}}(\mathbf{x} - \mathbf{x}')$  and the corresponding intensity distribution  $I_{\text{diff}}(\mathbf{q}_{\parallel})$ . In the correlation function  $\rho^{\text{FT}}(\mathbf{q}_{\parallel})$  in panel 3.3 (a) we have neglected the central peak at  $\mathbf{q}_{\parallel} = 0$ , since it has no influence on the shape of the resulting intensity distribution.

The lateral modulation creates a disordered lattice along [100] and [010] creating only 4 satellites of the first order in the map of the correlation function  $\rho^{\text{FT}}(\mathbf{q}_{\parallel})$ ; higher satellites disappear due to the disorder. The Green function  $w^{\text{FT}}(\mathbf{q}_{\parallel})$  consists in two lobes (see figure 3.2) separated by a line of zero values (nodal line) perpendicular to  $\mathbf{h}$ ; therefore, in the function  $T_{\text{diff}}^{\text{FT}}(\mathbf{q}_{\parallel})$  only the satellite maxima lying along [100] are visible – see figure 3.3(d) (i.e., in the direction parallel to  $\mathbf{h}$ ). The other two satellites are suppressed since they lie in the nodal line of  $w^{\text{FT}}$ . This is also the reason, why the resulting intensity distribution in figure 3.3(c) is elongated parallel to  $\mathbf{h}$ . The function  $T_{\text{diff}}^{\text{FT}}$  is a coherent superposition of the antisymmetric function  $w^{\text{FT}}$  with a constant factor  $\xi$ . Since the two lobes of  $w^{\text{FT}}$  differ in sign, this superposition results in an asymmetry of function  $T_{\text{diff}}^{\text{FT}}$  (figure 3.3(b)) and consequently in an asymmetric intensity distribution in figures 3.3(c,d). Therefore, the asymmetry in the intensity distribution in the radial direction (i.e., along  $\mathbf{h}$ ) is a consequence of the interference of a wave scattered from the deformation field with a wave scattered from the inhomogeneities of the structure factor.

### 3.1.4 Direct determination of the correlation function from GID

Formulas (3.30,3.31) make it possible to determine the correlation function  $\rho^{\text{FT}}(\mathbf{q}_{\parallel})$  directly from the measured data without assuming any particular form of the correlation function  $\rho(\mathbf{x} - \mathbf{x}')$ . The procedure consists in the following steps:

1. We calculate the inverse Fourier transformation of the intensity distribution  $I(q_x, q_y) \equiv I(\mathbf{q}_{\parallel})$  (the Patterson function)

$$P(\mathbf{X}) = \frac{1}{4\pi^2} \int d^2 \mathbf{q}_{\parallel} I(\mathbf{q}_{\parallel}) e^{i \mathbf{q}_{\parallel} \cdot \mathbf{X}}. \quad (3.35)$$

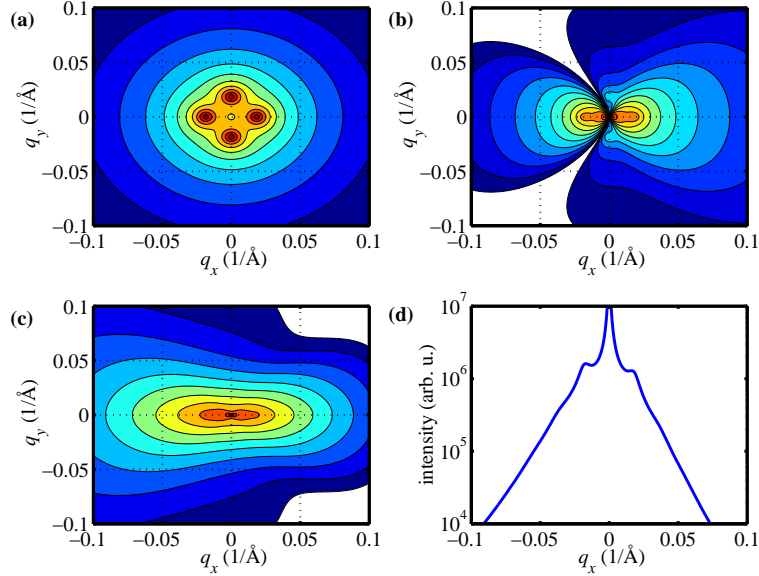


Figure 3.3: The example correlation function  $\rho^{\text{FT}}$  with maxima in the directions of  $q_x$  and  $q_y$  (a). The function  $w^{\text{FT}} + \xi$  around diffraction 400 (b), and the corresponding function  $T^{\text{FT}}$  (c). In the inset (d) is shown the cut through the function  $T^{\text{FT}}$  along  $q_x$  axis.

- From the Patterson function we determine the diffuse part  $T_{\text{diff}}(\mathbf{X})$  of the correlation function using the formula

$$T_{\text{diff}}(\mathbf{X}) = \ln[P(\mathbf{X})] + \text{const.}, \quad (3.36)$$

where the constant is determined so that

$$\lim_{|\mathbf{X}| \rightarrow \infty} T_{\text{diff}}(\mathbf{X}) = 0.$$

- We calculate the Fourier transform

$$T_{\text{diff}}^{\text{FT}}(\mathbf{q}_{\parallel}) = \int d^2 \mathbf{X} T_{\text{diff}}(\mathbf{X}) e^{-i\mathbf{q}_{\parallel} \cdot \mathbf{X}} \quad (3.37)$$

It is worthy to note that the resulting function  $T_{\text{diff}}^{\text{FT}}(\mathbf{q}_{\parallel})$  is real. Knowing this function, using equation (3.30) we can directly determine  $\rho^{\text{FT}}(\mathbf{q}_{\parallel})$ , since the function  $w^{\text{FT}}(\mathbf{q}_{\parallel})$  and the factor  $\xi$  are known. The procedure fails in the points  $\mathbf{q}_{\parallel}$ , where  $|w^{\text{FT}}(\mathbf{q}_{\parallel}) + \xi|^2$  is very small; this is the reason, why two diffractions (400 and 040, for instance) are necessary in order to reconstruct the correlation function  $\rho^{\text{FT}}(\mathbf{q}_{\parallel})$ .

## 3.2 Sample structure and preparation

The samples were prepared by the molecular beam epitaxy (MBE) in Sandia National Laboratory in New Mexico, USA. The superlattice was deposited on a 100 nm thick  $\text{Al}_x\text{In}_{1-x}\text{As}$  buffer layer grown on  $\text{InP}(001)$  substrate. The composition of the buffer layer is set to be the

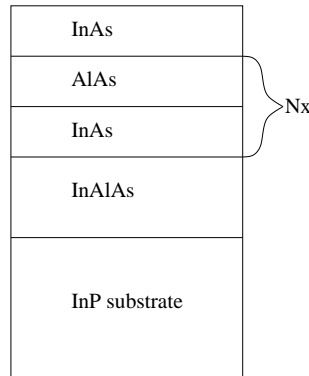


Figure 3.4: The schematic structure of the samples.

same as the average composition of the superlattice stack. Thus the short-period superlattice (SPS) is lattice-matched to the buffer layer and no misfit dislocations in the SPS are present, which was confirmed by TEM [3, 65]. The superlattice consists of thin InAs and AlAs bilayers; the lowest layer is InAs and one additional InAs cap layer is on the top. The schematic structure is shown in figure 3.4.

We have studied samples of two different series. The first sample was named EA532 and it had 100 InAs/AlAs bilayers. The thickness of particular layers in the superlattice were 1.9 mL (monolayers) of InAs and 1.5 mL of AlAs. The sample has a miscut angle of  $\beta = 1.8^\circ$  with the azimuthal direction close to the [100] crystallographic direction. The results of the x-ray diffraction experiments described later in this chapter show that the lateral modulation has a period of  $(280 \pm 10) \text{ \AA}$  and its direction corresponds to the azimuthal miscut direction. In that case three monoatomic steps on surface are present in one lateral period, and the modulation can be formed by the step bunching processes. The sample was deposited by MBE at temperature  $545^\circ\text{C}$  with the deposition rate  $0.35 \text{ mLs}^{-1}$ .

The second type of samples was grown for the investigation of the self-organization process. We have studied the series of samples with 0, 1, 2, 5, 10 and 20 multilayer periods. In the following we note by the number of superlattice periods for easier orientation. For instance the sample with 20 superlattice periods is noted as sample #20. Each multilayer period consisted of 1.9 mL thick InAs layer and 1.9 mL thick AlAs layer. These samples were grown on the InP substrate with small miscut of about  $0.2^\circ$ . The lateral modulation was observed in two perpendicular directions close to  $[310]$  and  $[\bar{1}30]$  with the period of  $(267 \pm 15) \text{ \AA}$  by the x-ray diffraction. This modulation can't be explained by the step bunching process because one monoatomic step corresponds to about three modulation periods. The deposition rate was about  $0.5 \text{ mLs}^{-1}$  and the deposition temperature was  $530^\circ\text{C}$ . The chemical composition of the buffer layer was chosen so that the superlattices were slightly deformed in tension; for our samples, the critical thickness for plastic relaxation and creation of misfit dislocations is about  $0.3 \text{ \mu m}$ , i.e., much larger than the superlattice thickness [66].

### 3.3 X-ray diffraction setup

The x-ray diffraction experiments were performed in two scattering geometries. The measurements were performed at synchrotron ESRF in Grenoble. All the samples were measured in

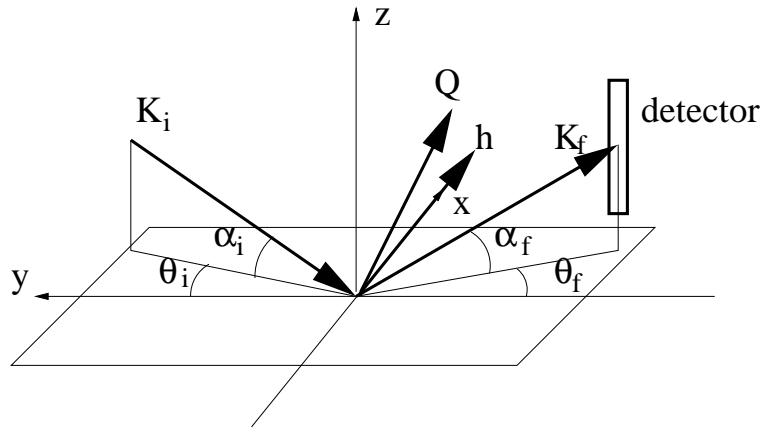


Figure 3.5: Experimental setup for the grazing incidence diffraction. The position sensitive detector is perpendicular to the sample surface. The diffraction vector is parallel to the sample surface.

the grazing-incidence diffraction setup (GID) and the sample with high miscut was measured also in high-angle diffraction (HAD). The grazing-incidence technique measures the diffraction in the planes perpendicular to the surface i.e., with the diffraction vector  $\mathbf{h}$  parallel to the surface (figure 3.3). In this setup the monochromatic and collimated incident beam with the wave vector  $K_i$  forms small angle  $\alpha_i$  to the sample surface. The scattered intensity is usually measured with a position sensitive detector (PSD) parallel to the surface normal. At one position of PSD the dependence of the scattered intensity on the angle  $\alpha_f$  is measured. In the reciprocal space the dependence on  $\alpha_i$  corresponds to the dependence on the  $Q_z$  coordinate. The reciprocal space maps are measured changing the angles  $\theta_i$  and  $\theta_f$ . The angles  $\alpha_i$  and  $\alpha_f$  are very small (around total reflection) and therefore the penetration depth is also small. The penetration depth can be changed by the angles  $\alpha_i$  and  $\alpha_f$  and the information from various depths can be obtained.

The sample with higher miscut was measured at the high-angle diffraction setup (figure 3.3). In the usual coplanar diffraction the incident beam  $\mathbf{K}_i$ , scattered beam  $\mathbf{K}_f$ , and the diffraction vector  $\mathbf{h}$  form plane perpendicular to the sample surface. The reciprocal space map of  $Q_x Q_z$  plane can be quickly measured using PSD perpendicular to the surface – see figure 3.3(a). We have also used an unusual setup with PSD parallel to sample surface – figure 3.3(b). This setup is non-coplanar diffraction because the scattered beam  $\mathbf{K}_f$  does not lay in the plane formed by the incident beam  $\mathbf{K}_i$  and the diffraction vector  $\mathbf{h}$ . The dependence on the angle  $\psi$ , which is measured for one position of PSD, correspond to the line scan along  $Q_y$  axis. The reciprocal space maps in  $Q_x Q_y$  planes for various constant  $Q_z$  were measured.

### 3.4 X-ray diffraction on the sample with higher miscut

This sample was measured on ESRF beamline ID10B using wavelengths 1.540 Å and at the beamline ID01 with an anomalous wavelength 3.366 Å. The wavelength 1.54 Å corresponds to the  $K\alpha$  line of copper, which is common in the laboratory x-ray tubes. At the latter wavelength, AlAs and InAs have the same polarizabilities  $\chi_h$  in diffraction 200 and therefore, the diffracted intensity depends only on the elastic deformation field in the sample and not on

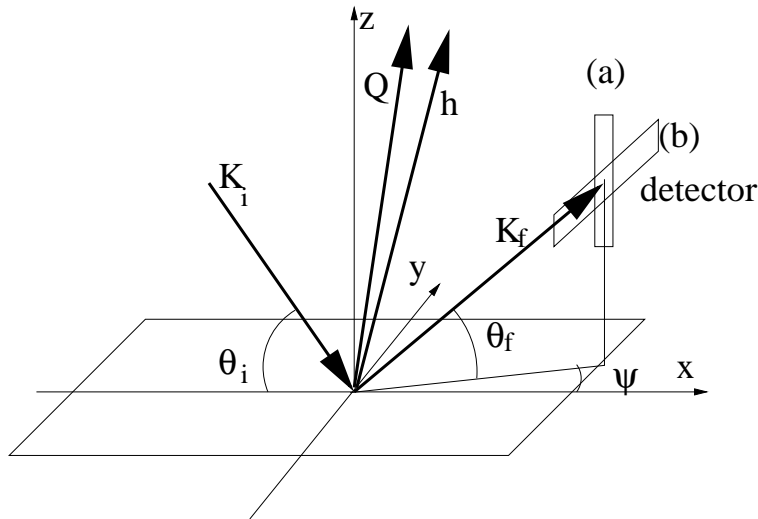


Figure 3.6: Experimental setup for the high-angle diffraction. We have used two positions of the PSD. Position (a) with PSD perpendicular to the sample surface and angle  $\psi = 0$  corresponds to usual coplanar diffraction. In this setup one can measure reciprocal space maps in  $Q_x Q_z$  planes with  $Q_y = 0$ . In the position (b) PSD is parallel to the sample surface and measure dependence of the scattered intensity on the angle  $\psi$ . This setup allows us to measure reciprocal space maps in  $Q_x Q_y$  planes at constant  $Q_z$ .

the chemical composition. The experiments were performed in grazing-incidence diffraction (GID) and in a high-angle x-ray diffraction (HAD) geometry.

The miscut angle of EA532 sample is  $\beta = 1.8 \pm 0.2^\circ$  and the azimuthal direction of the miscut is inclined from  $[100]$  by about  $10^\circ$ . The direction of the LCM exactly coincides with the miscut direction. The period of the LCM was determined from TEM to  $L = 280 \pm 10 \text{ \AA}$ . Three monoatomic steps correspond to one lateral period.

The GID 200 diffraction at  $3.366 \text{ \AA}$  was measured with the PSD oriented perpendicular to the surface, so that one PSD scan represents the dependence of the scattered intensity on the exit angle  $\alpha_f$ . In this diffraction, the in-plane component of the (200) diffraction vector was parallel to the LCM direction. The reciprocal space map with the incidence angle  $\alpha_i = 0.5^\circ$ , and the penetration depth of  $90 \text{ \AA}$  in the coordinates  $Q_x Q_z$  is plotted in figure 3.7(a), the  $Q_x$ -axis is parallel to the in-plane component of the diffraction vector (see figure 3.3 – radial axis). Nearly periodic LCM gives rise to lateral intensity satellites along the LCM direction. Due to local differences in the LCM direction and an azimuthal divergence of the primary beam, the lateral satellites are slightly smeared along  $Q_y$  and it was possible to detect the satellites even for a LCM direction misoriented from  $[100]$ ; up to the  $\pm 3^{\text{rd}}$ -order satellites are visible. Very similar results were obtained for the incidence angle  $\alpha_i = 0.7^\circ$ , corresponding to the penetration depth of about  $500 \text{ \AA}$ . This demonstrates a nearly full vertical homogeneity of the superlattice.

In the XRD experiments at  $\lambda = 3.366 \text{ \AA}$ , the PSD was parallel to the sample surface (figure 3.3). This arrangement made it possible to measure a two-dimensional intensity distribution in a reciprocal plane  $Q_z = \text{const}$  parallel to the sample surface. The reciprocal-intensity map was reconstructed from a series of  $\psi$ -scans taken for various azimuthal directions of the

primary x-ray beam. Three maps at different  $Q_z$  were measured around the symmetrical 002 reciprocal lattice point. In figure 3.7(b), only the map at  $Q_z = 2.136 \text{ \AA}^{-1}$  is plotted, the other maps measured at  $Q_z = 2.12 \text{ \AA}^{-1}$  and  $2.15 \text{ \AA}^{-1}$  are very similar; this confirms again the vertical homogeneity of the sample. In these intensity maps, the lateral satellites can be resolved up to the order of  $\pm 3$ .

Using  $\lambda = 1.54 \text{ \AA}$  and the GID geometry, we have measured a full three-dimensional intensity map around 400 reciprocal lattice point with the penetration depth of about  $210 \text{ \AA}$ , using a PSD perpendicular to the sample surface. In figure 3.8(d) is shown only an extracted line scan through the lateral maxima. In the map, the satellites up to the order  $\pm 4$  are visible. The measurement was performed only to find the exact direction of the LCM modulation.

The XRD measurement at the same wavelength ( $1.54 \text{ \AA}$ ) was performed in the usual setting with the PSD detector perpendicular to the sample surface. This arrangement made it possible to measure the intensity distribution in a vertical reciprocal plane around the asymmetric reciprocal lattice point 404 (figure 3.7(c)). In XRD geometries with both wavelengths, the penetration depth exceeded the total superlattice thickness.

The scattered intensity was detected as a function of the scattering vector  $\mathbf{Q} = \mathbf{K}_f - \mathbf{K}_i$ , where  $\mathbf{K}_{i,f}$  are the wave vectors of incident and scattered beams, respectively. In GID, changing the angle of incidence  $\alpha_i$ , we tune the penetration depth of the incoming radiation, so that we can suppress the scattering in the substrate.

From the intensity maps measured both in the GID and XRD geometries, the mean period of the LCM was determined to  $L = (280 \pm 10) \text{ \AA}$ , which agrees well with TEM observations [65]. From the  $Q_x Q_z$  intensity maps in figure 3.7(c) it is obvious that the row of the lateral satellites is *not* parallel to the sample surface. The profiles of different interfaces in the SPS are replicated; the replication direction is always perpendicular to the row of the satellites in the  $Q_x Q_z$  plane. In our case, the replication direction is tilted by  $\gamma = (4 \pm 1)^\circ$  off the growth direction; the azimuthal direction of this tilt is the same as that of the LCM.

### 3.4.1 Analysis of the experimental data

For the calculation of the elastic displacement field in a SPS with a lateral modulation, we have used a model of monoatomic stairs described in the section 2.1.5 (figure 2.5). From the mean LCM period  $L$  and the miscut angle  $\beta = 1.8 \pm 0.2^\circ$  it follows that three monoatomic steps (and three atomically flat terraces) fit in one LCM period; the widths of these terraces averaged over many LCM periods are denoted  $L_{1,2,3}$ . The obvious relation  $L_1 + L_2 + L_3 = L$  holds.

We assume that all the interfaces in the SPS stack have the same values of  $L_{1,2,3}$ . The positions of the steps at equivalent interfaces are laterally shifted according to the replication angle  $\gamma$  determined from the experimental data. The sequence of the terraces at adjacent InAs/AlAs and AlAs/InAs interfaces are shifted laterally by  $L/2$ ; the shift leads to a lateral modulation of the average chemical composition of the SPS. The structure model is schematically sketched in figure 2.5, where all the model parameters, namely  $L_{1,2,3}, \beta, \gamma$ , are explained. The results of the strain calculation is already shown in the section 2.1.5 along with the comparison of the various strain calculation methods.

Assuming a perfectly periodic structure along  $x$ , the scattered intensity consists of a periodic sequence of  $\delta$ -like peaks (intensity satellites) in the positions  $q_{xp} = \frac{2\pi}{L}p$ , where  $p$  is an integer. In an experimental reciprocal-space map, the peaks are smeared, due to a limited experimental resolution in reciprocal space and due to random deviations from the periodicity

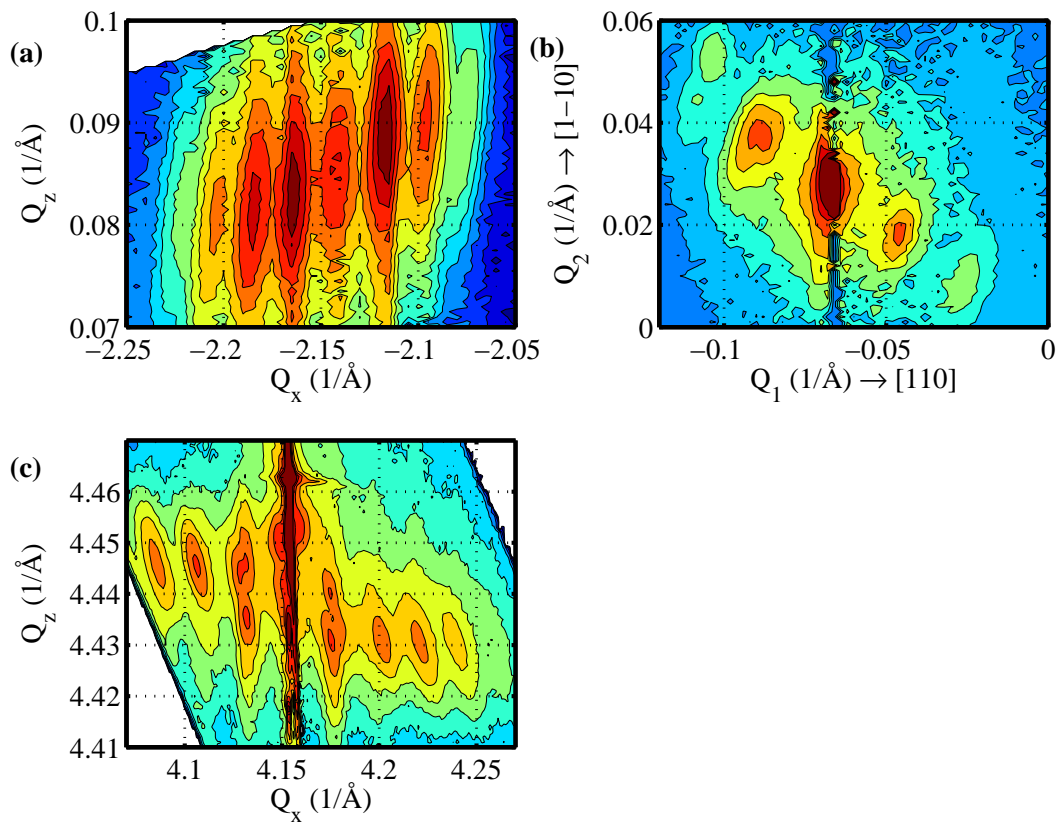


Figure 3.7: Reciprocal space maps around the diffractions 200 (a) and 002 (b) for the wavelength 3.366 Å and diffraction 404 at wavelength 1.54 Å (c). The map in panel (b) is measured with constant  $Q_z = 2.136 \text{ \AA}^{-1}$  and axes  $Q_1$  and  $Q_2$  are parallel to the crystallographic directions [110] and  $[1\bar{1}0]$ , respectively.

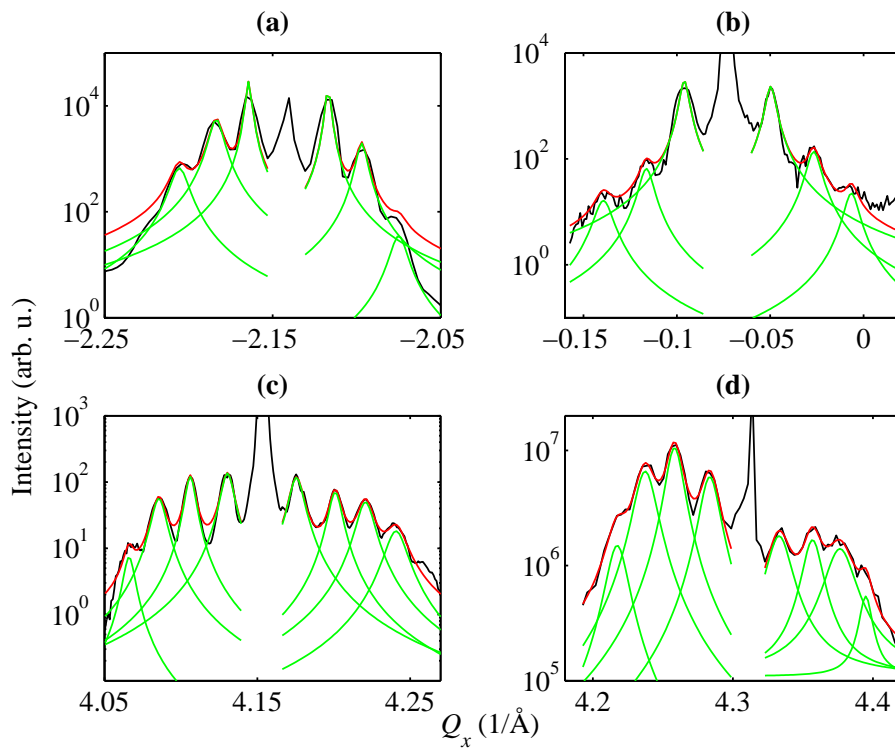


Figure 3.8: The linear cuts through the lateral maxima and their fits with Lorentzian profiles. The scans in panels (a) and (b) are extracted from diffractions 200 and 002 at wavelength  $3.366 \text{ \AA}$ , respectively; the scans in panels (c) and (d) are around diffractions 440 and 400 at wavelength  $1.54 \text{ \AA}$ , respectively. The linear scans in panels (a), (b), and (c) are extracted from the reciprocal space maps plotted in the figure 3.7.

of the LCM. If the deviations obey a short-range-order model, in the first approximation, they do not change the integrated intensities of the satellites. Therefore, we have compared the integrated intensities of the measured lateral satellites with the satellite intensities calculated assuming a perfectly periodic LCM.

The vertical periodicity of the SPS gives rise to superlattice satellites along the  $Q_z$  axis. All our measurements were performed around the zero-order superlattice satellite, thus for  $\text{Re}(q_z) \approx 0$ . Then the intensity of the  $j$ -th lateral satellite is proportional to the square of the  $j$ -th coefficient in the Fourier series of  $\chi(\mathbf{x}) \exp(-i\mathbf{h} \cdot \mathbf{u}(\mathbf{x}))$  along  $x$ . Since the diffraction vector  $\mathbf{h}$  in the GID arrangements is nearly parallel to the sample surface, only the  $u_x$  component affects the scattered intensity in this geometry. In contrast, the intensity diffracted in a symmetric coplanar XRD arrangement depends only on  $u_z$ . Both components of the displacement field influence the reciprocal-space map measured in an asymmetric XRD setup.

From the two- and three-dimensional reciprocal-space maps we have extracted linear scans crossing the lateral satellites. Then, we determined the integrated intensities of these satellites by fitting to a periodic sequence of Lorentzian profiles (figure 3.8). From the fit of these integrated intensities to theoretical values calculated using the FTM method (see chapter 2.1.2), we have determined the widths  $L_{1,2,3}$  of the terraces. Both the measured and the fitted integrated intensities of the lateral satellites are plotted in figure 3.9. For the fit we have used the integrated intensities of the satellites measured in GID and XRD around 200 and 002 reciprocal lattice points, using the wavelength 3.366 Å. The resulting terrace lengths are  $L_1 = 118 \pm 25$  Å,  $L_2 = 120 \pm 24$  Å and  $L_3 = 42 \pm 30$  Å. We have achieved a fairly good correspondence of experimental and calculated data.

Similar procedure was used for the evaluation of GID and XRD measurements in diffractions 400 and 404, respectively, using the wavelength of 1.54 Å, and we have obtained  $L_1 = 121 \pm 6$  Å,  $L_2 = 128 \pm 4$  Å and  $L_3 = 31 \pm 7$  Å. The obvious discrepancy between the experimental and calculated integrated intensities in the coplanar 404 diffraction can be ascribed to the fact that, in this case, the penetration depth of the primary beam exceeds the total SPS thickness; most likely, the intensities of the  $\pm 1^{\text{st}}$  satellites are affected by the diffuse scattering from defects in the buffer layer under the SPS.

In spite of the anomalous nature of the scattering at 3.366 Å, the experiments at the “usual” wavelength of  $\lambda = 1.54$  Å are much more sensitive to the terrace lengths. This is due to the following reasons: (i) The diffraction vector  $\mathbf{h}$  in diffraction 400 is 2 times longer than in 200 and 002; in diffraction 404 even 2.8 times. Since, the displacement field  $\mathbf{u}(\mathbf{r})$  enters the formula (3.17) in the scalar product  $\mathbf{h} \cdot \mathbf{u}$ , the sensitivity of the scattering to the displacement increases with increasing  $|\mathbf{h}|$ . (ii) The polarizability at the wavelength 3.366 Å in diffraction 002 (or 200) does not depend on the chemical composition and therefore the chemical contrast is zero. The non-zero chemical contrast at 1.54 Å contributes to the sensitivity of the scattering process to the terrace lengths.

In Section 2.1.5 we have compared the displacement fields in a short-period laterally-modulated superlattice calculated by a continuum-approximation (FTM) and valence-force field (VFF) methods. Since, in VFF, we have neglected the influence of the free surface and the substrate-SPS interface, this comparison can be performed only in a region far away from these interfaces, where the components of the strain tensor averaged over the superlattice period do not depend on the vertical coordinate  $z$ .

X-ray diffraction intensities were simulated using the FTM-calculated displacement field, since the surface relaxation plays a substantial role, especially in GID, where the penetration

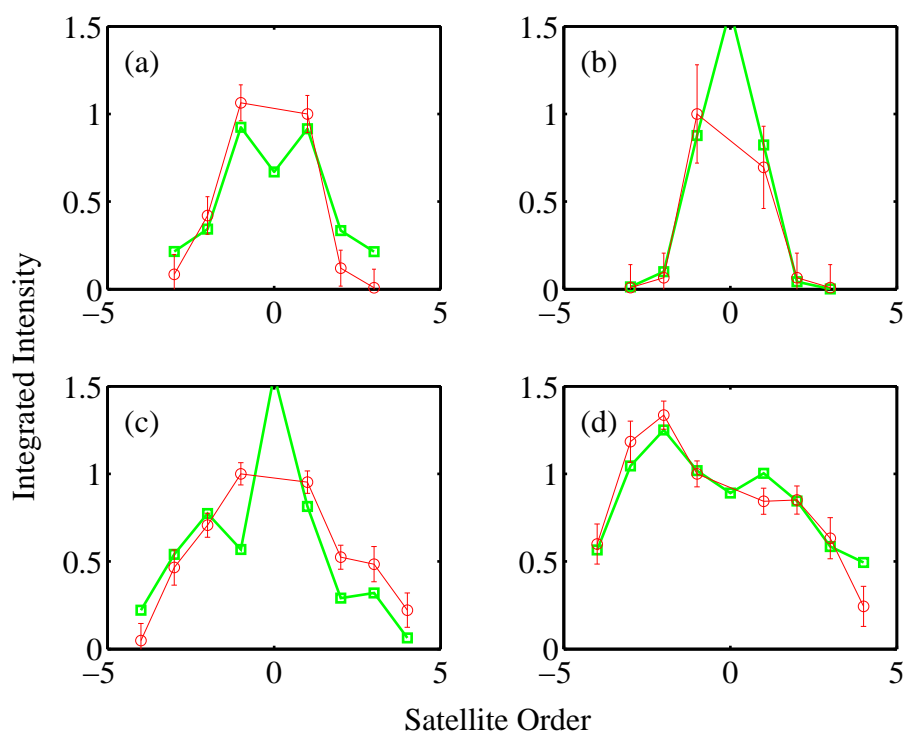


Figure 3.9: Comparison of calculated and measured integral intensities of the lateral satellites. Panel (a) shows satellites for 200 diffraction, (b) 002 for the wavelength 3.366 Å; panel (c) 404, and panel (d) 400 diffraction at wavelength 1.54 Å.

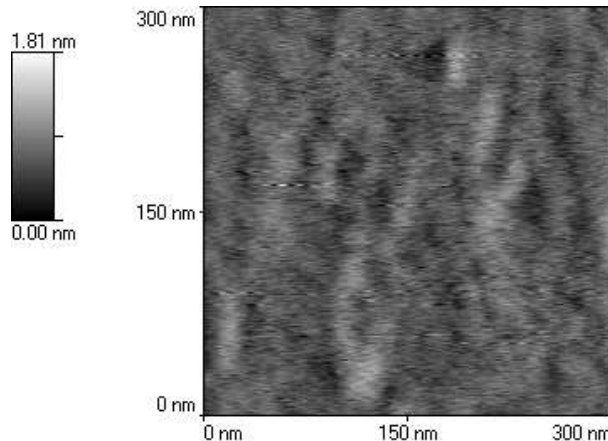


Figure 3.10: Atomic force microscopy image of the sample #20. The resolutions in heights is not clear enough to observe any modulation.

depth of the primary radiation is comparable to the depth, where the surface relaxation takes place.

The structure model used for the evaluation of experimental data neglects a vertical inhomogeneity of the SPS structure, since we have assumed that all the structure parameters  $L_{1,2,3}, \beta, \gamma$  are constant in the superlattice stack. Actually, at the beginning of the superlattice growth, the structure gradually evolves until a stationary growth is reached; this stationary growth mode is observed after the completion of about 10 to 20 bilayers [3, 10]. A possible dispersion of the terrace lengths  $L_{1,2,3}$  and local inhomogeneities of the LCM period broadens the widths of the lateral satellites, in the first approximation, however, the integrated intensities of the satellites remain unchanged. From the widths of the satellites we can estimate the dispersion of the terrace lengths to  $(1000 \pm 500) \text{ \AA}$ .

Our results were compared with results in the work [11], where the LCM was modeled by a *continuous* lateral modulation of the mean chemical composition of the SPS. In the work [11] was found the amplitude of the composition modulation  $\Delta x = (15 \pm 2) \%$ . This result is in a good agreement with the previous work; from the obtained lengths  $L_{1,2,3}$  the value  $\Delta x = (16 \pm 2) \%$  follows.

The consistency of our model is also supported by the agreement of the values of the terrace lengths  $L_{1,2,3}$  obtained by means of various scattering geometries using a “normal” and an anomalous wavelength.

### 3.5 GID diffraction on the series of samples

The samples structure is described in the section 3.2 in the begging of this chapter. The x-ray measurements have been carried out at the beamline ID01 of the European Synchrotron Radiation Facility (ESRF, Grenoble). For all samples, we have measured the intensity distribution of the 400 and 040 diffraction in the  $q_x q_y$  plane of the reciprocal space, i.e., parallel to the sample surface, at  $q_z = \text{const}$ . In order to enhance the surface sensitivity of the scattering and suppress the substrate signal, the angle of incidence of the primary beam was kept constant  $\alpha_i = 0.27 \text{ deg}$ , i.e., just below the critical angle of total external reflection ( $\alpha_c = 0.28 \text{ deg}$ ) for the wavelength used ( $\lambda = 1.5468 \text{ \AA}$ ).

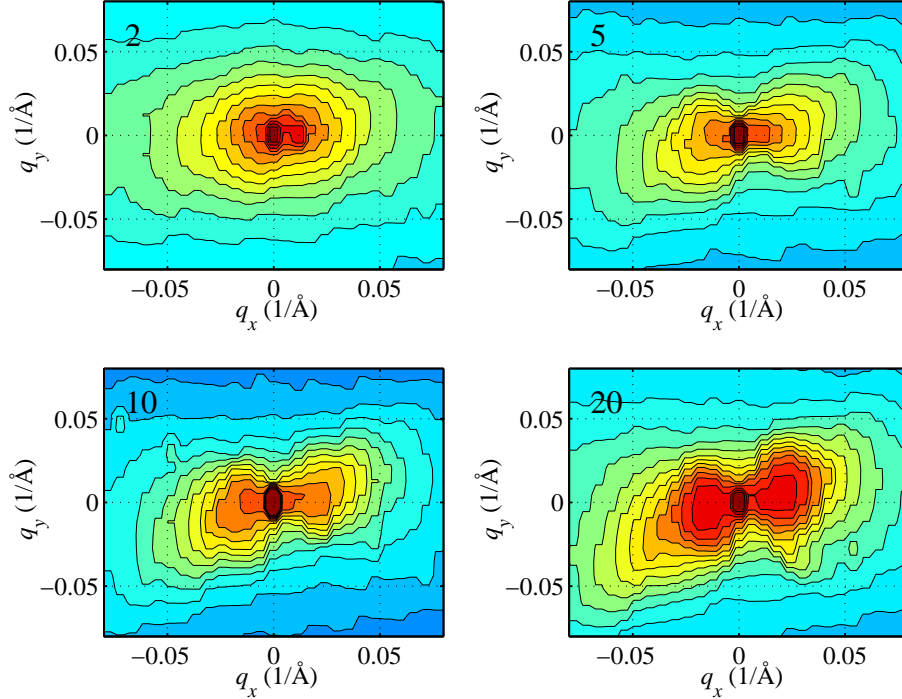


Figure 3.11: 400 grazing incidence x-ray diffraction on the series of samples.

In figure 3.11 we show the reciprocal space maps of all samples taken in diffraction 400, figure 3.12 compares the 400 and 040 reciprocal space maps of sample #20 (i.e., with 20 superlattice periods). In all cases except of the 2-period sample, the intensity distributions exhibit two side maxima in direction few degrees from  $[100]$  and  $[010]$  caused by the periodicity of the composition modulation, in addition to the central maximum (representing a coherent crystal truncation rod). From figure 3.11 it follows that with increasing number of the superlattice periods, the intensity satellites are more pronounced, so that the lateral composition modulation becomes stronger. From the pair of the maps in 400 and 040 diffractions (figure 3.12) it follows that the sample is laterally modulated in two *orthogonal* directions making the angle of about  $(12 \pm 3)$  deg with  $\langle 100 \rangle$  directions, i.e.,  $(6 \pm 3)$  deg with the directions  $[310]$  and  $[\bar{1}30]$ . Similar modulation was found previously for superlattices deformed in tension [10, 55]. In these works however, the two modulation directions  $[310]$  and  $[130]$  were non-orthogonal. The reason for this difference is not clear up to now, it might be caused by the fact that the samples in references [10, 55] have more than hundred of periods.

In this section we use procedure described in the previous section to analyze the experimental data presented in section 3. In the measured maps in figures 3.11 and 3.12 only the side maxima lying on a line nearly parallel to  $\mathbf{h}$  are visible. The other pair of the maxima (on a line nearly perpendicular to  $\mathbf{h}$ ) are suppressed, since the function  $|w^{\text{FT}}(\mathbf{q}_{\parallel}) + \xi|^2$  is rather small here. The asymmetry of the maxima (the maximum at  $q_x < 0$  is larger than that for  $q_x > 0$ ) is caused by the interference of the contributions caused by the scattering from the strain field and from the chemical contrast.

From the maps in figure 3.12 we have calculated the Patterson function  $P(\mathbf{X})$ , the correlation function  $T_{\text{diff}}(\mathbf{X})$  and its Fourier transformation  $T_{\text{diff}}^{\text{FT}}(\mathbf{q}_{\parallel})$  (figure 3.13). A direct

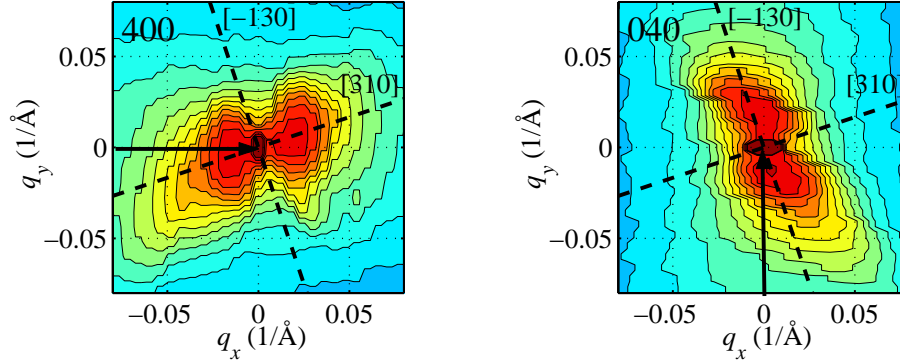


Figure 3.12: The reciprocal space maps of sample #20 of the diffracted intensity measured in diffractions 400 and 040. The diffraction vectors are denoted by the arrows, the dotted lines represent the directions  $[310]$  and  $[\bar{1}30]$ .

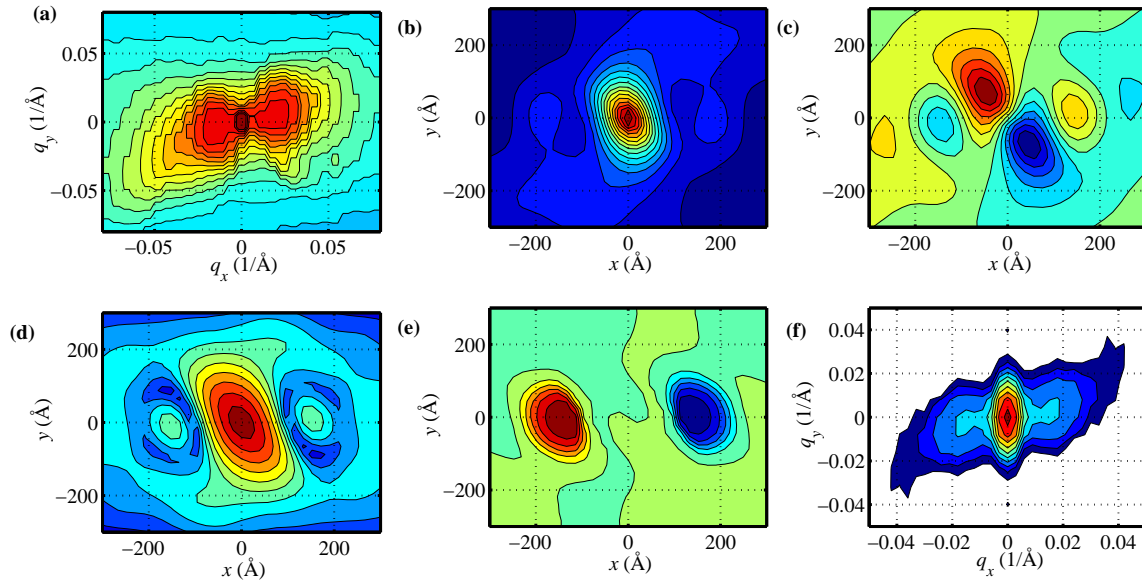


Figure 3.13: The reciprocal space maps of sample #20 of the diffracted intensity measured in diffraction 400 (a), the real part (b) and the imaginary part (c) of the Patterson function  $P(\mathbf{X})$ , the real part (d) and the imaginary part (e) of the function  $T_{\text{diff}}(\mathbf{X})$ , and the symmetric part of the function  $T_{\text{diff,sym}}^{\text{FT}}(\mathbf{q}_{\parallel})$  (f). In (c) and (e), the positive (negative) values are denoted by red (blue) colors, respectively.

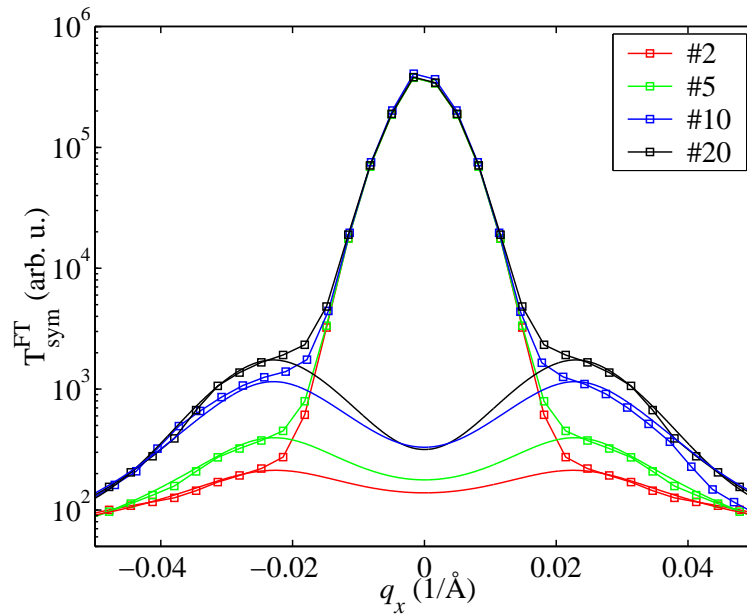


Figure 3.14: The linear scans of the functions  $T_{\text{diff,sym}}^{\text{FT}}(q_{\parallel})$  of samples #2 to #20 extracted along the line crossing the lateral intensity satellites (dots) along with their fits by the Voigt function (lines). The sample #2 is denoted by the red color, #5 green, #10 blue and #20 by black color, respectively.

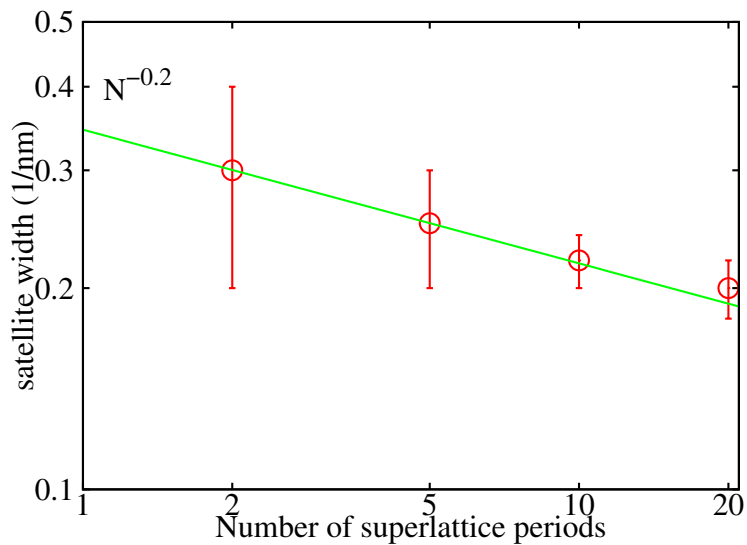


Figure 3.15: The dependence of the lateral widths  $\delta q$  (circles) on the number of the superlattice periods. The line shows a fit by function  $N^{-0.2}$ .

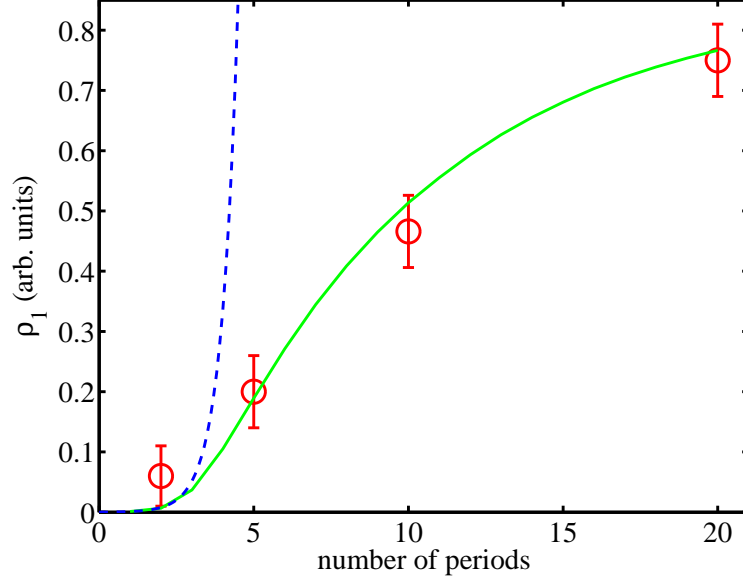


Figure 3.16: The dependence of the lateral satellite amplitude  $\rho_1$  (circles with errorbars) on the number of the superlattice periods. The experimental points are compared to the result of the numerical simulation (green solid line) and to the prediction of the linearized approach [28, 29] (blue dashed line).

calculation of the correlation function  $\rho^{\text{FT}}(\mathbf{q}_{\parallel})$  from  $T_{\text{diff}}^{\text{FT}}(\mathbf{q}_{\parallel})$  using equation (3.30) is not possible, since the division of  $T_{\text{diff}}^{\text{FT}}(\mathbf{q}_{\parallel})$  by the function  $|w^{\text{FT}}(\mathbf{q}_{\parallel}) + \xi|^2$  introduces a very large error in the points  $\mathbf{q}_{\parallel}$ , where this function is very small. However, in order to determine the degree of lateral modulation and its change during the superlattice growth, it is not necessary to extract  $\rho^{\text{FT}}(\mathbf{q}_{\parallel})$  from the measured data. Instead, we use the symmetric part  $T_{\text{diff,sym}}^{\text{FT}}(\mathbf{q}_{\parallel})$  of  $T_{\text{diff}}^{\text{FT}}(\mathbf{q}_{\parallel})$ , plotted in figure 3.13 (f); the lateral maxima of this function are nearly proportional to the maxima of  $\rho^{\text{FT}}(\mathbf{q}_{\parallel})$ . In figure 3.14 we have plotted the functions  $T_{\text{diff,sym}}^{\text{FT}}(\mathbf{q}_{\parallel})$  of all samples, extracted along the lines crossing the side maxima, with their fits by the Voigt functions. Figure 3.15 demonstrates the dependences of the integrated amplitude  $C\delta q$  (i.e., the area below the first satellite maximum in  $T_{\text{diff,sym}}^{\text{FT}}(\mathbf{q}_{\parallel})$ ) and width  $\delta q$  of the satellites on the number of superlattice periods, i.e., on the growth time. A scaling behavior of  $\delta q$  clearly visible. On the other hand, the period of the lateral modulation does not depend on the number of superlattice periods and from the positions of the lateral satellites the mean period of  $\langle L \rangle = (267 \pm 15) \text{ \AA}$  follows.

### 3.5.1 Comparison with growth simulations

The simulations are described in the chapter 2.3.3. The material and deposition parameters are presented in the appendix C. The resulting structure of the interfaces inside the superlattice is shown in Fig. 2.30. From the simulations, the modulation period of  $300 \text{ \AA}$  follows, which is in a good agreement with the experimentally observed value  $L_{\text{exp}} = (267 \pm 15) \text{ \AA}$ .

The simulations show a good agreement with the experimental results in spite of the simplified one-dimensional model of the surface used. Transmission electron microscopy (TEM) on similar samples [55] revealed that the modulation is nearly one-dimensional indeed, result-

ing in a quasiperiodic sequence of quantum wires; this fact explains why the one-dimensional model is sufficient for the simulation of the modulation kinetics. The TEM observations also demonstrated that if the average lattice parameter of the (relaxed) multilayer is larger than that of the InP buffer underneath (the actual multilayer structure is laterally compressed), the modulation direction is close to [100]; if the multilayer is laterally deformed in tension, the modulation direction is close to the crystallographic directions [310] and [130]. Of course, the one-dimensional model used here cannot predict the modulation direction. We ascribe the dependence of the modulation direction on the deformation sign to the anisotropic surface tension and anisotropy in elastic constants [56]. The degree of anisotropy of the surface tension is also affected by the actual strain in the layer [57] and this fact could therefore also explain different modulation directions in the case of a tensile and compressive deformation of the multilayer.

The continuum simulation also allows for the formation of non-physical layers the thickness of which are fractional numbers of monolayers. However, our results based on a continuum approximation are qualitatively similar to the those obtained using an atomistic model and a monolayer step corrugation [13].

In our simulations, we have achieved a good correspondence of both the modulation period and the time dependence of the modulation amplitude for any value of the diffusion constant of Al between  $10^{-10}$  and  $10^{-7}$   $\text{cm}^2\text{s}^{-1}$ ; the diffusion constant of In was chosen 100 times larger than that for Al.

The resulting interface morphology is substantially affected by the wetting-effect, i.e., by a non-linear dependence of the volume density of the elastic energy on the layer thickness. We have approximated this dependence by the equation (2.48). The best correspondence of the measured and simulated modulation amplitudes was obtained for the values  $E_W = 0.15 \times E_0$  and  $h_W = 0.6 \times h_{\text{ml}}$ . We have also estimated these values by means of an atomistic simulation of the elastic energy density using the valence-field force method and the Keating model [39]. In these simulations we have neglected the surface relaxation and reconstruction and we have obtained the dependence of the density of the elastic energy on the thickness of a layer with a flat (001) surface. From the fit of this dependence with exponential formula in equation (2.48) we have obtained  $E_W = 0.10 \times E_0$  and  $h_W = 0.8 \times h_{\text{ml}}$ , which very well corresponds to the values above.

## Chapter 4

# Summary

We have presented three different calculation methods for the strain field inside the short-period superlattices. We have used an analytic Fourier transform method (FTM), boundary integral equations (BIE) method and an atomic valence force field (VFF) method. We have achieved a good coincidence of results obtained by the continuum elasticity (FTM and BIE) methods and the atomic VFF method well even on the system of short-period superlattices. Small differences (locally up to 10% in the values of the strain components) were caused by the neglected of the discrete atomistic nature of the superlattice and by the fact that the continuum method neglects the differences in the elasticity constants of constituting materials and nonlinearity effects. Using VFF method we have also calculated nonlinear dependence of the strain energy density on the layer thickness, which is a substantial part of a wetting effect. The dependence of the strain energy density on the layer thickness can be described by the exponential function.

Using the continuum elasticity BIE method we have performed the nonlinear growth simulations. We have tested our simulation on the system of a single heteroepitaxial layer. The results obtained without the CKPZ term and the wetting effect correspond to the published works [17, 18]. In that case the modulation amplitude increase infinitely and a lattice of cracks is formed in the layer. A mean distance of the cracks corresponds to the critical wavelength  $\lambda_c$  obtained from the linearized theory [14, 15]. Such equation could also describe the Vollmer-Weber growth mode, where the heteroepitaxial layer grown on the substrate is not continuous.

Then we have studied the evolution with the nonlinear CKPZ term. We have found that high positive and negative values can stabilize the unlimited growth of the modulation amplitude. We have also found steady shapes of the surface profile. If the positive value of CKPZ term is taken, one obtains a quasiperiodic lattice of cusps; for the negative value of CKPZ term one obtains a lattice of pits. In the initial stage of growth a mean period of cusps or pits correspond to the critical wavelength  $\lambda_c$ ; in the further stage the pits (cusps) coalesce together in the process similar to the Ostwald ripening. In our simulations we have observed that the modulation period reaches the final value of about  $3\lambda_c$ . We have found that this final period is almost independent on the particular value of the CKPZ parameter. It is not clear if there is a physical reason for this value of the final modulation period. It is possible that a further ripening could occur if the simulation had been performed for much longer time. However, the stabilization of the modulation amplitude occurs only for very high

positive and negative values of the CKPZ term. As for our knowledge, such high values of the CKPZ parameter have no physical interpretation.

The modulation amplitude can be also stabilized in presence of the wetting effect. The initial stage of growth is similar to the growth without the wetting effect. At first, the surface profile finds the critical period  $\lambda_c$ . When the modulation increases the wetting effect stops the modulation. In the latter stage islands separated with the wetting layer of nearly uniform thickness are formed. The process of Ostwald ripening was observed in the simulations with wetting effect. In contrast to the simulations with the CKPZ term we have not observed the final modulation period. If the simulation were carried out for a long time, the final state usually contains only one isolated island. This observation is in a good correspondence to the Ostwald ripening, where no limited size is predicted. The values of the wetting effect parameters necessary to the stabilization of the surface profile are in a good correspondence with the values estimated using the VFF calculation.

The method of continuum simulation was adapted to the system of short-period superlattice. We have studied the effects of the CKPZ term and the wetting to the superlattice morphology. Although the CKPZ parameter stabilizes the modulation amplitude of a single layer for both positive and negative values, only negative values of the CKPZ parameter stabilizes the modulation amplitude. The stabilizing effect was observed only for unphysical values of the CKPZ parameter.

On the other hand, the wetting effect can stabilize the modulation amplitude also in the superlattices. We have performed the simulations with various values of the simulation parameters and studied the influence of various simulation parameters. It was found that the resulting morphology depends mainly on the wetting effect parameters. During the deposition of the first several layers the modulation amplitude rapidly increases in accordance to the linearized theory of the multilayers [28, 29]. After depositing of about 5 superlattice periods the increase of modulation amplitude slows down. The rate of the initial stage growth is also affected by the wetting effect parameter  $h_W$ ; the rate increases with decreasing value of parameter  $h_W$ . The slowing down is affected mainly by the parameter  $E_W$ . Simulating the experimental data we have found the values of the wetting effect parameters in a reasonable agreement with the values estimated using the VFF calculation. On the contrary, the resulting modulation shows only minor dependence on the surface diffusion rate. It is known that the surface diffusion of In is about  $100\times$  faster than Al surface diffusion, although exact value of the surface diffusion constant is known with much lower precision [58]. In our simulations, we have achieved good correspondence with the x-ray scattering experiment for the Al surface diffusion constant between  $10^{-7}$  and  $10^{-10}$   $\text{cm}^2\text{s}^{-1}$ . If the diffusion is slow (in the order of  $10^{-10}$   $\text{cm}^2\text{s}^{-1}$ ) the Ostwald ripening process does not occur. In the slow diffusion case the modulation period is given roughly by the modulation period of the first deposited layer. If the diffusion is fast (in the order of  $10^{-7}$   $\text{cm}^2\text{s}^{-1}$ ) the modulation period of the first layer is of course affected by the Ostwald ripening. It leads to the formation of smaller number large dots. Due to the strain energy two ripples occur on the sides of each large dot during the the growth of next layer. After the deposition of about 4 superlattice periods the ripples cover whole surface. This process remains the modulation period almost unaffected in the whole region of the surface diffusion constant.

Our simplified one-dimensional model is sufficient for the prediction of the modulation amplitude and period of the short-period superlattices. Of course this model cannot explain complete morphology of the superlattice. It is not clear why the lateral modulation shows a direction close to [100] in the In-rich superlattice and [310] and [130] directions in the Al-

rich superlattice. We ascribe this fact to the anisotropy of the physical properties (elastic constants, surface energy density, surface diffusion). To explain the anisotropic properties a complete two-dimensional simulation has to be made. The two-dimensional simulations could be also useful for simulating growth processes of the quantum dots systems. The numerical simulation also cannot predict the widths of lateral satellites observed in the x-ray scattering. The modulation period obtained by the numerical simulations is affected by the size of the simulated system. For the prediction of the satellite width a very large system has to be simulated. We have shown that the modulation amplitude does not depend on the system size and a sufficient prediction of the modulation period can be obtained from simulations performed for several system sizes.

Our simulations do not explain that the quantum dots occur mostly in the layers with a positive lattice mismatch. In our simple model quantum dots can be formed also in the layers with a negative lattice mismatch, because the elastic energy depends on a second power of the lattice mismatch. The behavior of the real systems can be caused by the fact that the surface energy density and its anisotropy depends on the elastic deformation of the layer [56].

Experimental results obtained on two types of sample are presented. The first type was the sample with 100 superlattice periods. On the basis of simulated elastic displacement field we have calculated x-ray diffraction intensities and compared with experiments performed in several geometries and two different wavelengths. We have improved the structure model of a modulated SPS taking this discrete nature of the interfaces into account. We use a discrete model of the interfaces for the analysis of XRD data taken both in coplanar and grazing-incidence geometry (GID). From this comparison we have determined the sizes of the monoatomic terraces constituting the interfaces.

The second studied type was a series of samples with 2, 5, 10, and 20 superlattice periods. The samples in the series were grown under the same deposition conditions. Using grazing-incidence x-ray diffraction, we have investigated the early stages of spontaneous lateral composition modulation. For an analysis of obtained experimental results we have developed an approximative method for the direct determination of the correlation function of the chemical composition from the intensity distribution in the reciprocal space. From the analysis of experimental data it follows that the period of the modulation remains constant during the growth, while the modulation amplitude increases and the periodicity of the modulation improves. This behavior cannot be explained by bunching of monolayer steps and the modulation process is explained by the creation of periodic surface modulation. A scaling behavior was found for the time evolution of the degree of periodicity of the composition modulation. The obtained results were compared to the numerical simulations and we have found good coincidence in both lateral modulation period and the modulation amplitude.

## Appendix A

# Elastic Green function of various systems

The elastic Green functions  $U_{jk}(\mathbf{x}, \mathbf{x}_0)$  and  $T_{jk}(\mathbf{x}, \mathbf{x}_0)$  are defined by the equations (2.34, 2.37). The formula for the three-dimensional Green function of an isotropic solid is known as Kelvin solution [33]

$$U_{jk}^{3D}(\mathbf{x}_0 - \mathbf{x}) = \frac{1}{16\pi\mu(1-\nu)r} \left[ (3-4\nu)\delta_{jk} + \frac{\partial r}{\partial x_j} \frac{\partial r}{\partial x_k} \right], \quad (\text{A.1})$$

where  $r = |\mathbf{x}_0 - \mathbf{x}|$  and the traction Green function is

$$T_{jk}^{3D}(\mathbf{x}_0 - \mathbf{x}) = -\frac{1-2\nu}{8\pi(1-\nu)r^2} \left[ \sum_{l=1}^3 \frac{\partial r}{\partial x_l} n_l \left( \delta_{jk} + \frac{3}{1-2\nu} \frac{\partial r}{\partial x_j} \frac{\partial r}{\partial x_k} \right) + \frac{\partial r}{\partial x_j} n_k - \frac{\partial r}{\partial x_k} n_j \right]. \quad (\text{A.2})$$

In the general case of an anisotropic solid the Green function can be expressed in terms of an integral [67, 68]

$$U_{jk}(\mathbf{x}_0 - \mathbf{x}) = \frac{1}{8\pi r} \int_0^{2\pi} Q_{jk}^{-1}(\psi) d\psi, \quad (\text{A.3})$$

where  $\hat{Q}^{-1}(\psi)$  is an inverse matrix to the matrix

$$Q_{jl}(\psi) = \sum_{k,m} C_{jklm} (n_k \cos \psi + s_k \sin \psi) (n_m \cos \psi + s_m \sin \psi)$$

and unit vectors  $\mathbf{x}/r, \mathbf{n}, \mathbf{s}$  form a right-handed orthonormal system. The solution for hexagonal system was found by Lifshitz and Rosenzweig [67]. For cubic crystal were found only several approximative formulas [67, 68, 69]. However for cubic crystal exists simple formula for its Fourier transform[69]:

$$U_{jk}^{\text{FT}}(\mathbf{q}) = \frac{1}{|\mathbf{q}|^2} \left\{ \frac{\delta_{jk}}{C_{44} + H(q_j^0)^2} - \frac{q_j^0 q_k^0 (C_{12} + C_{44})}{(C_{44} + H(q_j^0)^2)(C_{44} + H(q_k^0)^2)} \left[ 1 + \sum_{l=x,y,z} \frac{C_{12} + C_{44}}{C_{44} + H(q_l^0)^2} (q_l^0)^2 \right]^{-1} \right\}, \quad (\text{A.4})$$

where  $q_j^0 = q_j/|\mathbf{q}|$  and  $H = C_{11} - C_{12} - 2C_{44}$  is the elastic anisotropy factor ( $H = 0$  for an elastically isotropic continuum).

If we assume that the structure does not depend on the position along axis  $y$  and the material is isotropic solid, we could use the Green function of the two-dimensional solid (see e.g., [31, 70])

$$U_{jk}^{2D}(\mathbf{x}_0, \mathbf{x}) = -\frac{1}{8\pi\mu(1-\nu)} \left[ (3-4\nu)\ln(r)\delta_{jk} - \frac{\partial r}{\partial x_j} \frac{\partial r}{\partial x_k} \right], \quad (\text{A.5})$$

$$T_{jk}^{2D}(\mathbf{x}_0, \mathbf{x}) = \sum_{l=x,z} S_{jkl}^{2D}(\mathbf{x}_0, \mathbf{x})n_l(\mathbf{x}), \quad (\text{A.6})$$

$$S_{jkl}^{2D}(\mathbf{x}_0, \mathbf{x}) = -\frac{1}{4\pi(1-\nu)r} \left[ (1-2\nu) \left( \frac{\partial r}{\partial x_l} \delta_{jk} + \frac{\partial r}{\partial x_k} \delta_{jl} - \frac{\partial r}{\partial x_j} \delta_{kl} \right) + 2 \frac{\partial r}{\partial x_j} \frac{\partial r}{\partial x_k} \frac{\partial r}{\partial x_l} \right]. \quad (\text{A.7})$$

Assuming that the system is periodic along  $x$  axis with period  $L$ , the integration along the whole boundary can be replaced by integration over just one period with the periodic Green functions

$$\begin{aligned} \int_{x=-\infty}^{\infty} d\mathbf{x} U_{jk}^{2D}(x_0, z_0, x, z) t_k(x, z) &= \sum_{m=-\infty}^{\infty} \int_{x=0}^L d\mathbf{x} U_{jk}^{2D}(x_0, z_0, x+mL, z) t_k(x, z) = \\ &= \int_{x=0}^L d\mathbf{x} U_{jk}^L(x_0, z_0, x, z) t_k(x, z), \end{aligned} \quad (\text{A.8})$$

where

$$U_{jk}^L(x_0, z_0, x, z) = \sum_{m=-\infty}^{\infty} U_{jk}^{2D}(x_0, z_0, x+mL, z) \quad (\text{A.9})$$

and an analogous procedure can be performed for  $T_{jk}$

$$T_{jk}^L(x_0, z_0, x, z) = \sum_{m=-\infty}^{\infty} T_{jk}^{2D}(x_0, z_0, x+mL, z) \quad (\text{A.10})$$

These infinite sums can be calculated analytically [17]:

$$\begin{aligned} U_{xx} &= A \left[ \frac{3-4\nu}{2} \ln(\cosh Z - \cos X) + \frac{1}{2} Z \frac{\sinh Z}{\cosh Z - \cos X} \right] \\ U_{xz} &= -A \frac{1}{2} Z \frac{\sin X}{\cosh Z - \cos X} \\ U_{zx} &= U_{xz} \\ U_{zz} &= A \left[ \frac{3-4\nu}{2} \ln(\cosh Z - \cos X) - \frac{1}{2} Z \frac{\sinh Z}{\cosh Z - \cos X} \right] \end{aligned} \quad (\text{A.11})$$

$$\begin{aligned}
S_{xxx} &= B \frac{\pi}{L} \left[ (3 - 2\nu) \frac{\sin X}{\cosh Z - \cos X} - Z \frac{\sinh Z \sin X}{(\cosh Z - \cos X)^2} \right] \\
S_{zzz} &= B \frac{\pi}{L} \left[ 2(1 - \nu) \frac{\sinh Z}{\cosh Z - \cos X} + Z \frac{\cosh Z \cos X - 1}{(\cosh Z - \cos X)^2} \right] \\
S_{xzz} &= B \frac{\pi}{L} \left[ -(1 - 2\nu) \frac{\sin X}{\cosh Z - \cos X} + Z \frac{\sinh Z \sin X}{(\cosh Z - \cos X)^2} \right] \\
S_{zxx} &= B \frac{\pi}{L} \left[ 2\nu \frac{\sinh Z}{\cosh Z - \cos X} - Z \frac{\cosh Z \cos X - 1}{(\cosh Z - \cos X)^2} \right] \\
S_{xxz} &= B \frac{\pi}{L} \left[ 2(1 - \nu) \frac{\sinh Z}{\cosh Z - \cos X} - Z \frac{\cosh Z \cos X - 1}{(\cosh Z - \cos X)^2} \right] \\
S_{zxx} &= B \frac{\pi}{L} \left[ (1 - 2\nu) \frac{\sin X}{\cosh Z - \cos X} + Z \frac{\sinh Z \sin X}{(\cosh Z - \cos X)^2} \right] \\
S_{xxx} &= S_{xxz} \\
S_{zzz} &= S_{zxx},
\end{aligned} \tag{A.12}$$

where  $A = -\frac{1}{8\pi(1-\nu)\mu}$ ,  $B = -\frac{1}{4\pi(1-\nu)}$ ,  $X = 2\pi \frac{x-x_0}{L}$ , and  $Z = 2\pi \frac{z-z_0}{L}$ . The sums were calculated using following analytical sums [71]

$$\sum_{n=-\infty}^{\infty} \frac{n+p}{q^2 + (n+p)^2} = \frac{\pi \sin(2\pi p)}{\cosh(2\pi q) - \cos(2\pi p)} \tag{A.13}$$

$$\sum_{n=-\infty}^{\infty} \frac{1}{q^2 + (n+p)^2} = \frac{\pi}{q} \frac{\sinh(2\pi q)}{\cosh(2\pi q) - \cos(2\pi p)} \tag{A.14}$$

$$\sum_{n=-\infty}^{\infty} \frac{q^2 - (n+p)^2}{[q^2 + (n+p)^2]^2} = 2\pi^2 \frac{\cosh(2\pi q) \cos(2\pi p) - 1}{[\cosh(2\pi q) - \cos(2\pi p)]^2} \tag{A.15}$$

$$\sum_{n=-\infty}^{\infty} \frac{n+p}{[q^2 + (n+p)^2]^2} = \frac{\pi^2}{q} \frac{\sinh(2\pi q) \sin(2\pi p)}{[\cosh(2\pi q) - \cos(2\pi p)]^2} \tag{A.16}$$

$$\sum_{n=-\infty}^{\infty} \ln [q^2 + (n+p)^2] = \ln [\cosh(2\pi q) - \cos(2\pi p)]. \tag{A.17}$$

# Appendix B

## List of symbols

### Symbols used in the evolution equation

Position vector	$\mathbf{x} \equiv \mathbf{r}$
Surface height, layer thickness	$h$
Chemical potential on the surface	$\mu_S$
Surface diffusion constant	$D_S$
Surface tension	$\gamma$
Surface curvature	$\kappa$
Strain energy density	$E_S$
Atomic volume	$\Omega$
Deposition rate, deposition noise	$F, \eta$
Wetting effect amplitude and thickness	$E_W, h_W$
Critical modulation period	$\lambda_c$

### Symbols used in a strain field calculation

Displacement vector	$\mathbf{u}$
Strain tensor	$\epsilon_{jk}$
Stress tensor	$\sigma_{jk}$
Density of volume forces	$\mathbf{f}$
Displacement and traction Green function	$U_{jk}(\mathbf{x}_0, \mathbf{x}), T_{jk}(\mathbf{x}_0, \mathbf{x})$
Surface normal	$\mathbf{n}$
Surface traction	$\mathbf{t}$
Lattice mismatch	$\zeta$
Elastic shear modulus and Poisson ratio	$\mu, \nu$
Elastic constants in cubic material	$C_{11}, C_{12}, C_{44}$

### Symbols used in the x-ray scattering

Wave vector	$\mathbf{K}$
Reciprocal lattice vector, diffraction vector	$\mathbf{G}, \mathbf{h}$
Scattering vector, reduced scattering vector	$\mathbf{Q}, \mathbf{q}$
Scattered intensity	$I$
Local InAs concentration	$c$
Correlation function and its first Fourier component	$\rho, \rho_1$
Susceptibility	$\chi$
Modulation period	$L$

## Appendix C

# Table of simulation parameters

### Material constants

Surface tension	$\gamma$	$1 \text{ Jm}^{-2}$
AlAs shear modulus	$\mu_{\text{AlAs}}$	$3.1 \times 10^{10} \text{ Pa}$
InAs shear modulus	$\mu_{\text{InAs}}$	$1.9 \times 10^{10} \text{ Pa}$
AlAs Poisson ratio	$\nu_{\text{AlAs}}$	0.32
InAs Poisson ratio	$\nu_{\text{InAs}}$	0.35
AlAs surface diffusion constant (530 °C)	$D_S$	$10^{-7} - 10^{-10} \text{ cm}^2\text{s}^{-2}$
InAs surface diffusion constant (530 °C)	$D_S$	$10^{-5} - 10^{-8} \text{ cm}^2\text{s}^{-2}$
AlAs lattice parameter	$a_{\text{AlAs}}$	$5.6618 \text{ \AA}$
InAs lattice parameter	$a_{\text{InAs}}$	$6.0360 \text{ \AA}$
InP lattice parameter	$a_{\text{InP}}$	$5.8687 \text{ \AA}$
AlAs/InP lattice mismatch	$\zeta_{\text{AlAs}}$	-0.0354
InAs/InP lattice mismatch	$\zeta_{\text{InAs}}$	0.0323
Wetting energy	$E_W$	$0.10 E_0$
Wetting thickness	$h_W$	$0.8 h_{ML}$

### Deposition conditions

Deposition temperature	$T$	$530 \text{ }^\circ\text{C}$
Deposition rate	$F$	$1 \text{ \AA s}^{-1}$
Standard deviation of deposition noise	$\eta$	$0.5 \text{ \AA s}^{-1}$

# Bibliography

- [1] J. H. Davies, *The physics of low-dimensional semiconductors – An introduction* (Cambridge University Press, 1998).
- [2] C. Weisbuch and B. Vinter, *Quantum semiconductor structures* (Academic Press, Inc., San Diego, 1991).
- [3] J. Mirecki-Millunchick, R. D. Twosten, D. M. Follstaedt, S. R. Lee, E. D. Jones, Y. Zhang, S. P. Ahrenkiel, and A. Mascarenhas, *Appl. Phys. Lett.* **70**, 1402 (1997).
- [4] K. Y. Cheng, K. C. Hsieh, and J. N. Baillargeon, *Appl. Phys. Lett.* **60**, 2892 (1992).
- [5] D. M. Follstaedt, R. D. Twosten, J. Mirecki-Millunchick, S. R. Lee, E. D. Jones, S. P. Ahrenkiel, Y. Zhang, and A. Mascarenhas, *Physica E* **2**, 325 (1998).
- [6] A. G. Norman *et al.*, *Appl. Phys. Lett.* **73**, 1844 (1998).
- [7] E. D. Jones, J. Mirecki-Millunchick, D. Follstaedt, S. Lee, J. Reno, R. D. Twosten, Y. Zhang, and A. Mascarenhas, *Physica E* **2**, 44 (1998).
- [8] S. Francoer, A. G. Norman, M. C. Hanna, A. Mascarenhas, J. L. Reno, D. M. Follstaedt, and S. R. Lee, *Mat. Sci. Eng. B* **88**, 118 (2002).
- [9] J.-H. Li, V. Holý, Z. Zhong, J. Kulik, S. C. Moss, A. G. Norman, A. Mascarenhas, J. L. Reno, and D. M. Follstaedt, *Appl. Phys. Lett.* **78**, 219 (2001).
- [10] A. G. Norman *et al.*, *Mat. Res. Soc. Proc.* **583**, 297 (2000).
- [11] J.-H. Li, V. Holý, M. Meduňa, S. C. Moss, A. G. Norman, A. Mascarenhas, and J. L. Reno, *Phys. Rev. B* **66**, 115312 (2002).
- [12] J. Stangl, V. Holý, and G. Bauer, *Rev. Mod. Phys.* **76**, 725 (2004).
- [13] L. Bai, J. Tersoff, and F. Liu, *Phys. Rev. Lett.* **92**, 225503 (2004).
- [14] R. J. Asaro and W. A. Tiller, *Metall. Trans.* **3**, 1789 (1972).
- [15] M. A. Grinfeld, *Sov. Phys. Dokl.* **31**, 831 (1986).
- [16] D. J. Srolovitz, *Acta Metall.* **37**, 621 (1989).
- [17] W. H. Yang and D. J. Srolovitz, *J. Mech. Phys. Solids* **42**, 1551 (1994).
- [18] B. J. Spencer and D. I. Meiron, *Acta Metall. Mater.* **42**, 3629 (1994).

- [19] D. E. Jesson, S. J. Pennycook, J.-M. Baribeau, and D. C. Houghton, *Scanning Microscopy* **8**, 849 (1994).
- [20] B. J. Spencer, *Phys. Rev. B* **59**, 2011 (1999).
- [21] J. Tersoff, *Phys. Rev. B* **43**, 9377 (1991).
- [22] T. V. Savina, P. W. Voorhees, and S. H. Davis, *J. Appl. Phys.* **96**, 3127 (2004).
- [23] W. Ostwald, *Z. Phys. Chem. (Leipzig)* **34**, 495 (1990).
- [24] W. Seifert, N. Carlsson, M. Miller, M. E. Pistol, L. Samuelson, and L. R. Wallenberg, *Progr. Cryst. Growth and Charact.* **33**, 423 (1996).
- [25] H. R. Eisenberg and D. Kandel, *Phys. Rev. B* **71**, 115423 (2005).
- [26] B. J. Spencer, P. W. Voorhees, and J. Tersoff, *Phys. Rev. B* **64**, 235318 (2001).
- [27] P. Venezuela, J. Tersoff, J. A. Floro, E. Chason, D. M. Follstaedt, F. Liu, and M. G. Lagally, *Nature* **397**, 678 (1999).
- [28] L. E. Shilkrot, D. J. Srolovitz, and J. Tersoff, *Phys. Rev. B* **62**, 8397 (2000).
- [29] Z. F. Huang and R. C. Desai, *Phys. Rev. B* **67**, 075416 (2003).
- [30] T. Roch, V. Holý, A. Hesse, J. Stangl, T. Fromherz, G. Bauer, T. H. Metzger, and S. Ferrer, *Phys. Rev. B* **65**, 245324 (2002).
- [31] A. M. Linkov, *Boundary integral equations in elasticity theory* (Kluwert Academic Publishers, Dordrecht, 2002).
- [32] R. M. Martin, *Phys. Rev. B* **1**, 4005 (1970).
- [33] L. D. Landau and I. M. Lifshitz, *Teoria uprugosti* (Nauka, Moscow, 1986), In russian.
- [34] J. Balaš, J. Sládek, and V. Sládek, *Analýza napětí metodou hraničných integrálních rovnic* (Veda, Bratislava, 1985), In slovak, English translation: *Stress analysis by boundary element methods* (Elsevier, 1989).
- [35] J. F. Luo, Y. J. Liu, and E. J. Berger, *Comp. Mech.* **24**, 448 (2000).
- [36] Y. J. Liu, N. Xu, and J. F. Luo, *J. Appl. Mech.* **67**, 41 (2000).
- [37] W. H. Press, S. A. Teukolsky, W. T. Vetterling, and B. P. Flannery, *Numerical recipes in C* (Cambridge University Press, 1992).
- [38] J. F. Luo, Y. J. Liu, and E. J. Berger, *Comp. Mech.* **22**, 404 (1998).
- [39] P. N. Keating, *Phys. Rev.* **145**, 637 (1966).
- [40] H. Jiang and J. Singh, *Phys. Rev. B* **56**, 4696 (1997).
- [41] H. R. Eisenberg and D. Kandel, *Phys. Rev. B* **66**, 155429 (2002).
- [42] W. W. Mullins, *J. Appl. Phys.* **28**, 333 (1957).

- [43] H. R. Eisenberg and D. Kandel, *Phys. Rev. Lett.* **85**, 1286 (2000).
- [44] K.-J. Bathe, *Numerical methods in finite element analysis* (Prentice Hall, New Jersey, 1976).
- [45] R. L. Honeycutt, *Phys. Rev. A* **45**, 600 (1992).
- [46] D. E. Jesson, S. J. Pennycook, J.-M. Baribeau, and D. C. Houghton, *Phys. Rev. Lett.* **71**, 1744 (1993).
- [47] M. Kardar, G. Parisi, and Y. C. Zhang, *Phys. Rev. Lett.* **56**, 889 (1986).
- [48] Z.-W. Lai and S. D. Sarma, *Phys. Rev. Lett.* **66**, 2348 (1991).
- [49] A. L. Barabási and H. E. Stanley, *Fractal concepts in surface growth* (Cambridge University Press, 1995).
- [50] T. Sun, H. Gao, and M. Grant, *Phys. Rev. A* **40**, 6763 (1989).
- [51] J. Villain, *J. Phys. I* **1**, 19 (1991).
- [52] J. Krug, *Origins of scale invariance in growth processes*, Habilitation thesis for Heinrich Heine Universität Düsseldorf, Forschungszentrum Jülich, 1995.
- [53] A. A. Golovin, S. H. Davis, and P. W. Voorhees, *Phys. Rev. E* **68**, 056203 (2003).
- [54] B. J. Spencer and J. Tersoff, *Phys. Rev. Lett.* **79**, 4858 (1997).
- [55] S. P. Ahrenkiel, A. G. Norman, M. M. Al-Jassim, A. Mascarenhas, J. Mirecki-Millunchick, R. D. Twesten, S. R. Lee, D. M. Follstaedt, and E. D. Jones, *J. Appl. Phys.* **84**, 6088 (1998).
- [56] R. F. Sekerka, *Theory of crystal growth morphology*, in *Crystal growth – from fundamentals to technology*, Elsevier, 2004.
- [57] V. M. Kaganer and K. H. Ploog, *Phys. Rev. B* **64**, 205301 (2001).
- [58] Review of surface diffusion experiments can be found at <http://www.mse.ufl.edu/~spear>.
- [59] M. Kasu and N. Kobayashi, *J. Appl. Phys.* **78**, 3026 (1995).
- [60] M. A. Herman and H. Sitter, *Molecular beam epitaxy – Fundamentals and current status* (Springer, 1996).
- [61] V. Holý, U. Pietsch, and T. Baumbach, *High-resolution x-ray scattering from thin films and multilayers* (Springer, 1999).
- [62] S. K. Sinha, E. B. Sirota, S. Garoff, and H. B. Stanley, *Phys. Rev. B* **38**, 2297 (1988).
- [63] P. H. Dederichs and J. Pollmann, *Z. Physik* **255**, 315 (1972).
- [64] S. Dietrich and W. Fenzl, *Phys. Rev. B* **39**, 8873 (1989).
- [65] C. Dorin, J. Mirecki-Millunchick, Y. Chen, B. G. Orr, and C. A. Pearson, *Appl. Phys. Lett.* **79**, 4118 (2001).

- [66] J. W. Matthews and A. E. Blakeslee, *J. Cryst. Growth* **27**, 118 (1974).
- [67] I. M. Lifshitz and L. N. Rosenzweig, *Zh. Eksp. Teor. Fiz.* **17**, 783 (1947), In russian.
- [68] T. C. T. Ting and V. G. Lee, *Q. J. Mech. Appl. Math.* **50**, 407 (1997).
- [69] P. H. Dederichs and G. Leibfried, *Phys. Rev.* **188**, 1175 (1969).
- [70] P. Brož and P. Procházka, *Metoda okrajových prvků v inženýrské praxi* (SNTL, Praha, 1987), In czech.
- [71] J. P. Hirth and J. Lothe, *Theory of dislocations* (McGraw-Hill, 1968).

# Curriculum vitae

Ondřej Caha

- Born on 25<sup>th</sup> February 1979 in Třebíč
- 1997 finished grammar school in Jihlava
- 1997–2002 study of physics, Faculty of Science, Masaryk University in Brno; Diploma thesis: *Small angle x-ray scattering on quantum dots*, supervisor Prof. V. Holý.
- 2003–2005 two stays at University of Houston, USA, together 10 months.

## List of publications

1. O. Caha, V. Křápek, V. Holý, S. C. Moss, J.-H. Li, A. Norman, A. Mascarenhas, J. L. Reno, J. Stangl, and M. Meduňa, *X-ray diffraction on laterally modulated InAs/AlAs short-period superlattices*, J. Appl. Phys. **96**, 4833 (2004).
2. O. Caha, P. Mikulík, J. Novák, V. Holý, S. C. Moss, A. Norman, A. Mascarenhas, J. L. Reno, and B. Krause, *Spontaneous lateral modulation in short-period superlattices investigated by grazing-incidence X-ray diffraction*, Phys. Rev. B **72**, 035313 (2005).
3. J.-H. Li, D. W. Stokes, O. Caha, S. L. Ammu, J. Bai, K. E. Bassler, and S. C. Moss, *Morphological instability in InAs/GaSb superlattices due to heterointerfaces*, Phys. Rev. Lett. **95**, 096104 (2005).
4. O. Caha, V. Holý, and K. E. Bassler, *Nonlinear evolution of surface morphology in InAs/AlAs superlattices via surface diffusion*, Phys. Rev. Lett. **96**, 136102 (2006).

## Conference presentations

1. O. Caha and V. Holý, *Grazing-incidence diffraction on InAs/AlAs short-period superlattices*, Workshop "Characterization of thin films by x-ray scattering", Uckley (Germany), 2003 (talk).
2. O. Caha, V. Křápek, and V. Holý, *X-ray diffraction on laterally modulated (InAs)<sub>n</sub>/(AlAs)<sub>m</sub> short-period superlattices*, 8<sup>th</sup> international conference on surface X-ray and neutron scattering, Bad Honnef (Germany), 2004 (poster).
3. O. Caha, V. Křápek, and V. Holý, *X-ray diffraction on laterally modulated InAs/AlAs short-period superlattices*, 7<sup>th</sup> biennial conference on high-resolution x-ray diffraction and imaging, Průhonice u Prahy (Czech republic), 2004 (poster).
4. O. Caha, V. Holý, P. Mikulík, J. Novák, S. C. Moss, and K. E. Bassler, *Lateral compositional modulation in InAs/AlAs short-period superlattices studied by x-ray diffraction*, 6<sup>th</sup> autumn school of x-ray scattering from surfaces and thin layers, Smolenice (Slovakia), 2005 (talk and poster).
5. O. Caha, V. Holý, P. Mikulík, J. Novák, S. C. Moss, and K. E. Bassler, *Evolution of the lateral modulation in InAs/AlAs short-period superlattices grown on InP*, 28<sup>th</sup> international conference on the physics of semiconductors, Wien (Austria), 2006 (poster).